Calcium-Silicate-Hydrate in cementitious systems: chemomechanical correlations, extreme temperature behavior, and kinetics and morphology of in-situ formation.

by

Deepak Jagannathan

B. Tech, Indian Institute of Technology Madras (2010)

Submitted to the Department of Materials Science and Engineering in partial fulfillment of the requirements for the degree of

Master of Science in Materials Science and Engineering

at the

Massachusetts Institute of Technology

February 2013

Signature redacted

Author .....
Department of Materials Science and Engineering
January 14 2013

Signature redacted

Certified by ....
Krystyn J. Van Vliet, Thesis Advisor
Paul M. Cook Career Development Associate Professor of Materials Science and Engineering

Signature redacted

Accepted by .....
Gerbrand Ceder, Chairman, DMSE Committee on Graduate Students
R.P. Simmons Professor of Materials Science and Engineering

Dedicated to Janaki Srinivasan, Rama Jagannathan, Rangaswamy Jagannathan, and Dinesh Jagannathan whose unshakable faith in my abilities continues to propel me ...

A Thank You Note

Galileo Galilei once said

"We cannot teach people anything; we can only help them discover it."

This is a humble attempt to express, in mere words, my gratitude towards people who have guided by discoveries at MIT.

When I started to work with Krystyn Van Vliet, I can confidently say that I was the least meticulous member of her research group. Being haphazard was not a particular strength in this situation. Over the past two years, as a result of her consistent insistence to put my best foot forward, I have been able to reach, hitherto unknown, potentials. In fact, to be quantitatively precise, I have become 147.2 $\pm$ 29.8 % more efficient with my time. In particular, being more organized has made me a better team player in my collaborative efforts. I owe her for helping me discover the benefits of a strong work ethic.

VV Group has been sweet and optimum to me. It is quite essential that every graduate student finds an optimum office. If you become best friends for life with your office mates, the probability of your graduation within a prescribed time frame will dwindle to appallingly low values. On the other hand, you should like them enough to share a cottage in the woods in New Hampshire for the weekend. This group has been that and much more.

Others have helped me see the method in the madness, that my experimental data is.

Franz Ulm can infuse energy and imagination into any topic, and make it seem fascinating. Before taking his class, I would not have considered microporomechanics to be something interesting. Watching him present conclusive evidence / opinion / wild guess with such natural presence has helped me discover my passion for telling stories.

Hamlin Jennings has helped me discover patterns in my data through his vast experience. On more than one occasion, he has been able to listen to my ramblings, stare outside through the window for a brief moment, and *voila*, a diagnosis or explanation that I would have never thought of. He has helped me discover the joy of connecting the dots between what you *know* and what you *see*.

It may come as no surprise to the reader that I am still learning how to be a skilled experimentalist. Luckily, I have been able to partner with the right people.

During the early stages of my graduate program, *Jon Estrada* helped me ease into the life of an experimentalist. He helped me learn the arts of sample preparation and nanoindentation. For my last project, I have been able to perform complex experiments. I owe *Romain Grossier* and *Nicola Ferralis* for designing these experiments and for being great collaborators.

In the past two years, my *Facebook friends* living in Cambridge, MA have given me unique experiences to cherish. I cannot list all of them here for space constraints. However, I want to mention that in each one of them, I discovered a part of myself.

Contents

List of Figures

List of Tables

Abstract

Concrete, the second most used material on the planet, is a multi-scale heterogeneous material. A fundamental component known as Calcium-Silicate-Hydrate which forms from the reaction between cement and water is the binding phase in concrete. Curiously, this is the least understood component of concrete because of its porous amorphous structure. Further, beyond mere scientific curiosity, cementŠs industry large carbon footprint due to its volume of usage sets up a practical context to seek improvements in concrete performance and equip concrete with additional functionalities. It is our contention that we can better understand the least known and crucial component of concrete, Calcium-Silicate-Hydrate, to inform the design of next generation of high performance concrete. With this broad theme, this thesis presents three different aspects of properties of Calcium Silicate Hydrate: chemo-mechanical correlations, behavior under extreme temperature and pressures, and kinetics and nanostructure of in-situ formation.

Calcium Silicate Hydrate (C-S-H) formed in-situ in concrete is believed to have a layered structure with silicate chains similar to crystal structures of Tobermorite and Jennite. Its chemical composition, characterized by Ca/Si ratio, must therefore influence its silicate chain structure and thus its mechanical properties. We explore the correlation between C-S-H composition and its mechanical properties. By varying chemical composition of cement clinkers and supplementary cementitious materials, water/cement ratios, and hydration temperatures, we prepare cement pastes with different C-S-H of different C/S ratios. We use nanoindentation and X-ray spectroscopy to respectively measure the mechanical properties and composition of C-S-H.

We then study the mechanical performance of C-S-H at elevated temperatures. This is relevant in the design of infrastructure that can sustain extreme events such as blasts and high velocity impacts. As a starting point for concrete that would enable such infrastructure, we use ultra high performance concrete (UHPC). We use nanoindentation and X-ray spectroscopy to respectively measure mechanical properties and composition of individual components of UHPC. We compare the composition and properties of C-S-H found in UHPC to that found in ordinary cement pastes (OPC). Our grid nanoindentation experiments also reveal an artifacts created by the incorporation of steel fiber reinforcements in UHPC. We find that steel fiber reinforcements disrupt the perfect packing of constituent materials in UHPC to create capillary porosity at microscale. Further, we study the mechanical properties of C-S-H in concrete specimens subjected to high temperatures of 400°C and 1000°C.

As a product of the reaction between cement and water, the properties of C-S-H are ultimately controlled by the reaction. To obtain quantitative kinetics, we use time-lapse optical microscopy to study hydration of micron sized monoclinic C_3S particles with in

droplets of water of 50 μm. Using Raman spectroscopy, we characterize the hydration product growing inside these droplets.

Chapter 1

Calcium Silicate Hydrates in cementitious materials

1.1 Sustainability Challenge

Concrete is the second most consumed material in the world, with 20 billion tons produced annually, representing one cubic meter per capita per year [1]. Concrete has a huge carbon footprint due to its scale of consumption and the use of cement. Production of cement generates 0.8 tons of CO_2 per ton of cement, resulting approximately in 0.3 tons of CO_2 per ton of concrete [2]. On the other hand, cement is crucial to concrete's mechanical strength [3]. A composite material comprising primarily of cement, sand, and water, concrete derives its mechanical strength from calcium-silicate-hydrate (termed C-S-H), a product of the reaction between cement and water [4]. The C-S-H phase binds multiple components of concrete together, providing structural integrity to concrete. [4]. Interestingly, after two centuries of concrete usage, C-S-H, the vital binding phase, is the least understood component of concrete.

A fundamental understanding of C-S-H, specifically its mechanics, offers limitless possibilities to engineer concrete with higher performance, multiple functionalities, and reduced carbon footprint. [2, Essay: What's the matter with Concrete] The nano-to microscale porosity of C-S-H together with multiscale heterogeneous nature of concrete have hindered a systematic understanding of C-S-H. Advances in materials characterization techniques in the last decade enable us to overcome these impediments by providing access to ever so smaller material volumes [5]. Herein lies the central theme of this thesis: a fundamental understanding of of physical, chemical and mechanical properties of C-S-H to inform the macroscopic design of concrete. This chapter sets up the context for original work in the following chapters by presenting a review of cement hydration, C-S-H structure and mechanics, and experimental techniques used to characterize C-S-H.

Phase	Formula	Wt% of OPC
Alite	Ca_3SiO_5	50-70
Belite	Ca_2SiO_4	15-30
Aluminate	$Ca_3Al_2O_6$	5-10
Ferrite	Ca_2AlFeO_5	5-15

Table 1.1: Major phases in OPC. All the phases have significant levels of impurities which are not captured in the listed formulae [6].

1.2 Cement Chemistry Notation - A Primer

Cement reacts with water to importantly produce the binding phase, C-S-H. The most common variety of cement is called Ordinary Portland Cement (OPC) or simply Portland Cement. It is made by heating limestone and clay, or other materials of similar bulk composition, ultimately to a temperature of 1450°C [6]. Nodules of clinker are thus produced. Clinker is composed of four major phases: alite, belite, aluminate, and ferrite [6]. Table 1.1 details of composition of these phases.

The cement chemistry nomenclature represents these phases using oxides as elementary components. For instance Ca_3SiO_5 is represented as $3CaO.SiO_2$. Common oxides are abbreviated to single letters, such as C for CaO and S for SiO_2. Ca_3SiO_5 thus becomes C_3S, while Ca_2SiO_4 becomes C_2S. The most widely used abbreviations are listed below.

$$\begin{array}{llll} C = CaO & S = SiO_2 & A = Al_2O_3 & F = Fe_2O_3 \\ M = MgO & K = K_2O & \bar{S} = SO_3 & N = Na_2O \\ T = TiO_2 & P = P_2O_5 & H = H_2O & \bar{C} = CO_2 \end{array}$$

Thus, the major phases in OPC are C_3S, C_2S, C_3A , and C_4AF in the order listed in the table above. Note that C-S-H is not $CaOSiO_2H_2O$. The hyphens indicate the lack of specific stoichiometry.

1.3 Hydration of Portland Cement

The definitions of the following terms have been adopted from [6]:

Hydration is the reaction of clinker with water to produce various products including C-S-H.

Setting is stiffening of a mixture of cement and water without significant development of compressive strength, and typically occurs within a few hours of mixing.

Paste is a mixture of cement and water in such proportions that setting and hardening occur. This term is extended to include the hardened material.

Water/cement (w/c) or water/solid (w/s) ratio refers to proportions by weight; for a paste, it is typically 0.3-0.6.

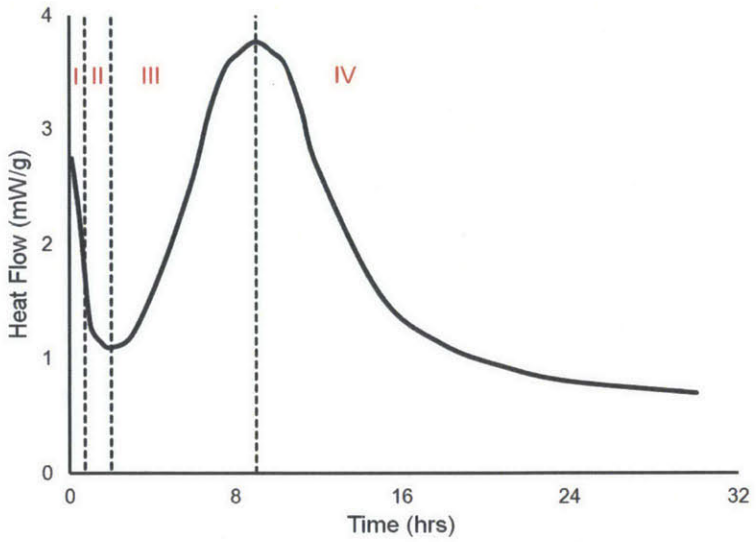

Figure 1.1: Representative plot of rate of alite hydration (quantified by heat flow in calorimetric experiments) as a function of time showing various stages of hydration separated by dotted lines. I - Initial reaction; II - Period of slow reaction; III - Acceleration period; IV - Deceleration period. Based on Figure 1 in [4].

Curing means storage under conditions in which hydration occurs; typically in air initially and subsequently in water or saturated lime solution after 24 h.

Given OPC is a complex mixture of phases, studies on rate of hydration are typically conducted on individual constituent phases. A majority of these studies focus on alite, the principal constituent. For a given particle size and w/c ratio, setting and hardening processes of alite and OPC are similar [6]. 70% of C_3S in OPC reacts in 28 days and virtually all in 1 year to produce calcium hydroxide (CH) and amorphous C-S-H. Reaction of C_2S with water is similar, albeit much slower [4].

The rate of hydration has been measured using various techniques. Some examples include isothermal calorimetry, quantitative X-ray diffraction, nuclear magnetic resonance (NMR), and small angle neutron scattering (SANS). These techniques measure the net rate of hydration, but do not provide sufficient details to construct a reaction mechanism [4]. However, they have been used to systematically explore influence of factors such as fineness of cement particles, w/c ratio, and temperature. Based on rates of hydration measured in calorimetric experiments (see Figure 1.1), alite hydration reaction is divided into four stages: (1) initial reaction, (2) period of slow reaction, (3) acceleration period, and (4) deceleration period.

1.3.1 Initial and slow reaction periods

In the initial period, wetting and dissolution of C_3S results in a sharp exothermic signal. C_3S has been shown to dissolve congruently and quite rapidly in the first few seconds [7] as

given by

$$C_3S + 3H_2O \rightarrow 3Ca^{2+} + H_2SiO_4{}^{2-} + 4OH^- \quad (1.1)$$

Interestingly, the dissolution rate of alite rapidly declines resulting in the so called induction or slow reaction period. Note that the reaction rate is still non-zero. Several hypotheses have been proposed and debated in the literature [8]. Here, we mention two mechanisms that continue to remain plausible in light of recent studies.

The metastable barrier hypothesis argues that rate of hydration reaction declines because of the formation of a continuous thin metastable layer of C-S-H which passivates the clinker surface by limiting diffusion of detaching ions. Calcium and silicate ion concentrations measured by various studies in literature on early hydration have been shown to lie along one of the two solubility curves, suggesting the existence of two different kinds of C-S-H; one stable and the other metastable [9]. Simulations of hydration reaction using a metastable barrier hypothesis have successfully reproduced several results from experimental studies of alite hydration [10]. Critics of the metastable barrier hypothesis point to scant direct experimental evidence of the existence of such a passivating layer. In recent years, the challenge has not been to prove the existence of an early hydrate phase, but to show its passivating influence [4]. The mechanism for the end of delay period is also not clear.

The slow dissolution hypothesis draws parallels from dissolution processes of many natural minerals where build up of ions in solution controls the dissolution mechanism. For instance, far away from equilibrium, fast dissolution occurs through initiation of etch-pits, while closer to reaction equilibrium but still significantly undersaturated, the driving force is not sufficient to open etch-pits and dissolution occurs through slow retreating steps. Support for this view comes from experiments on stirred C_3S suspensions of high w/c ($\sim$ 50000) [11] and studies on role of crystallographic defects in the early hydration process [12]. Saturation state of the solution does not however seem to be the only controlling factor. In conventional alite hydration experiments, researchers have observed a sharp peak in silicate concentration in the first few minutes. The decline of silicate concentration has been attributed to C-S-H nucleation. However, according to the slow dissolution step hypothesis, this decline in silicate concentration should prompt an increase in rate of dissolution of alite which is not experimentally observed.

1.3.2 Nucleation & Growth of C-S-H

At a certain critical point, C-S-H nucleation and growth accelerates hydration kinetics. C-S-H is known to nucleate heterogeneously on alite surface [13, 14]. There is a growing body of literature that uses nucleation and growth models to study alite hydration data (e.g., shown in Figure 1.1) and report good agreement between the model and experimental data. NMR spectroscopy based studies show that rate of hydration beyond the delay period is proportional to surface area of C-S-H suggesting C-S-H growth might be the rate determining step [15].

Because of limited number of direct observations of C-S-H nucleation, the literature on C-S-H nucleation is largely driven by modelling and simulation of hydration reaction [16]. Traditionally, Avrami's model [17], also known as JMAK model, has been applied to the calorimetric data shown in Figure 1.1. This model assumes that nucleation of C-S-H can be

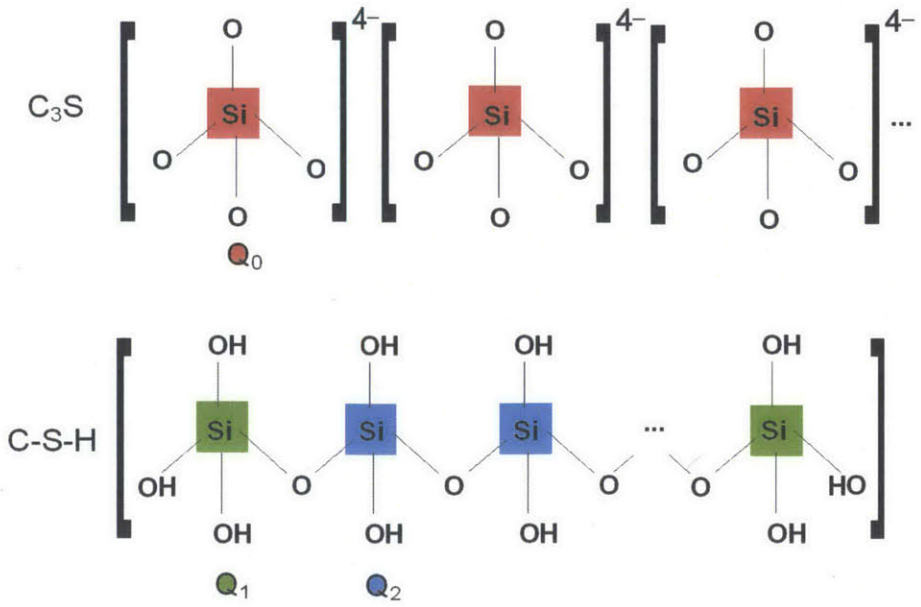

Figure 1.2: Si atoms in ^{29}Si MAS NMR spectroscopy are labelled as Q_n where n represents the number of bridging O atoms (that are bonded to two Si atoms). In anhydrous C_3S (and C_2S), silicate tetrahedra exist as individual SiO_4^{4-} units and hence the corresponding Si atoms are labelled Q_0 (red). In C-S-H, there are two types of Si atoms. Q_1 (green) bonded to one bridging O atom occur at the end of silicate chains. Q_2 (blue) bonded to two bridging O atoms occur in the middle of the silicate chains between two Q_1 ends. We refer to the ensemble of Q_n Si atom with its four O atoms as Q_n group.

both homogeneous and heterogeneous which contradicts exclusive heterogeneous nucleation observed in the limited number of controlled experiments [13,14,18]. Applicability of Avrami model also requires nucleation to start 1 hour after mixing. On the other hand, boundary nucleation and growth model (BNG) proposed by Thomas [19] assumes heterogeneous nucleation on C_3S particles and hypothesizes that nucleation of C-S-H starts as soon as alite is mixed with water. The Avrami model fits the calorimetric data until the hydration peak (end of stage III and start of stage IV in Figure 1.1). The BNG model has been shown to fit the calorimetric data well past the rate hydration peak. Further, 3D hydration simulations also predict nucleation to occur heterogeneously at the start of mixing [16]. The importance of nucleation in transition to acceleration stage is underscored by studies on eliminating induction period by seeding alite pastes with reactive form of C-S-H [20]. In these studies, the hydration rate progressed to acceleration stage immediately after mixing. The precise timing of nucleation is an ongoing area of research.

Growth mechanism and morphology are topics that have been heavily debated in the literature [4, references there in]. There are two schools of thought: one suggests that C-S-H grows as layers of defective silicate chains, while the other proposes aggregation of C-S-H nanoparticles.

According to the first mechanism, silicate tetrahedra bind to growing 2D silicate sheets.

Calcium atoms and hydroxyl groups are sandwiched between such silicate sheets to form structures similar to crystalline minerals forms of C-S-H known as Tobermorite and Jennite. This is compatible with TEM based observations of crystallinity in C-S-H at length scales of $\sim$ 1 nm [21, 22]. To account for the long range disorder or amorphous nature of C-S-H, this mechanism proposes that the growth of silicate chains will be punctuated by defective sites where silicate tetrahedra do not attach. Further, the idea of polymerization of silicate chains is supported by evidence from NMR experiments.

NMR experiments classify Si atoms in silicate chains in cement into three: Q_0, Q_1 and Q_2 , with the subscript indicating the number of bridging Oxygen atoms that are attached to the Si atom in question. While Q_0 Si atoms are only found in anhydrous C_3S (and anhydrous C_2S), Q_1 and Q_2 Si atoms are found in C-S-H (Figure 1.2). Isolated silicate tetrahedra (SiO_4^{4-}) have Q_0 Si atoms, while a silicate chain with n Si atoms can be visualized as having 2 Q_1 Si atoms at the end of the chain and (n-2) Q_2 atoms between the ends (Figure 1.2). Thus, higher the proportion of Q_2 Si atoms, the longer the silicate chains.

Using NMR spectroscopy, several studies have shown silicates in early stages of cement hydration to be Q_1 silicates [4]. Notably, Brough and coworkers [23] measured relative proportions of Q_n silicates, $n \in \{0, 1, 2\}$ as a function of time (see Figure 1.3). The proportion of Q_0 (red in Figure 1.3) steadily declines indicating the consumption of anhydrous C_3S. In the first 100 hours of alite hydration, the hydrated phase is dominated by Q_1 silicate groups (green in Figure 1.3). In other words, C-S-H initially consists of dimeric silicate groups. Note that the inflexion point in both the proportions of Q_1 and Q_2 (green and blue, respectively in Figure 1.3) at about 1000 h. Q_1 starts to slowly decrease while Q_2 starts to increase at a higher rate than before. The steady increase of Q_2 points to increasing silicate polymerization in C-S-H, as hypothesized by the silicate tetrahedra based growth model for C-S-H.

The alternative mechanism for C-S-H growth is based on the aggregation of C-S-H nanoparticles. This mechanism proposes that nuclei of C-S-H or C-S-H nanoparticles grow up to a few nanometers and then stop growing [4]. These nuclei then act as nucleation

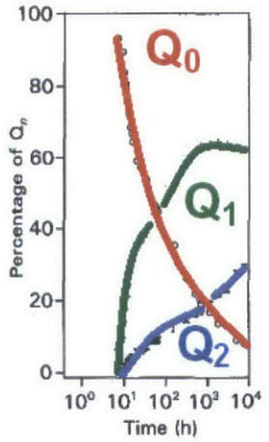

Figure 1.3: Evolution of relative quantities of Q_n silicates with time (log scale) for C_3S hydration at 20°C with w/c = 0.5. (red) Q_0, (green) Q_1 and (blue) Q_2. Adapted from [23].

and aggregation sites for new C-S-H nanoparticles and existing C-S-H nanoparticles in pore solution, respectively. Such a mechanism is compatible with structural models for C-S-H in mature pastes that will be discussed in the next section. However such nanoparticle based growth of C-S-H would imply that the thermodynamic driving force of heterogeneous or homogeneous nucleation of C-S-H nanoparticles is greater than that for growth of these particles. Evidence from experiments and modelling of C-S-H growth contradict this deduction [4]. A deep divide between two structural models for C-S-H, i.e., silicate chain and C-S-H nanoparticle based models, continues to exist. While the former accounts for experimental data on early stages of hydration, the latter is best able to explain experimental data on mature pastes. To complete the discussion on rate of hydration, deceleration period is triggered by several factors including diffusion, complete consumption of small alite particles, lack of space, and lack of water.

1.3.3 Open Questions in Cement Hydration

The following points of discussion have been assimilated from Refs. [4, 16].

Mechanistic understanding of period of slow reaction

We presented the current views on the period of slow reaction. Settling this issue has practical benefits in being able to control the setting time and early age properties of concrete. For instance, some applications like oil-well cementing require long setting times during which the concrete remains fluid. This is currently achieved through an empirical understanding of accelerators and retarders, reagents that accelerate and retard the rates of hydration of cement, respectively. A mechanistic understanding with physical basis can help design concrete formulations for specific applications.

Kinetics of C-S-H nucleation & growth

We noted the studies on alite dissolution and nucleation of C-S-H. However, there is a dearth of knowledge on rate constants and rate determining steps controlling C-S-H nucleation and growth. The complexity of cement hydration has prevented a systematic understanding of kinetics of individual steps contributing to the hydration process.

Morphology of C-S-H growth

We discussed the two possible mechanisms of C-S-H growth. Several observations on morphology of C-S-H have been made in the literature. There is a lack of coherent understanding of C-S-H growth, particularly in the early stages and how it can be coupled with the models of C-S-H in mature pastes. As we will see in Chapter 3, a great deal of progress has been made in controlling the properties of other components of concrete. The missing link that hinders a complete control of macroscopic properties of concrete is therefore the growth and morphology of C-S-H phase.

Role of supplementary cementitious materials

Supplementary cementitious materials (SCM) like fly ash, blast furnace slag, silica fume etc, are becoming increasingly prominent in concrete mixes. These materials can substitute cement clinker and thus reduce concrete's carbon footprint. Further, these SCMs can react with water to produce hydration products, importantly C-S-H. These SCMs are far more complicated than crystalline phases in OPC. We lack a complete understanding of OPC hydration and the addition of SCMs further convolutes this problem.

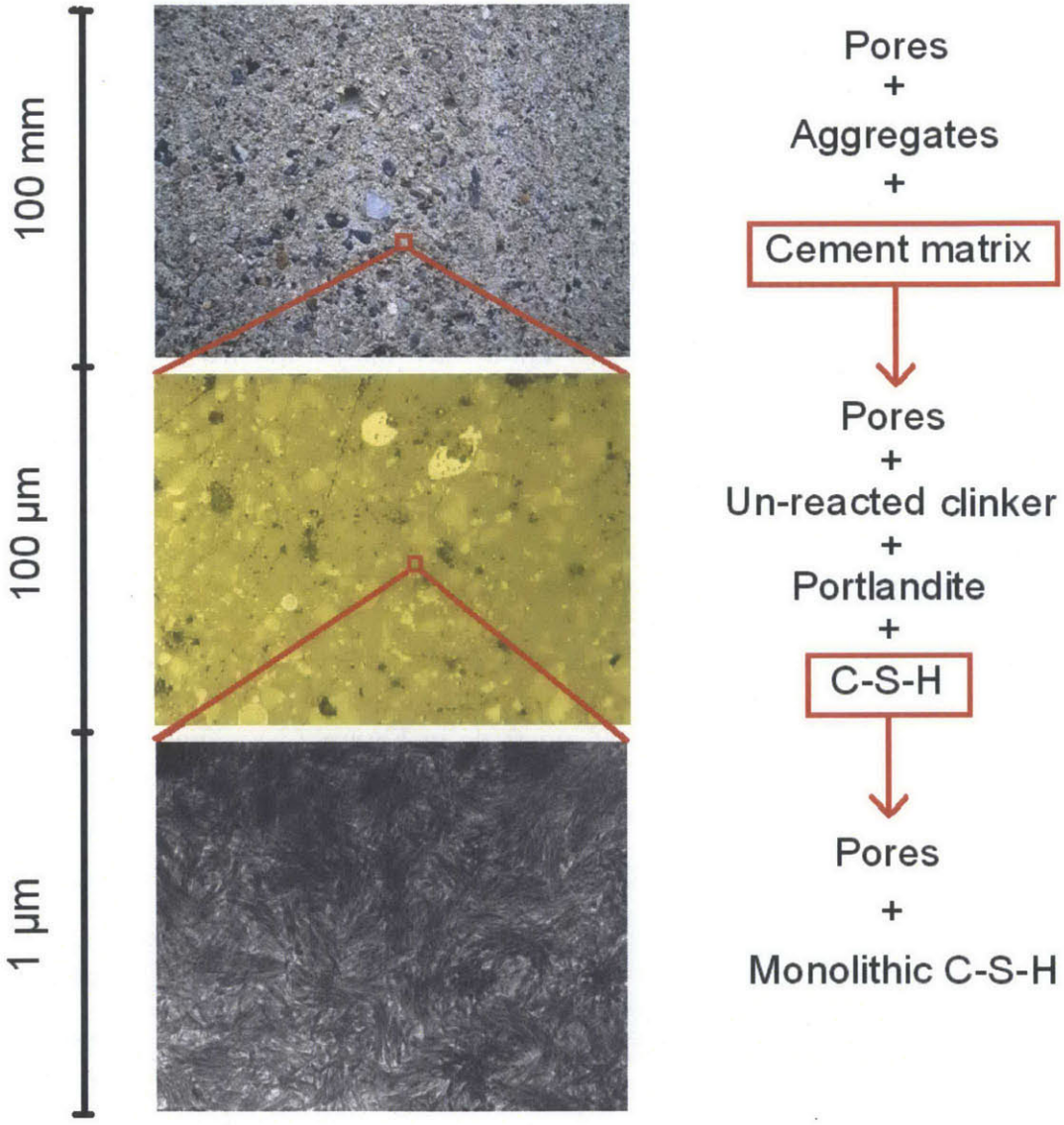

Figure 1.4: Concrete is a multiscale heterogeneous material. 1 µm micrograph adopted from [22].

1.4 Structure of C-S-H in mature pastes

The structure of C-S-H in mature pastes has been another topic that has been heavily debated in the literature. Figure 1.4 illustrates one of the reasons why unearthing C-S-H structure has been such a challenge: the multiscale heterogeneous nature of concrete. Porosity complicates the issue even further. Structure of concrete at various levels has been extensively studied and interested reader is referred to Refs. [24] and [25] for details on macroscale and microscale structures of concrete respectively. This section will focus on micro- and nano-structures of C-S-H which are at the heart of our nanoindentation based measurement of mechanical properties of C-S-H that will be described in the next section.

C-S-H is structurally and mechanically heterogeneous at sub-micron scale. A number of researchers have agreed on two distinct forms of C-S-H, although their labels have been diverse [26]. The early models of C-S-H [27, 28] were able to explain the porosity of C-S-H, but were unable to account for its variable morphology associated with two different forms of C-S-H. Feldman and Sereda [28] proposed that C-S-H phase was an assembly of irregular C-S-H layers with inter-layer water molecules. Powers and Brownyard on the other hand, proposed a colloid like C-S-H phase made of small bricks or fundamental units. The currently used "Jennings model" [29,30] borrows from both these models and successfully accounts for both characteristics of C-S-H, porosity and variable morphology.

The Jennings model is a concise model that posits C-S-H to comprise of two structurally distinct but compositionally similar phases. These two phases are distinguished by their porosities and are supposed to exist because of experimental data [29] which show a positive correlation between surface area and gel porosity, as measured by nitrogen adsorption - a correlation which would be expected to be negative for a gel with a single porosity, that was proposed in earlier models [27]. Any model which considers the existence of two or more phases with different porosities would be able to explain this experimental phenomenon, but the fact that the Jennings model uses two phases is compatible with the observation of two distinct formations by many researchers.

The Jennings model proposes that "globules" of C-S-H (10 nm scale in Figure 1.5) of characteristic size $\sim$ 5 nm pack themselves into two characteristic forms: Low Density (LD) C-S-H and High Density (HD) C-S-H (500 nm scale in Figure 1.5) . The two phases are distinguished only by their porosities. The total gel packing density at microscale is a combination of the packing densities of LD and HD C-S-H:

$$\eta_{C-S-H} = \eta_{LD} \times f_{LD} + \eta_{HD} \times f_{HD} \tag{1.2}$$

where f_{LD} and f_{HD} are volume fractions of LD and HD C-S-H respectively and, $f_{LD} + f_{HD} = 1$. These volume fractions describe C-S-H microstructure. This degree of freedom is also the model's strength in contrast to earlier models which calculated singular values for C-S-H gel porosity. Thus, while earlier models are unable to explain the evolution of gel porosity during the cement hydration process, Jennings' model is able to reconcile with this fact by leveraging the degree of freedom of volume fraction of LD or HD C-S-H.

As noted above, two morphologies of C-S-H have been observed in several other studies. Richardson and others have noted the presence of two morphologically distinct forms of C-S-H in their Transmission Electron Microscopy (TEM) based studies of cement pastes [22,32]. They distinguish between outer product or Op C-S-H and inner product or Ip C-S-H. The

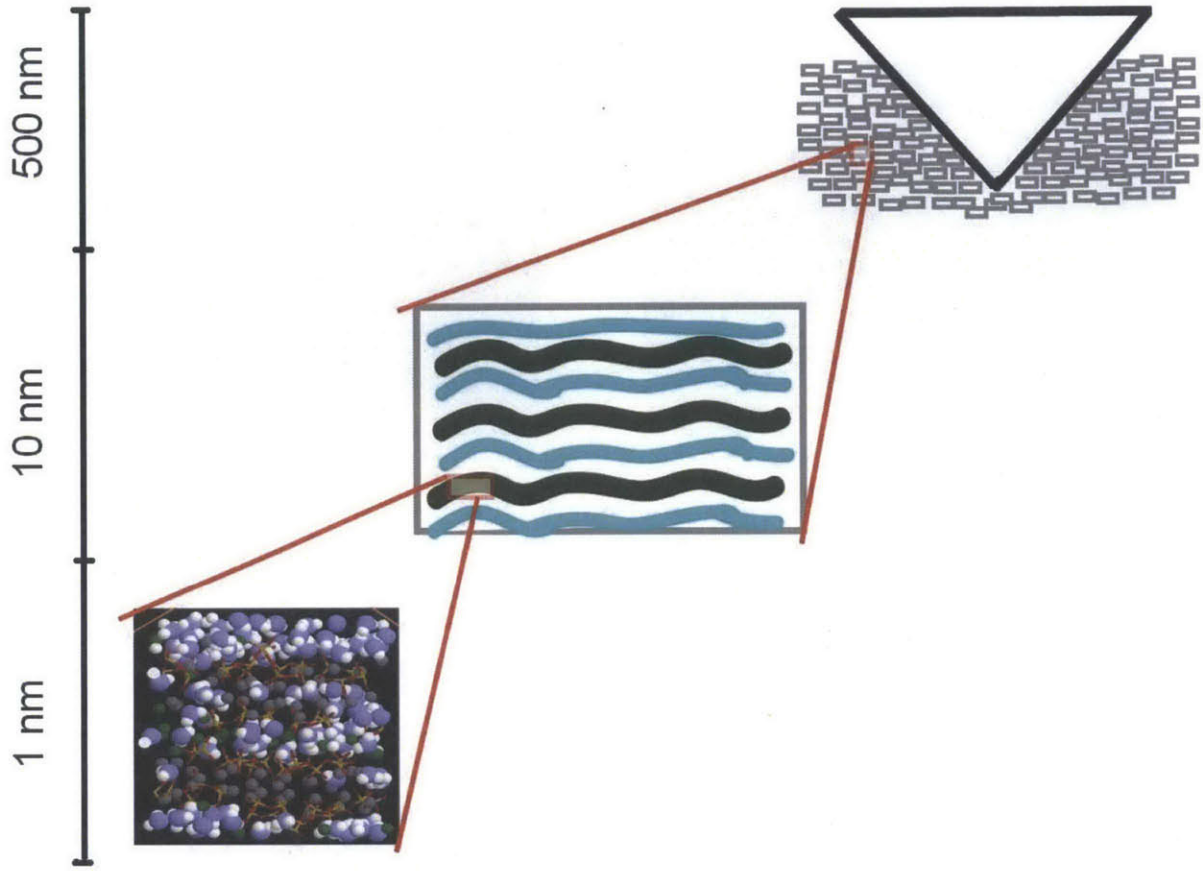

Figure 1.5: Schematic of multiscale structure of C-S-H. At the scale of 1 nm, the molecular model of C-S-H nanoparticle (from [31]): the blue and white spheres are oxygen and hydrogen atoms of water molecules, respectively; the green and gray spheres are inter and intra-layer calcium ions, respectively; yellow and red sticks are silicon and oxygen atoms in silica tetrahedra. At 10 nm scale, several nanoparticles are packed into a globule represented as a grey rectangle (after [29]). Globules consists of C-S-H layers (deriving from layered structures of crystalline calcium silicate hydrates) shown in dark green separated by layers of water molecules. At 500 nm scale, several globules pack randomly to form the microstructure. Note that the dimensions of globules or porosity at this scale are much smaller than the indentation depth as a result of which the nanoindenter tip (shown in black) perceives a homogenous material.

fibrillar Op C-S-H (see Figure 1.6) grows outwards from the clinker surface into the water filled pore space. Inner product or Ip C-S-H forms within the boundary of original clinker particles and has fine texture (Figure 1.6). Drawing parallels to globules of Jennings' models, Richardson notes that both Ip and Op C-S-H consist of (cit.) "globular particles" of different aspect ratios with dimensions $\sim$ 10 nm [22]. Several studies based on nanoindentation of cement pastes [26, 33–35] also report the presence of two forms of C-S-H. These studies estimate the packing fractions of LD and HD C-S-H to be $\eta_{LD} = 0.63$ and $\eta_{HD} = 0.76$

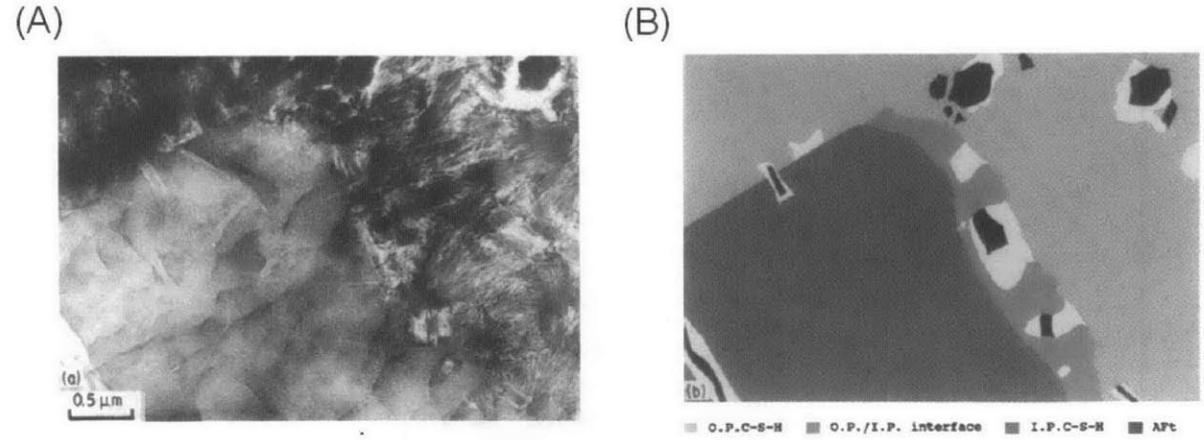

Figure 1.6: (A) Tranmission electron micrograph of OPC hydrated with w/c = 0/4 at 20°C for 3 months showing distinct morphologies of inner product (Ip) and outer product (Op) C-S-H. Ip C-S-H starting at the bottom left corner has a fine texture while Op C-S-H starting at the top right corner has fibrillar morphology. (B) Schematic of the same micrograph showing Ip (dark grey) and Op C-S-H (light grey). Adapted from [1993Richardson].

respectively.

In essence, it is clear that the structure of C-S-H between 10s of nm and 1 µm consists of a colloid like assembly of globules or particles. The Jennings model postulates that these globules in turn are an assembly of fundamental C-S-H nanoparticles of the size of $\sim$ 1 nm. We note that there is ongoing debate in literature on the precise packing arrangement of both fundamental nanoparticles to form a globule and globules to form LD (HD) C-S-H or Op (Ip) C-S-H. However, as described in the next section, a clever theoretical construction in micromechanics enables us to cut across these hierarchies to link the microscale properties of LD + HD C-S-H as measured by nanoindentation to the nanoscale properties of the C-S-H nanoparticle.

Efforts to model the exact structure of C-S-H nanoparticle have centered on structures of two natural calcium silicate hydrate minerals, 1.4 nm Tobermorite (approximately $C_5S_6H_9$) and Jennite ($C_9S_6H_{11}$) [22]. We remarked earlier about the parallels between silicate tetrahedra based growth model of C-S-H and structures of Tobermorite and Jennite. Every model must account for two basic characteristics of C-S-H. Firstly, C-S-H does not possess a unique composition, quantified by the ratio of Ca to Si atoms (Ca/Si or C/S). Ca/Si ratios in cement pastes range from 0.8 to 2.1 [22]. Secondly, nuclear magnetic resonance (NMR) spectroscopy and trimethylsilation (TMS) experiments have a recorded a series of distinct silicate chain lengths 2, 5, 8 ... (3n - 1), where n is a natural number.

It is difficult to directly observe the structure of these nanoparticles in experiments. Pellenq et al., recently proposed a model of C-S-H nanoparticle [31] of Ca/Si = 1.65 using molecular simulations (Figure 1.5, 1 nm scale). They validate this model by predicting the density of C-S-H nanoparticle to be 2.56 g/cm^3, which agrees closely with value of 2.6 g/cm^3 measured from neutron scattering experiments on C-S-H of Ca/Si = 1.7 [36]. This model

thus provides opportunities to predict several material properties of the C-S-H nanoparticle, importantly its stiffness and hardness which contribute to the compression strength of concrete. In the next section, we describe the use of nanoindentation and micromechanics modelling to predict the mechanical properties of C-S-H nanoparticle. In this work, we will compare our experimental results to those predicted from molecular simulations to explore the molecular origins of the properties we measure.

1.5 Characterization of C-S-H

1.5.1 Mechanical Properties: Nanoindentation

During the last decade, with the emergence of nanotechnology, characteristic sizes have continually declined across a wide variety of material applications. Nanoindentation has emerged as a leading characterization tool for the measurement for physical and mechanical properties across dimensions ranging from a few nm to a few μm [37]. Note that the idea of indentation however, i.e., pushing an indenter onto a material surface and characterizing the hardness of the material as the ratio of pressing force to the indentation area, dates back to early 20^{th} century. Owing to advances in sensors, actuators and computerized control of experiments in early 1990s, nanoindentation today has evolved into an experimental technique that can reliably measure continuum-scale mechanical properties by merely accessing sub-micron volumes of homogeneous materials.

A nanoindentation experiment involves application of load on a material surface using

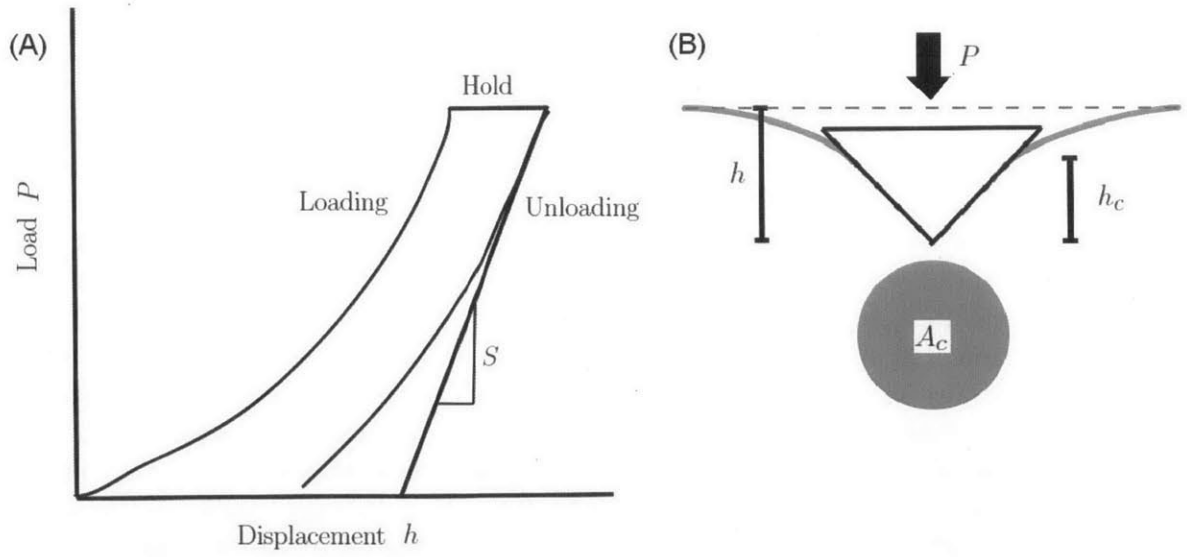

Figure 1.7: (A) Representative load displacement curve, its various segments and important variables defined in the text above. (B) Schematic of contact area in indentation experiments. P is the indentation load, h the indentation depth, h_c is the contact depth, and A_c is the projected area of contact.

an indenter to collect the load-displacement response (Figure 1.7A). We use the Berkovich trihedral pyramidal indenter. The behavior of the material during unloading (at least in the early stages) is assumed to be elastic. From elastic punch theory, we can relate initial unloading response to the elastic properties as [5]

$$S = \frac{dP}{dh}|_{h=h_{max}} = \beta \times \sqrt{A_c} \times E' \tag{1.3}$$

where β is a constant that depends on the shape of the indenter, A_c is the contact area (see Figure 1.7B) at maximum penetration depth, and E' is a composite elastic modulus of the material and indenter given by

$$\frac{1}{E'} = \frac{1-\nu^2}{E} + \frac{1-\nu_{in}^2}{E_{in}} \tag{1.4}$$

where E, ν and E_{in}, ν_{in} are the elastic constants of the indented material and the indenter, respectively. For the diamond indenter used in our work, E_{in} is at least one order of magnitude greater than E of most constituents of cementitious materials, thus $E' \simeq \frac{E}{1-\nu^2}$. We define indentation modulus M as $\frac{E}{1-\nu^2}$. Thus, equation 1.2 becomes

$$S = \frac{dP}{dh}|_{h=h_{max}} = \beta \times \sqrt{A_c} \times M \tag{1.5}$$

Equation 1.2 was originally developed for flat punch indenters with constant $c = \frac{2}{\sqrt{\pi}} = 1.128$. However, studies have shown it to be applicable to Berkovich indenter and estimate c in this case to be 1.167 [5]. Robust calibration methods have been established to accurately estimate the contact area A_c for Berkovich indenter as a function of penetration depth h [38]. Hardness H is calculated as

$$H = \frac{P}{A}|_{h=h_{max}} \tag{1.6}$$

Indentation of Cementitious materials: Grid Nanoindentation

Indentation provides access to mechanical properties at length scale $\propto h_{max}$, i.e., properties averaged over material volume $\propto h_{max}^3$. Given the nanoscale depth resolution, nanoindentation enables measurement of local mechanical properties. This is particularly relevant to calculating mechanical properties of constituent phases in heterogeneous material systems.

We wish to measure M and H of constituent phases of cementitious materials, importantly C-S-H. Appropriate choice of indentation depth h_{max} is crucial to such experiments. If h_{max} is much larger compared to characteristic size D of constituent phases, we would be measuring the composite response of mixture of phases. Thin film deposited on a substrate is a model material system in which characteristic size D (of the deposited phase) is easily accessible as the thickness of the film and thus, enables the study of the interplay between measured properties and indentation depth. Through indentation experiments on thin films at various h_{max}/D values, Constantinides and Ulm [26] estimate a critical $h/D = 0.1$ below which the measured mechnical properties of the film are within 10% of the mechnical properties of the pure phase. Transmission electron micrographs of cement pastes [32] have clearly shown C-S-H phase spanning lengths $> 2\mu$m. This defines an upper bound for h_{max} at approximately

200 nm. There are two lower bounds for h_{max}. Theoretically, principles of continuum mechanics used in equation 1.2 are valid when representative elementary material volume (r.e.v.) l satisfies $l \ll h_{max}$. For C-S-H, we can assume that this representative element is the C-S-H nanoparticles whose dimensions have been both theorized [29] and observed [22] to be well within 10 nm. The practical lower bound for h_{max} comes from surface roughness of the sample. One of the central assumptions in nanoindentation experiments is that the indenter is examining an infinite, isotropic, and homogeneous half-space. This assumption breaks down when surface roughness is comparable to or greater than the indentation depth. Surface preparation technique used in this work has been shown to reduce roughness to $\sim$ 10 nm [39]. Based on these bounds, we choose $h_{max} \simeq 200$ nm.

Now consider a material at length scale $L \gg D$, composed of multiple phases distributed uniformly. By performing a number of individual indentation tests, we would be able to sample constituent phases in a heterogeneous material with a probability that is equal to their respective volume fractions. This is the premise of grid nanoindentation - indenting at sufficiently shallow depths to estimate properties of a pure phase in a multiphase material and then repeating the indentation process a number of times to capture all the constituent phases in the multiphase material [33]. Recently, there have been a few studies that question grid nanoindentation based approach to measuring mechanical properties of C-S-H [40,41]. Their principal criticism centers around interaction volume of nanoindentation being comparable to volumes of pure LD or HD C-S-H seen in microscopy based studies in literature. In other words, at the proposed h_{max} and given the microscopic length scales of C-S-H, can the nanoindenter measure the individual properties of LD and HD C-S-H? In this work, we do not seek to evaluate individual M and H of LD or HD C-S-H, but rather seek the average mechanical properties of composite C-S-H phase (LD C-S-H + HD C-S-H) to subsequently compute the stiffness and hardness of the C-S-H nanoparticle. For this purpose, we can safely assume that at h_{max} proposed above, we are not evoking a composite response of C-S-H and other phases in cement paste. Thus, for our objectives, grid indentation provides the desired and valid access to mechanical properties of interest.

Data Interpretation

In a typical grid nanoindentation experiment, we carry out 1000 indentations and thus obtain a M and H data set. We first eliminate the data points extracted from irregular data curves corresponding to pores and surface preparation defects. The data set, thus obtained, is referred to as filtered data set. These irregular curves account for less than 20% of data. We then separate the subset of data points corresponding to the C-S-H phase from the filtered M and H data set using mixture modelling algorithms. We use the MCLUST package [42] available in R [43], a computational tool for statistical analyses. We briefly review the principles of mixture modelling here. For detailed understanding, the reader is referred to the MCLUST package documentation [1].

Given a set of data points for a mixture of components or phases, a mixture modelling or clustering algorithm is able to create a mixture model, i.e., classify each data point as belonging to a unique component or phase. In our case, this data set is a series of (M, H) coordinates associated with cement paste, a phase mixture. To demonstrate the idea, let us consider a solid phase mixture S1 with three solid phases with properties $(M_1, H_1) =$

$(100, 10)$, $(M_2, H_2) = (30, 1)$, $(M_3, H_3) = (50, 5)$ where all values are in GPa. A hypothetical nanoindentation data set for S1 is shown in Figure 1.8A. A curious reader might wonder why the results of a nanoindentation experiment have a scatter of data points around the bulk properties. The scatter arises out of (1) experimental error, and (2) mixing of phases, (2) being a bigger factor than (1). The reader is advised to refer back to the thin films analogy given in the previous section. The mixture modelling algorithm is then able to classify each data point in the data set as belonging to either Phase 1 or Phase 2 or Phase 3, shown in Figure 1.8B with different colors. Note that the mixture modelling process is agnostic to the actual values of$M$ and H of these phases. It merely explores the proximity and spatial density of data points in a scatter and comes up with the best model to account for the obtained data set. In this case, the only input that the algorithm accepts is a guess value of the number of phases present for which we use the range [1-20]. For each of $n \in [1 - 20]$, the algorithm fits the probability density of obtained experimental dataset $\mathcal{P}(M, H)$ as the sum of the probability densities of clusters centered around n individual phases. In other words, it minimizes the difference $\mathcal{D}$

$$\mathcal{D} = \mathcal{P}(M, H) - \sum_{i=1}^{n} f_i \times \mathcal{P}(M_i, H_i, \sigma_i) \tag{1.7}$$

where f_i is the volume fraction of phase i. M_i and H_i are the bulk properties of phase i. σ_i

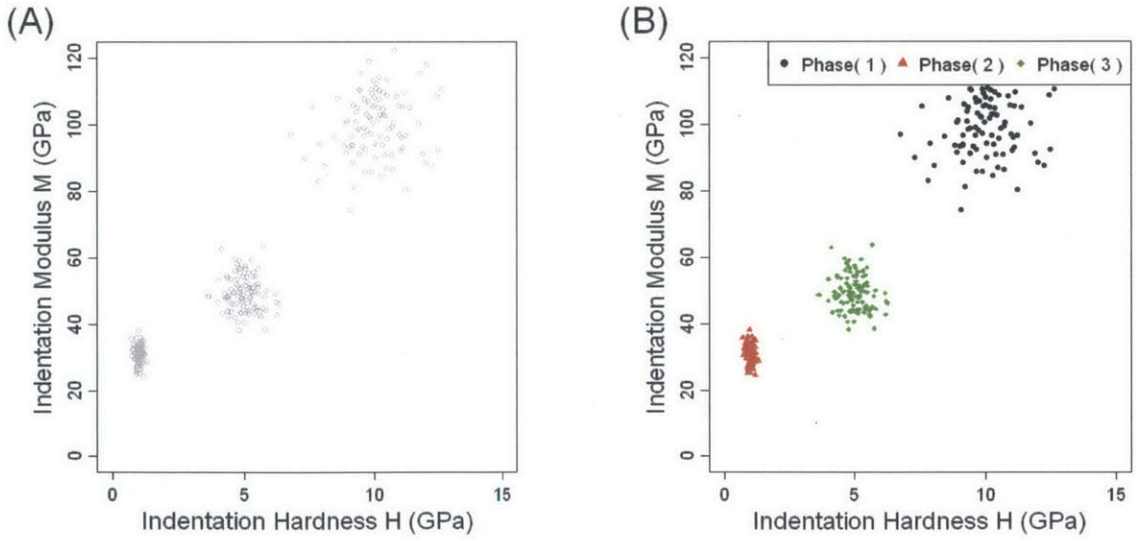

Figure 1.8: (A) Hypothetical experimental dataset obtained from nanoindentation of phase mixture S1 (see description above) (B) Mixture modelling algorithms segregates dataset in (A) into groups or clusters (represented by different coloured symbols) each corresponding to a unique phase. Here, the properties of individual phases are $(M_1, H_1) = (100, 10)$, $(M_2, H_2) = (30, 1)$, $(M_3, H_3) = (50, 5)$ GPa.

is the covariance matrix given by

$$\sigma = \begin{bmatrix} \sigma_{MM} & \rho_{MH} \\ \rho_{MH} & \sigma_{HH} \end{bmatrix} \tag{1.8}$$

where σ_{MM} and σ_{HH} are standard deviations of M and H respectively. ρ_{MH} is a measure of correlation between M and H. Additionally, the BIC criterion adds an extra term to $\mathcal{D}$ proportional to the number of terms n so that we arrive at an optimum mixture model with the least number of phases n. Further, MCLUST also explores several possible covariance structures. Hence, the variables that are being optimized to minimize $\mathcal{D}$ are $n, \{f_i\}, \{M_i\}, \{H_i\}, \{\sigma_i\}$.

The covariance matrix, especially the values of ρ_{MH} can help identify phases in cement paste. In grid nanoindentation experiments, we perform nanoindentation on a grid at different locations on a specimen. For crystalline materials like unreacted clinker and portlandite, the tip of the nanoindenter possibly encounters different crystalline planes as a result of which we measure different values of M and H at different locations. However, note that there would be no correlation between measured values of M and H at different locations, and thus, $\rho_{MH} = 0$. In the scatter plot of M and H, the corresponding cluster would be almost round. On the other hand, variation in local properties of C-S-H result from the

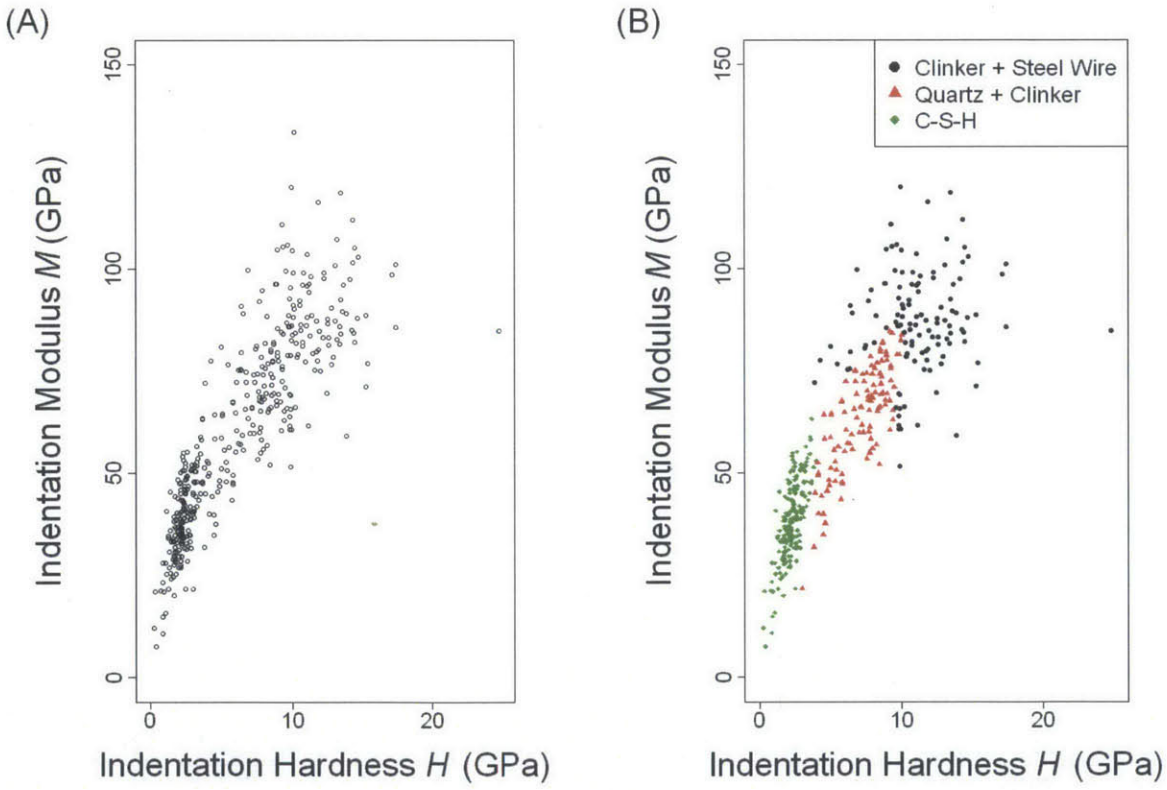

Figure 1.9: (A) Experimental dataset obtained from nanoindentation (B) Mixture modelling algorithms segregate dataset in (A) into groups or clusters (represented by different coloured symbols) each corresponding to a unique phase/phase mixture.

change in packing density η. In this case, the measured M and H would be highly correlated because both are proportional to η. In this case, the corresponding cluster would look be relatively narrow and elongated. Figure 1.9 demonstrates this idea using the results on a real nanoindentation data set obtained for ultra high performance concrete. The constituent phases at the microscale are quartz, clinker, C-S-H and steel fibers. The properties of all phases except C-S-H are known and by elimination, we assign the green cluster (Figure 1.9B) of data points to C-S-H phase. For the C-S-H phase, we find $< M > \in [25 - 35]$ GPa and $< H > \in [0.5 - 1.5]$ GPa in agreement with refs. [26, 33, 34]. In Figure 1.8B, notice that the C-S-H cluster is different in shape from that corresponding to clinker phase as expected.

Micromechanics - Extrapolation to nanoscale properties of C-S-H

At the nanoscale, C-S-H is a composite material of C-S-H nanoparticle and porosity. Since, the characteristic length scales of these two components are much smaller ($\sim$ 10 nm) than h_{max} in our experiments, nanoindentation is a valid technique to measure homogenized microscale properties of C-S-H. Micromechanics provides the link between M and H obtained from nanoindentation, i.e., composite properties, and intrinsic stiffness m_s and hardness h_s of C-S-H nanoparticle respectively. Homogenized response M and H is a function of the following parameters [35]

1. Intrinsic properties of C-S-H nanoparticle such as stiffness m_s, cohesion c_s, Poisson's ratio ν_s, and friction coefficient α_s of the C-S-H nanoparticle.

2. Packing density η of C-S-H nanoparticles. For instance, LD and HD C-S-H have different packing densities.

3. Morphological parameters like percolation threshold η_0, that is the solid fraction required to provide a continuous force path through the system. In micromechanics, there are two different morphological models of porous materials (Figure 1.10). In the matrix-porosity model, a distinct, homogeneous solid phase is punctuated with porosity. In this case, the solid phase remains continuous for any packing density $\eta > 0$, that is $\eta_0 = 0$. In polycrystal morphology, the solid phase itself is a granular material. In this case, the composite material of solid phase and porosity becomes unstable below $\eta = 0.5$ and thus, in this case $\eta_0 = 0.5$.

4. Indenter geometry-specific parameters such as cone angle θ. For the pyramidal Berkovich indenter, the equivalent cone angle $\theta = 70.32°$.

Based on nanoindentation experiments [35, 45], it has been shown that C-S-H is a randomly packed porous material (Figure 1.10). We note from our earlier discussion on C-S-H structure that indeed C-S-H has hierarchical porosity: nanoparticles pack into globules and globules into LD (HD) or Op(Ip) C-S-H. For this class of materials, micromechanics provides the following scaling relations [35]

$$M = m_s \mathcal{G} \frac{(9\eta r_s + 4\mathcal{G} + 3r_s)(3r_s + 4)}{4(4\mathcal{G} + 3r_s)(3r_s + 1)} \tag{1.9}$$

where

$$r_s = \frac{(1+\nu_s)}{3(1-2\nu_s)} \tag{1.10a}$$

$$\mathcal{G} = \frac{1}{2} - \frac{5}{4}(1-\eta) - \frac{3}{16}r_s(2+\eta) + \frac{1}{16}\sqrt{144(1-r_s) - 480\eta + 400\eta^2 + 480r_s\eta - 120r_s\eta^2 + 9r_s^2(2+\eta)^2} \tag{1.10b}$$

Constantinides and Ulm [34] showed that equation 1.6 was insensitive to the value of poission's ratio ν_s. For $\nu_s = 0.2$, equation 1.6 simplifies to

$$M(m_s, \eta) = m_s(2\eta - 1) \tag{1.11}$$

Using non-linear micromechanics, Cariou et al. [44] have developed a scaling relation for indentation hardness

$$H(c_s, \alpha, \eta) = c_s\Pi[1 + (1+\eta)\alpha_s - (d - e\eta)\alpha_s^2 - (f - g\eta)\alpha_s^5] \tag{1.12}$$

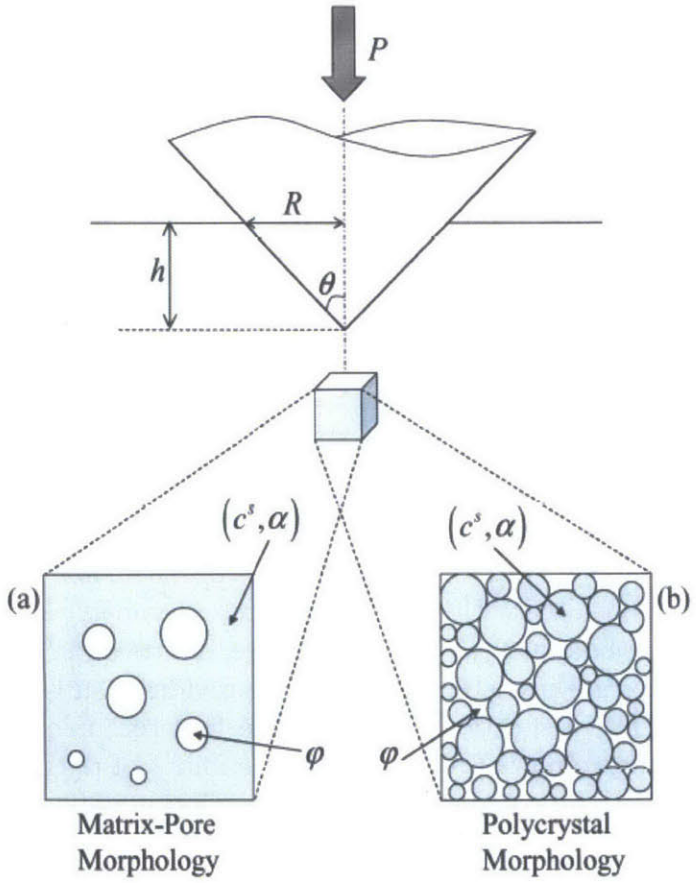

Figure 1.10: Indentation of porous materials. Two different morphologies (A) Matrix-porosity (B) Random packing or Polycrystal. Adapted from [44].

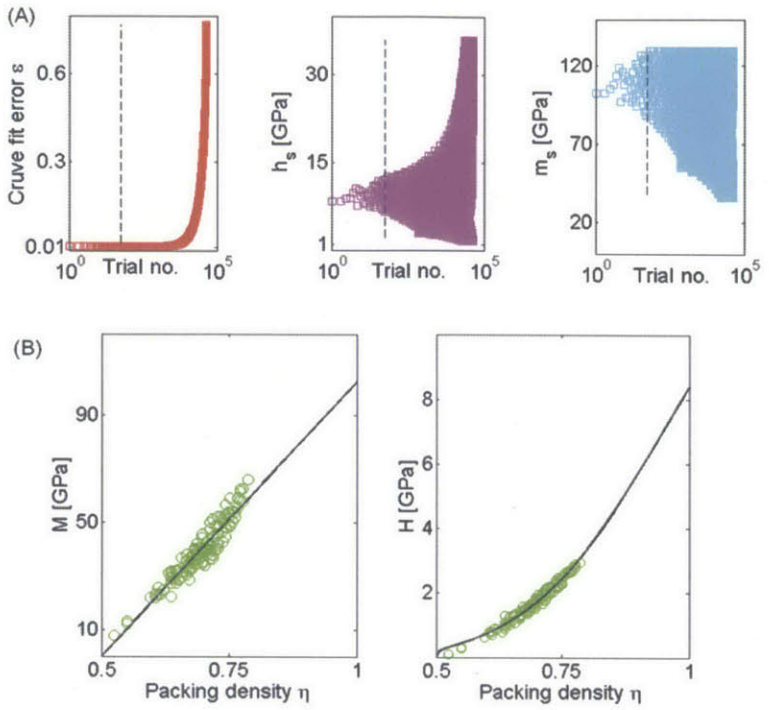

Figure 1.11: (A) Several trial micromechanics models with different values of parameters m_s, c_s and α were fit against nanoindentation data subset corresponding to C-S-H phase, $\{M_i\}$ and $\{H_i\}$ and subsequently enumerated in ascending order of fitting error ϵ. Trial 1 is the best fitting model that fits the data with the least curve fit error, ϵ_{min}. The models to the left of dotted line fit the data with $\epsilon < 1.01\epsilon_{min}$. (B) Best fitting model (solid line) plotted with experimental data (green circles) to show goodness of fit.

where

$$\Pi = \frac{12\eta(a - b\eta)\sqrt{(2\eta - 1)(2 + \eta)}}{(1 - c\eta)(2 + \eta)}$$

and $a = 0.19567, b = 0.03739, c = 077999, d = 20.3138, e = 31.5352, f = 52.1817,$ and $g = 99.3465$ are all constants associated with Berkovich indenter geometry and percolation threshold of random packing morphology, $\eta_0 = 0.5$. In practice, our M and H dataset from nanoindentation subjected to mixture modelling algorithms provides a subset associated with the C-S-H phase, $\{M_i\}$ and $\{H_i\}$ respectively. We seek to find the unique intrinsic properties of C-S-H nanoparticle $m_s, c_s,$ and α_s. We generate a number of trial models with different values of these parameters. The corresponding scaling relation is fit to the $\{M_i\}$ and $\{H_i\}$ data subset corresponding to C-S-H phase. There are is a unique set of values $\{m_s^0, c_s^0 \alpha_s^0\}$ of C-S-H nanoparticle that minimize the fitting error ϵ defined as

$$\epsilon(\{M_i\}, \{H_i\}, \{\eta_i\}, m_s, c_s, \alpha_s) = \frac{1}{m}\Sigma_{i=1}^{m}\sqrt{\left\{\frac{M(m_s, \eta_i) - M_i)}{< M >}\right\}^2 + \left\{\frac{H(c_s, \alpha_s, \eta_i) - H_i)}{< H >}\right\}^2} \tag{1.13}$$

where $M(m_s, \eta_i)$ and $H(c_s, \alpha, \eta_i)$ are given by equations 1.8 and 1.9 respectively, m is the cardinality of $\{M_i\}$ and $\{H_i\}$, and $< M >$ and $< H >$ are respectively the means of $\{M_i\}$ and $\{H_i\}$. We denote the minimum error $\epsilon(\{M_i\}, \{H_i\}, \{\eta_i\}, m_s^0, c_s^0, \alpha_s^0)$ as ϵ_{min}. We arrange trial models in ascending order of their corresponding ϵ (See Figure 1.11A). Thus, model 1 has fitting error ϵ_{min}. There are a finite number of models with ϵ within 1% of ϵ_{min} (dashed line in Figure 1.11A). The ranges of values of m_s obtained from these models are fit to a normal distribution to obtain mean μ_m and standard deviation, σ_m and thus, the coefficient of variation $c_v^m = \sigma_m/\mu_m$. The central hypothesis of micromechanics extrapolation is the existence of C-S-H nanoparticle with unique values of intrinsic properties m_s^0, c_s^0 and α_s^0 that can account for our nanoindentation data, $\{M_i\}$ and $\{H_i\}$. We consider this hypothesis to be validated, and thus the micromechanics extrapolation to be successful only when $\epsilon_{min} < 0.02$ and $c_v^m < 0.1$. These criteria are *posteriori* empirical criteria discussed in the context of results that we obtained in section 2.2. The essence of these criteria is to impose upper bounds on the uncertainity in the calculated properties m_s^0 and h_s^0 of C-S-H. The goodness of fit of the micromechanics model to the experimental data can be seen in Figure 1.11B.

1.5.2 Composition of C-S-H - Electron Probe Microanalysis

Electron Probe Micro-Analysis (EPMA) is an analytical technique used primarily for the *in situ*, non-destructive analysis of chemical composition and topography at length scales similar to nanoindentation. The similarity of interaction volumes between nanoindentation and EPMA allows easy investigation of the correlation between mechanical properties and chemical composition. A beam of electrons is accelerated to the surface of the sample of interest. X-rays produced by the interaction between the beam of electrons and the sample are characteristic of the local chemical composition of the sample.

In practice, EPMA is classified into two based on the x-ray detection method used: (1) Energy Dispersive Spectroscopy (EDS), and (2) Wavelength Dispersive Spectroscopy (WDS). As the name suggests, EDS classifies x-rays based on their energy. The detector converts the x-ray photons into a charge pulse which is subsequently converted to a voltage pulse. Each element is associated with a characteristic voltage pulse and the its mass fraction is proportional to the amplitude of the corresponding voltage pulse. On the other hand, WDS separates the x-ray photons based on their wavelength. Each element has characteristic wavelength(s) of x-ray photons and they are filtered by Bragg diffraction on special crystals. As a result, the x-ray detector in WDS analyzes elements one at a time. Filtration by Bragg diffraction also minimizes other spectral artifacts inherent in EDS [2]. Thus, EDS is typically used for high-throughput qualitative elemental mapping while WDS is used for accurate quantitative determination of composition. In our studies, we use EPMA with WDS.

EPMA has been used by a number of researchers to analyze the composition of cement hydration products. The major constituents of OPC paste are C-S-H, CH and unreacted clinker. There are minor hydration products resulting from the hydration of aluminate and ferrite phases. Al_2O_3- Fe_2O_3-mono or simply AFm phases have the general formula (in cement chemistry notation) $C_4(A,F).X_2.yH$ where X $\in \{OH^-, SO_4^{2-}, CO_3^{2-}\}$. The 'mono' label refers to single formula unit of singly charged anion or half a formula unit of a doubly charged anion. Similarly, there are Al_2O_3- Fe_2O_3-tri or simply AFt phases with three formula

units of anion X. A notably important AFt phase is ettringite $C_3A.3C\bar{S}.32H$ which forms in early stages of OPC hydration. In cement pastes where significant amount of OPC is replaced by supplementary cementitious materials with significant Al/Fe content like fly ash, blast furnance slag etc, AFm and AFt phases play a dominant role in the cement paste microstructure. In the interest of work that follows this chapter, we discuss AFm and AFt phases only in the context of their interaction with the C-S-H phase.

Early reports of EPMA reported considerable scatter of Ca/Si ratio of C-S-H between individual analyses [6]. Interestingly, Rayment and Majumdar noted that the ratio (Ca+Mg)/(Si+Al+Fe+S was nearly constant in contrast to Ca/Si [46]. They hypothesized that C-S-H was mixed with AFm and CH phases at sub-micron scale. Richardson and Groves [32], based on TEM + EDS studies on OPC pastes, reported several phases to be mixed with C-S-H at sub-micron scale. They conclude that Op and Ip C-S-H have (a) same C/S ratio, and (b) are embedded with other hydration products such as AFm, AFt and CH at EPMA scale of observation ($\sim 1\mu m$). Recently Chen et al., based on nanoindentation + SEM-EDS experiments on low w/c OPC pastes, noted the mixing of C-S-H and CH to form nanocomposites [47].

Our EPMA-WDS experiments were carried out at the MIT Electron Microprobe Facility by N. Chatterjee. For these experiments, we use the same surface preparation method as in the case of nanoindentation experiments. This surface is then coated with a 25 nm layer of graphite to prevent charging of the sample surface when exposed to electron beams. The heterogeneous nature of cementitious materials again requires a number of individual analyses, that is a grid based approach. The analogue of indentation depth is the accelerating voltage of electrons which determine the interaction volume. We chose it to be 15 kV using criteria similar to those listed for the choice of indentation depth. We probed our samples to identify the concentration of seven elements namely Ca,Si, Al, Fe, Mg, S and O.

A typical EPMA-WDS data set is shown in Figure 1.12A. The major crystalline phases have fixed compositions and C-S-H is known to have a composition within certain bounds. Note that C_3S is the only phase which appears to possess an isolated cloud or cluster of data points. This suggests that all the hydration products are extensively mixed at the micron scale at which we are investigating. The application of mixture modelling process to classify data points as belonging to different phases is therefore not straightforward. There are potentially seven variables (seven elements analyzed in EPMA-WDS) we could use to identify C-S-H, unlike in nanoindentation where there were two variables M and H. The question then arises as to what variables to use to define mixture models. In the case of nanoindentation, they were M and H. Initially, we attempted to use all the seven variables, i.e., compositions of seven elements as variables in our mixture modelling algorithm. Figure 1.12B shows the result of that process projected onto Ca-Si axes. The model then predicts existence of 13 different phases which is highly unlikely. We then attempted to use subsets of all elements. Figure 1.13B shows the results of mixture modelling process attempted using Ca,Si, and Al concentrations as variables. The model definitely predicts lesser number of phases. In this case, the mixturemodel identified 7 phases. Given there are three major phases, we can expect up to 7 phases if we additionally include 3 two phase mixtures and 1 three phase mixture. In Figure 1.13B, we can clearly identify the mixture phases. The phase represented by black circles is a mixture phase of C-S-H and AFm/AFt. The phase represented by blue circles is a mixture phase of C-S-H, CH and C_3S. This combination of elements however, predicted 10 phases or more in other samples with different composition

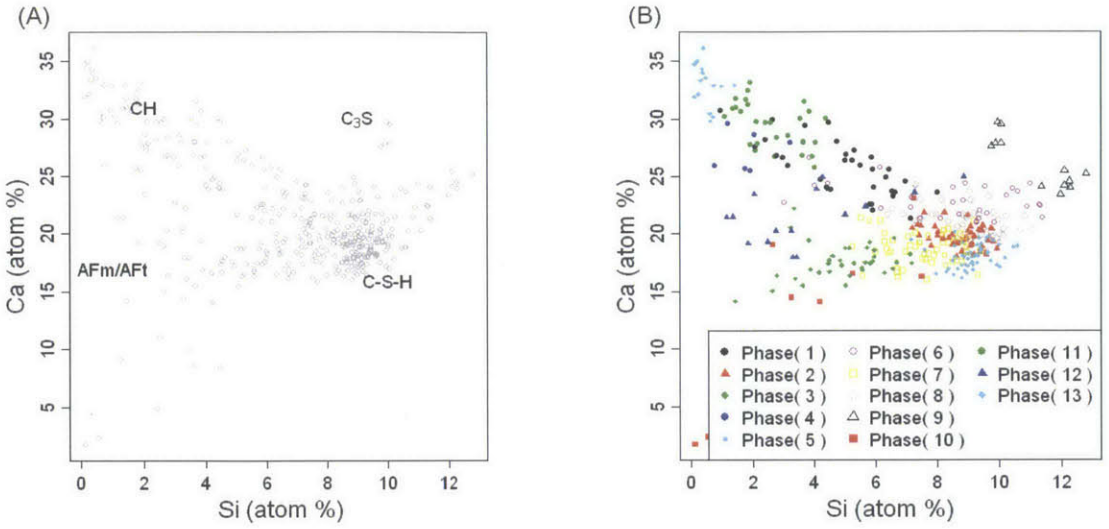

Figure 1.12: (A) Representative data set from EPMA - WDS experiment on an OPC paste with no supplementary cementitious materials projected on Ca-Si axes. The positions of major phases in this paste have been identified. (B) Mixture modelling using all seven elements as variables results in unrealistic prediction of number of phases in the paste.

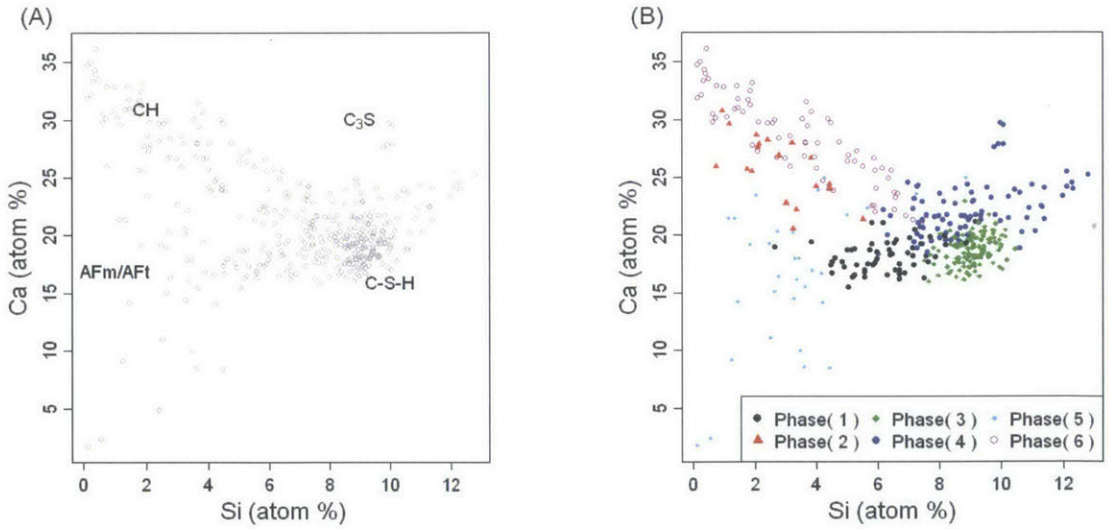

Figure 1.13: Same as in Figure 1.10 except concentration of Si, Ca and Al were used as mixture modelling variables. The phase represented by green diamonds is the C-S-H phase.

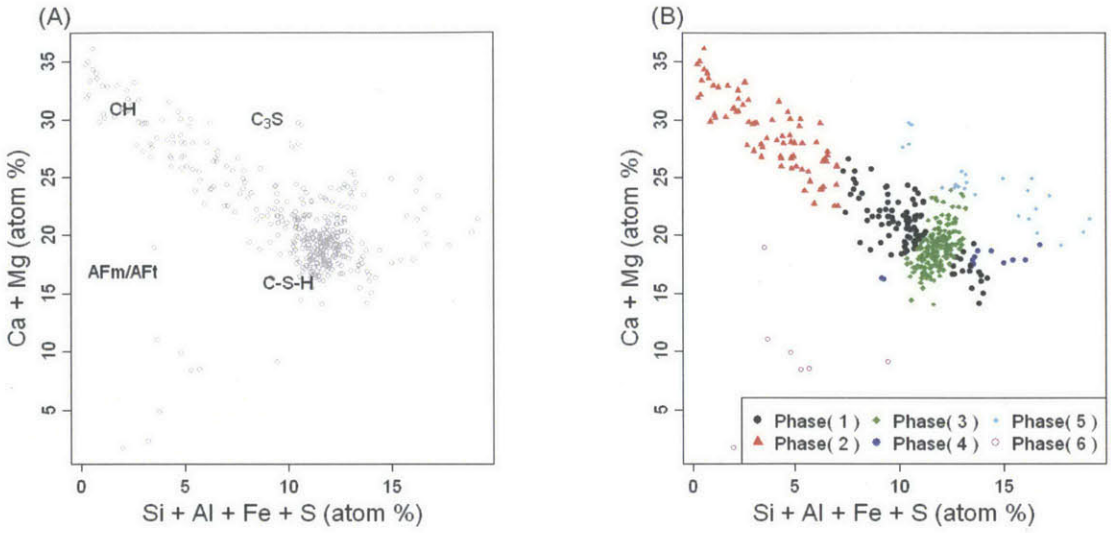

Figure 1.14: Same as in Figure 1.10 except concentration of Ca+Mg and Si+Al+Fe+S were used as mixture modelling variables. The phase represented by green diamonds is the C-S-H phase.

of cement precursors. We found no combination of variables that can be used to successfully model the EPMA-WDS data set our diverse set of samples.

Interestingly, we found that using Ca+Mg and Si+Al+Fe+S as two variables provided satisfactory results for all samples with different cement chemistries that were tested in this work. In all the cases, we noticed a tight cloud of data points in the region of Ca-Si plane where we expect the C-S-H phase (Figure 1.14B). The number of phases was below 7. As we pointed earlier, this has been observed earlier [46]. The physical basis for why this particular combination of atomic concentrations is able to best produce good mixture models can be multifold. We have repeatedly mentioned the mixing of several phases, notably C-S-H with AFm/AFt at a sub-micron scale. The role of Aluminum in bridging Si chains in C-S-H has been well documented [[48] and references therein]. Magnesium being similar, is known to substitute Calcium is several phases [6]. The roles of elements Fe and S have been debated [6]. Criteria for levels of solubility of these elements in C-S-H have been proposed [32], but they are highly empirical, and have not been robustly tested for cement precursors of different compositions. In this case, we do admit that the cluster of data points we identify as C-S-H phase has significant number of data points that could in principle be classified as belonging to CSH+AFm/AFt. However, this method is able to better predict an average C/S ratio for the C-S-H phase for various compositions of cement precursors.

1.6 Thesis Outline

The last section described the diversity of measured chemical composition of C-S-H. Although, studies have linked composition and morphological features, the relationship between composition and mechanical properties of C-S-H has not been explored. This is the subject of Chapter 2. We prepare a number of cement pastes to obtain C-S-H of various C/S ratios. We use nanoindentation to calculate the intrinsic mechanical properties of the C-S-H nanoparticle and then explore correlations between composition and properties of C-S-H. This could provide means to engineer mechanical performance of C-S-H through manipulation of its chemical composition. Given C-S-H is the principal binding phase in concrete, this could potentially have broad implications on engineering concrete properties.

In Chapter 3, we explore the applicability of C-S-H and concrete engineering to a specific application - designing infrastructural materials to sustain high temperatures and pressures experienced during explosions and blasts. Here, we characterize the properties of C-S-H in ultra high performance concrete (UHPC) and this once again exemplifies the correlation between composition and properties of C-S-H. Using nanoindentation, we also investigate the microstructure of UHPC. We find that steel fibers play an important role beyond enhancing ductility of UHPC.

Since C-S-H is a product of cement hydration reaction, its properties are ultimately controlled by this reaction. Although cement hydration reaction has been extensively studied, a quantitative kinetic model is still missing. In Chapter 4, we propose a novel technique based on optical microscopy and Raman spectroscopy to examine cement hydration kinetics at a microscale. We discuss preliminary results from those experiments.

The last chapter reflects on the principal results and their implications for future work.

Chapter 2

Chemomechanics of Calcium Silicate Hydrates

2.1 Introduction

Cement is a crucial component of concrete that reacts with water to generate Calcium Silicate Hydrates (C-S-H) necessary to bind together different components of concrete. The downside to use of cement in concrete is its the enormous carbon footprint of its manufacturing process. As we noted in the previous chapter, production of 1 ton of cement results in approximately 1 ton of CO_2. Coupled with the gigantic scale of concrete usage across the world (2 tonnes per capita) [2], the cement and concrete industry accounts for $\sim$ 5% of global man-made CO_2 emissions [49]. Carbon footprint of concrete is comprised of three factors:

$$\left[\begin{array}{c}\text{Mass of } CO_2 \\ (Tonnes) \\ \text{(I)}\end{array}\right] = \left\{\begin{array}{c}\text{Mass of concrete} \\ (Tonnes) \\ (A)\end{array}\right\} \times \left\{\begin{array}{c}\text{Wt\% of cement} \\ \text{in concrete (\%)} \\ (B)\end{array}\right\} \times \left\{\begin{array}{c}CO_2 \text{ per ton} \\ \text{of cement (\%)} \\ (C)\end{array}\right\} \tag{2.1}$$

In other words, to reduce the carbon foot print of concrete (I), we broadly have three levers. The consumption of concrete, lever (A), is projected to grow largely due to the growth of developing economies [49] and therefore, would not contribute to reducing the carbon footprint, (I). Current sustainability efforts are predominantly directed at lever (C), which translates to minimizing the energy consumption of the cement manufacturing process [49]. The potential of lever (B), i.e., proportion of cement used in the concrete mix is a materials design problem that has largely been unexplored.Given that the essential role of cement in concrete is producing C-S-H, the principal binding phase, optimizing the properties of C-S-H could reduce (I) through lever (B). With that goal in mind, this chapter explores the stiffness and hardness of the C-S-H phase and their relationship with composition of C-S-H, specifically its Ca/Si. Given the inherent variability in properties of C-S-H due (in theory) to variations in its structure and composition, we note that optimizing properties of C-S-H is only part of the solution together with defining methods and protocols that repeatably produce the C-S-H phase with those optimum properties.

Given the lack of such methods due in part to limited fundamental understanding of

the C-S-H phase, the recently proposed molecular model of C-S-H [31] was a resource that guided our experiments. This development allowed systematic exploration of the influence of various structural and compositional characteristics of C-S-H on its mechanical properties. These simulations predict that: (1) Ca/Si of the C-S-H phase does not uniquely determine its mechanical properties, and (2) the hardest and stiffest C-S-H phase occurs at Ca/Si $\sim$ 1.5. We attempted to validate these predictions by synthesizing cement pastes with C-S-H phases of diverse Ca/Si ratios. Further, we explored if cement pastes can be controlled to reliably produce stiff and hard C-S-H phase and/or C-S-H phase of a specific Ca/Si ratio. These experimental results will be the focus of this chapter. In the discussion section, these results will be interpreted using a theoretical framework developed from the results of molecular simulations by our collaborators R. Pellenq, R. Shahsavari, and M. Qomi (MIT).

The experiments presented in this chapter involved the efforts of several personnel. In order to obtain C-S-H phases of different Ca/Si ratios, we synthesized several cement pastes. We received a batch of cement pastes from CIMPOR - Cimentos de Portugal SGPS SA, Portugal. Subsequently, nanoindentation on specimens from these pastes were carried out by Drs. K. Stewart and M. Qu. A second batch of cement pastes was prepared at MIT. The synthesis of these pastes was designed by Dr. S. Musso, and carried out by Dr. S. Musso and J. Estrada along with the author. Nanoindentation on specimens from these pastes were performed by the author together with J. Estrada. Electron probe microanalysis with wavelength dispersive spectroscopy (EPMA-WDS) on all pastes was carried out at MIT Electron Microprobe Facility[3] by Dr. N. Chatterjee. The analysis of data from experiments on all pastes was performed by the author using programs developed by Dr. J. A. Ortega.

2.2 Materials & Methods

In an attempt to create C-S-H phases with different Ca/Si ratios, we explored several factors such as clinker composition, water/cement (w/c) ratio, curing temperature, quantity and composition of additives, and pH of mixing water. In order to allow for a systematic variation of these factors, we designed a subset of these samples using full factorial experimental design approach and another subset using the Taguchi experimental design approach. Before describing these methods, there are two terms that need to be defined: factors and levels. Factors are variables (like those listed above: clinker composition, w/c ratio, curing temperature etc.) whose influence on the outcome (in this case Ca/Si) is what we seek in our experiments. In these experiments, we will vary the state of these factors (e.g.: different clinker compositions and w/c ratios) and these various states of factors are called levels. When testing small number of factors n with few levels m ($n, m \in \{1, 2, 3\}$), we use full factorial design where we perform m^n experiments to test every possible combination of factors [50]. Such experiments become expensive to carry out when m and n become large. Full factorial design is best used when each factor significantly influences the outcome and the interaction between factors are strong [50]. For intermediate number of factors ($n \in [3-50]$) with few levels ($m \in \{1, 2, 3\}$), the Taguchi design of experiments is used. This method tests every combination of pair of factors in stead of every combination of every factor, like in the full factorial design. Taguchi design of experiments was conceived from a quality control method proposed by Taguchi [51] to determine the major factors that affected quality of a

product in a manufacturing environment with the least number of experiments. The biggest advantage of using the Taguchi method is the significant reduction in number of experiments. For instance, when testing the effects of $n = 6$ factors with $m = 2$ levels, the full factorial design requires $2^6 = 64$ experiments, while in Taguchi experimental design needs only $N = 8$ experiments. Such an array of N experiments is represented as L_N. For various values of m and n, the appropriate Taguchi matrix to be chosen can be found in Refs. [50, 51]. There is no analytical experession relating N to m and n. After obtaining the outcomes y_j of N experiments of the Taguchi L_N array ($j \in [1-N]$), we can deduce the influence of each factor and its optimal level through signal over noise factor S/N. The analytical expression for S/N of a factor n_0 at level m_0 depends on whether we wish to maximize, minimize or attain a target value of the outcome. In that order, the expressions for S/N are given by [51]:

$$S/N_{\text{maximize}}(n_0, m_0) = -log\left[\frac{1}{l}\sum_{i=1}^{l}\frac{1}{y_i^2}\right] \tag{2.2}$$

$$S/N_{\text{minimize}}(n_0, m_0) = -log\left[\frac{1}{l}\sum_{i=1}^{l} y_i^2\right] \tag{2.3}$$

$$S/N_{\text{y = y0}}(n_0, m_0) = -log\left[\frac{1}{l}\sum_{i=1}^{l}(y_i - y0)^2\right] \tag{2.4}$$

where l is the number of experiments in which the factor n_0 is set to level m_0, $l \leq \lfloor N/2 \rfloor^4$. For each factor n_0, we calculate a set of m S/N values, $\{S/N\}_{n_0}$, corresponding to each of the m levels. The level m_O that satisfies $S/N(n_0, m_0) = \max[\{S/N\}_{n_0}]$ is the optimal level among m levels for factor n_0 to achieve our objective for the outcome. Once we determine the optimal levels of each factor, we perform a final experiment with each of the n factors set to their optimal levels. If the outcome y_{final} of this experiment, meets our objective, i.e., maximize y or minimize y or attain $y = y0$, the Taguchi experimental design is deemed a success. We can also deduce the most influential factor on the outcome as the factor n_i with the largest range of $\{S/N\}_{n_i}$ among the n factors. Taguchi design of experiments is known to work best when some among n factors contribute significantly to the outcome y and the interactions among factors are weak [50].

As noted above, the first batch of cement pastes were prepared at CIMPOR - Cimentos de Portugal SGPS SA, Portugal. We used two full factorial design matrices. For the first, we use alite content (clinker composition) and w/c ratio as two factors each varied at two levels. We used an alite rich clinker (labelled as A') and a belite rich clinker (labelled as B') as two levels of the alite content factor. A' is comprised of 65.3% C_3S, 13.5% C_2S, 7.1% C_3A and 8.6% C_4AF while B' is comprised of 6.3% C_3S, 71.2% C_2S, 9.1% C_3A and 11% C_4AF, as determined by Bogue calculation [52]. We chose 0.3 and 0.4 as two levels for w/c factor. We used 100 g of cement clinker to prepare these samples. For the second full factorial design matrix, we chose alite content, w/c ratio and additive chemistry as three factors with two levels for each factor. We again used A' and B' as two levels of alite content. We chose 0.4 and 0.5 as levels for w/c ratio. We chose NaOH (labelled as NH) and Na_2SiO_3 (labelled as NS) solution as two levels for additives. For these samples, we first mixed 100 g of cement clinker with water at a w/c of 0.3. For samples with NaOH as additive, we then added either

Name	*Clinker*	*w/c*	*Additive*
A'30NO	C_3S rich	0.30	None
A'40NH	C_3S rich	0.40	NaOH
A'40NO	C_3S rich	0.40	None
A'40NS	C_3S rich	0.40	Na_2SiO_3
A'50NH	C_3S rich	0.50	NaOH
A'50NS	C_3S rich	0.50	Na_2SiO_3
B'30NO	C_2S rich	0.30	None
B'40NH	C_2S rich	0.40	NaOH
B'40NO	C_2S rich	0.40	None
B'40NS	C_2S rich	0.40	Na_2SiO_3
B'50NH	C_2S rich	0.50	NaOH
B'50NS	C_2S rich	0.50	Na_2SiO_3

Table 2.1: Summary of samples prepared using full factorial design matrices at CIMPOR - Cimentos de Portugal SGPS SA, Portugal. We adopt a three part sample name to uniquely label each sample. The first part identifies the clinker composition using a letter: A' - Alite rich clinker, B' - Belite rich clinker (see text for details). The second part expresses the w/c ratio in % terms. The third part identifies the additive using two letter labels: NO - No additives, NH - Sodium Hydroxide, NS - Sodium Silicate.

10 mL or 20 mL of 5M NaOH to the cement paste resulting in a final w/c of 0.4 and 0.5, respectively. For samples with Na_2SiO_3 as additive, we added 16 mL or 30 mL of saturated Na_2SiO_3 solution resulting in a final w/c of 0.4 and 0.5, respectively. Thus, we created 12 different cement paste samples using two full factorial designs. These are summarized in Table 2.1.

Further, to deduce the optimal levels for cement paste synthesis factors to reliably produce the C-S-H phase with the highest stiffness and hardness, and Ca/Si ratio of 1.5, we use a L16 Taguchi array with $n = 5$ factors and a maximum of $m = 4$ levels for each factor. This second batch of 16 samples were synthesized at MIT. For this experimental design, we chose clinker composition, w/c ratio, curing temperature, pH of hydration water and fly ash type as our five factors. We investigated clinker composition at four levels: pure monoclinic C_3S (labelled as A), ordinary portland cement (labelled as G), white cement (labelled as W), and pure β-C_2S (labelled as B). We used four w/c ratios: 0.34, 0.37, 0.40, and 0.43. Curing temperature was varied among 5, 20, 40 and 60°C. pH of mixing water was either 4 or 7. 8 samples were prepared without fly ash. Four samples were prepared with Class F flyash with high % of activated carbon (labelled as FH) and 4 more were prepared with Class F flyash with low % of activated carbon (labelled as FL). Thus, our fractional factorial design yielded 16 cement paste samples. Table 2.2 summarizes our implementation of Taguchi L16 array.

Cement pastes were obtained using 40 g of solid mixed with water in the proportion dictated by the Taguchi experimental array. In samples containing fly ash (class F), the solid mixture contained 30% by weight of fly ash. Deionized water was used for hydrating

water. HCl (1M) was added to deionized water to prepare solution of pH = 4. The mixture was poured in a 50 ml centrifuge tube that was then mounted onto a vortex mixer[5]. Mixing was performed for five minutes at $\sim$ 2500 rpm. Subsequently, the pastes were cast into Petri dishes (diameter 35 mm and height 10 mm) and tapped against a hard surface in order to remove any macroscopic air bubbles. These samples were then placed in large air tight plastic container and left undisturbed for one day. Some water was added to the container before closing the lid so as to maintain high humidity inside the container. After a day, all samples except those prepared from pure β-C_2S had become solid. Notches were created along the rim of Petri dishes using a rotary tool. Samples were then demolded from the weakened Petri dishes by hand. They were then allowed to cure in lime water for 28 days at specific temperatures as required by the experimental design array. Solvent exchange with isopropanol described elsewhere [53] was used to stop hydration. To minimize levels of carbonation, samples were stored in vacuum and were exposed to normal atmosphere (for < 1 hr) only when specimens were cut from them for experiments. For nanoindentation and EPMA-WDS experiments, specimens were prepared in the Metallography Lab in Center for Materials Science & Engineering at MIT. Sections of $\sim$ 1 $\times$ 1 $\times$ 0.5 cm were cut from samples using a diamond saw[6] with absolute ethanol as a coolant to avoid excessive heating

Sample	*Clinker*	*w/c*	*Additive*	*Temp. (°C)*	*pH*
A34NO	pure C_3S	0.34	None	40	4
A37FL	pure C_3S	0.37	Class F Fly ash + low C	20	7
A40FH	pure C_3S	0.40	Class F Fly ash + high C	05	4
A43NO	pure C_3S	0.43	None	60	7
B34FL	pure C_2S	0.34	Class F Fly ash + low C	60	4
B37NO	pure C_2S	0.37	None	05	7
B40NO	pure C_2S	0.40	None	20	4
B43FH	pure C_2S	0.43	Class F Fly ash + high C	40	7
G34NO	OPC	0.34	None	05	7
G37FH	OPC	0.37	Class F Fly ash + high C	60	4
G40FL	OPC	0.40	Class F Fly ash + low C	40	7
G43NO	OPC	0.43	None	20	4
W34FH	white cement	0.34	Class F Fly ash + high C	20	7
W37NO	white cement	0.37	None	40	4
W40NO	white cement	0.40	None	60	7
W43FL	white cement	0.43	Class F Fly ash + low C	05	4

Table 2.2: Summary of Taguchi L16 array of cement paste samples prepared at MIT . We adopt a three part sample name to uniquely label each sample. The first part identifies the clinker composition using a letter: A - Pure monoclinic C_3S, B - pure β-C_2S, G - OPC, and W - White cement. The second part expresses the w/c ratio in % terms. The third part identifies the additive using two letter labels: NO - No additives, FH - Class F Fly ash with high % C, FL - Class F Fly ash with low % C. For details on compositions and sources of these materials, please refer to Appendix A.

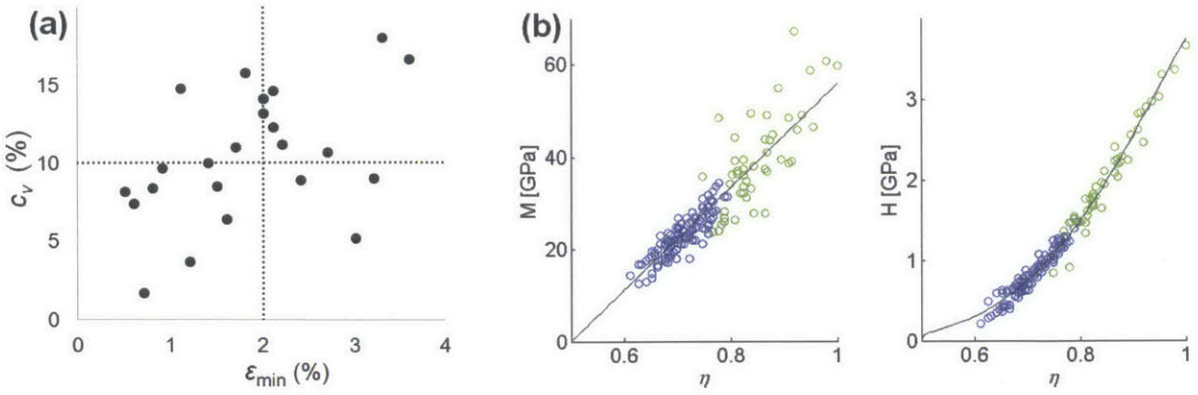

Figure 2.1: Choice of upper bound for $\epsilon_{\min}$ based on chosen upper bound for c_v. A) Variation of c_v with $\epsilon_{\min}$ in 24 cement pastes we tested . The dotted lines represent $\epsilon_{\min} = 2$ and $c_v = 10$. B) In samples with $c_v < 10$ and $\epsilon_{\min} > 2$, mixture modelling algorithm identified more than one phase with $M \in [25 - 35]$ and $H \in [0.5 - 1.5]$ shown here with two different colors blue and green. We attempted to fit the micromechanics model to the combination of data points corresponding to both phases. The green data points do not fit the micromechanics model (black line) well in the $M - \eta$ plot resulting in higher $\epsilon_{\min}$. This is possibly a result of mixing between C-S-H and Portlandite. The micromechanics model is invalid in such instances because it applies to only the C-S-H phase. We discount such instances by setting an upperbound of $\epsilon_{\min}$ at 2%.

of samples. Surfaces of less than 50 nm roughness were obtained using a polishing procedure described in ref. [39].

The nanomechanical properties of cement samples were measured using a commercially available indenter [7]. A Berkovich diamond probe was used for indentation. Parameters used for the indentation experiments were: maximum load = 2 mN, loading rate = 12 mN/min, dwell time at maximum load = 5 s, and unloading rate = 12 mN/min. We carried out 1000 individual indentations on each sample on a 20 × 50 grid where the indents were spaced 20 μm apart. Load-depth response curves containing jumps and discontinuities were discarded. Indentation modulus M and hardness H values were extracted from the remaining load-depth response curves using the Oliver-Pharr method [54].

Analysis of nanoindentation data detailed in Chapter 1 is briefly reviewed here. The subset of data corresponding to the C-S-H phase is extracted using clustering algorithms. We use a micromechanics model to predict the stiffness and hardness of the C-S-H nanoparticle from nanoindentation data corresponding to the C-S-H phase. We explore the goodness of fit of several micromechanics models with different values of parameters m_s and h_s. There is a unique model with parameters m_s^0 and h_s^0 that fits the nanoindentation data with least fitting error ϵ_{min}. There are a finite number of models with fitting error within 1% of ϵ_{min}. The range of m_s values from these models, $R_{m_s^0}$, is used to determine the coefficient of variation c_v of m_s^0 as the ratio of standard deviation σ and mean μ of $R_{m_s^0}$. We found the corresponding coefficient of variation of h_s^0 to be proportional to coefficient of variation of m_s^0 with a constant proportionality factor of approximately 2. Hence, we make a reference to

just c_v in the text that follows all the while noting that similar considerations apply to the coefficient of variation of h_s^0. For the given nanoindentation data, we deem the hypothesis of existence of the C-S-H nanoparticle with properties with unique mechanical properties to be fulfilled only when the following three criteria are met: (1) predicted median packing density of C-S-H, η_{med}, satisfies $0.6 \leq \eta_{med} \leq 0.85$, (2) $\epsilon_{min} \leq 2\%$ and (3) $c_v < 10\%$. The first criterion ensures that the predicted packing density of C-S-H is realistic [34]. The second and third are *posteriori* empirical criteria to impose upper bounds on the uncertainty in calculated values of m_s^0 and h_s^0. The uncertainty in m_s^0 (h_s^0) cannot be rigorously defined as it a result derived from a mathematical model. We chose $c_v \times < R_{m_s^0} >$ to represent the standard deviation of m_s^0. A upper bound on c_v is thus, an upper bound on the standard deviation of m_s^0 at approximately 10% of m_s^0. Interestingly, in all samples that satisfied $c_v < 10\%$, ϵ_{min} was less than 2% (Figure 2.1A) except in three samples: G43NO, A'50NH, and B'40NH. In these samples with, we could not obtain a single cluster or cloud of data points belonging to C-S-H in the typical range $M \in [25 - 35]$ and $H \in [0.5 - 1.5]$. In these instances, we fit data points belonging to two clusters to the micromechanics model. In samples with $\epsilon_{min} > 2\%$, possibly because it represented a mixture phase, one of the clusters did not fit the micromechanics model well (Figure 2B), elevating the value of ϵ_{min}. Since the micromechanics model is invalid in such instances, we empirically chose an upper bound of ϵ_{min} at 2%.

To assess the influence the cement paste synthesis factors on the composite mechanical properties of cement paste, we performed microindentation experiments on samples in the L16 array. These experiments are similar to nanoindentation experiments, but probe the cement paste at micron-scale depth. Thus, they assess the homogeneous composite properties of cement paste. These experiments were carried out at the Mechanics of Materials & Structures Laboratory in the Department of Civil Engineering at MIT. We used a commercially available microindenter [8]. Parameters used for the microindentation experiments were: maximum load = 2 N, loading rate = 12 N/min, dwell time at maximum load = 5 s, and unloading rate = 12 N/min. These loading conditions produced maximum indentation depths of around 5 μm. Given these responses are homogeneous, we performed 4 indentations on each sample on a 2×2 grid with a grid spacing of 0.2 mm. From the load-response curves, the indentation modulus $M_{\mu,c}$ and hardness $H_{\mu,c}$ were extracted using the Oliver-Pharr method [54].

We used EPMA-WDS to determine the Ca/Si of C-S-H in cement pastes. A 20 × 20 grid (400 probes, with 20 μm spacing) analysis was performed on each of the 28 samples. Before analysis the sample was coated with a 25 nm thick layer of graphite. Each probe collected signal for 10 seconds. In our analysis we collected data for up to seven different elements: Ca, Si, Al, Mg, Al, O, Fe, and S. Data corresponding to the C-S-H phase is extracted using clustering algorithms similar to those used in nanoindentation. Average Ca/Si and standard deviation $\sigma_{C/S}$ were extracted from the set of data points belonging to the C-S-H cluster. Note that we use the fraction {Ca + Mg}/{Si + Al + Fe + S} to represent the Ca/Si of C-S-H (see section 1.5.2).

We use magic angle spinning (MAS) NMR spectroscopy to understand the silicate chain structure in C-S-H [55]. NMR probes the local structural environment of a material at the atomic level [56]. A sample is placed in a high external magnetic field, thereby causing a splitting of the energy levels for the various spin states in nuclei with non-zero nuclear spins

(e.g., ^{29}Si, ^{27}Al, ^{1}H). When pulses of electromagnetic radiation are imposed on the sample under this condition, energy is absorbed at specific resonance frequencies, reported as chemical shifts. In cementitious materials, the ^{29}Si chemical shift is predominantly dependent on the atomic environment of the silicon- oxygen tetrahedra, denoted by Q_n, where n represents the number of bridging oxygen atoms [57]. This is represented schematically in Figure 2.2. Anhydrous C_3S or C_2S consists of only Q_0 groups. C-S-H consists of Q_1 and Q_2 groups. Each Q_n group has its characteristic NMR signature. Note that silicate chains in C-S-H are one-dimensional and there are no Q_3 and Q_4 groups [22]. With the proportion V_1 of different Q_n groups in a paste, one can determine the average silicate chain length l_{Si} as

$$l_{Si} = 2 \times (1 + V_2/V_1). \tag{2.5}$$

To study silicate groups in hydrated products only, a special NMR technique known as ^{1}H-^{29}Si cross polarization (CP) MAS NMR is used. This is a double resonance experiment

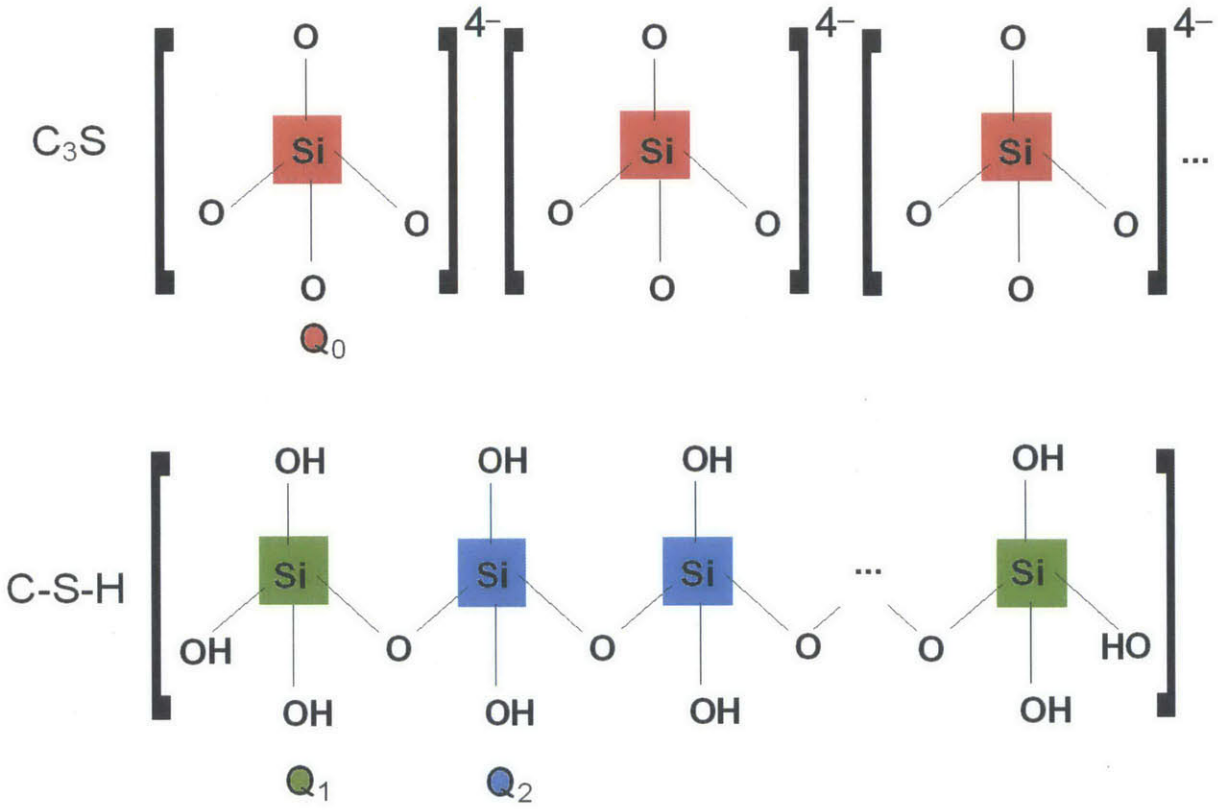

Figure 2.2: Si atoms in ^{29}Si MAS NMR spectroscopy are labelled as Q_n where n represents the number of bridging O atoms (that are bonded to two Si atoms). In anhydrous C_3S (and C_2S), silicate tetrahedra exist as individual SiO_4^{4-} units and hence the corresponding Si atoms are labelled Q_0 (red). In C-S-H, there are two types of Si atoms. Q_1 (green) bonded to one bridging O atom occur at the end of silicate chains. Q_2 (blue) bonded to two bridging O atoms occur in the middle of the silicate chains between two Q_1 ends. We refer to the ensemble of Q_n Si atom with its four O atoms as Q_n group.

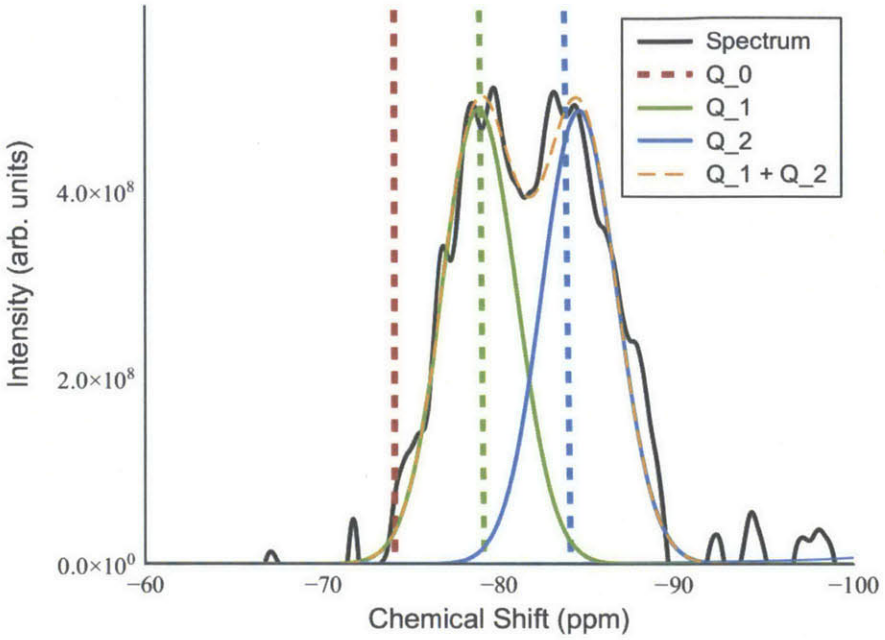

Figure 2.3: ^{29}Si-^{1}H CP MAS NMR spectrum of B'40NO (black solid line). Q_0 (red), Q_1 (green), and Q_2 (blue) have their characteristic signatures near -74, -79, -84 ppm, respectively (dashed lines) [23]. The recorded spectrum has been deconvoluted as sum of two gaussian peaks (green and blue) centered around -78.9 and -84.6 ppm, identified as Q_1 and Q_2, respectively.

in which energy is transferred from ^{1}H nucleus to ^{29}Si nucleus, and thus requires them to be in close proximity. This condition is not fulfilled in anhydrous silicates and hence, only silicates from C-S-H contribute to the NMR spectrum. Our CP MAS NMR experiments were performed by Dr. J. Struppe at Bruker Biochem Corp., Billerica MA.

Each silicate group Q_n has a characteristic NMR signature [23]. Figure 2.3 shows a CP-MAS NMR spectrum of B'40NO along with the reference signatures expected for Q_0. Q_1, and Q_2. The absence of Q_0 groups in CP experiments was explained above. We note that this spectrum is dominated by two peaks near -79 ppm and -84 ppm, the characteristic signatures of Q_1, and Q_2 groups, respectively. We use a curve fitting program[9] to deconvolute the observed spectrum as a sum of two Lorentzian [10] peaks. These peaks are shown in red and blue in Figure 2.3. The proportion of V_n of Q_n groups is then calculated as the ratio of area enclosed under the Lorentzian peak corresponding to Q_n and the total area enclosed by the sum of all Lorentzian peaks.

2.3 Results & Discussion

Here, we discuss the results on nanoscale properties of the C-S-H phase and Taguchi experimental design. Then, we compare select results of our experiments with results from

molecular simulations. Finally, we explore the correlation between the measured nanoscale mechanical properties of the C-S-H phase with the microscale mechanical properties of cement paste.

Sample	Mechanical Properties		Chemical Properties		Micromechanics		
	$\mathbf{m_s}$ **(GPa)**	$\mathbf{h_s}$**(GPa)**	**Ca/Si (atomic)**	$\sigma_{\mathbf{C/S}}$	ϵ_{min} (%)	c_v (%)	η_{med}
A34NO	93.96	7.26	1.8	0.1	1.4	10.0	0.67
A37FL	88.42	9.47	1.71	0.4	1.7	11.0	0.68
A40FH	80.1	7.59	1.71	0.08	2.7	10.7	0.69
A43NO	77.33	6.73	1.68	0.1	0.7	1.7	0.67
A'30NO	89.63	7.15	1.61	0.14	1.2	3.7	0.75
A'40NH	57.92	3.43	1.7	0.26	2.2	11.2	0.75
A'40NO	105.05	8.06	1.62	0.19	0.6	7.4	0.72
A'40NS	57.88	4.38	1.53	0.28	2.1	12.3	0.73
A'50NH	55.15	3.59	1.52	0.19	3.0	5.2	0.68
A'50NS	91.03	9.66	1.52	0.16	3.3	18.0	0.58
B'30NO	46.83	2.31	1.66	0.14	0.5	8.2	0.87
B'40NH	46.84	3.26	1.36	0.21	3.2	9.0	0.67
B'40NO	105.05	10.46	1.68	0.1	0.8	8.4	0.65
B'40NS	49.61	3.69	1.41	0.27	3.6	16.6	0.73
B'50NH	66.24	8.85	1.51	0.25	2.1	14.6	0.55
B'50NS	74.56	4.05	1.38	0.08	4.7	16.6	0.62
G34NO	44.06	1.97	1.63	0.13	1.1	14.8	0.8
G37FH	88.41	5.36	1.29	0.08	1.6	6.4	0.66
G40FL	60.7	4.66	1.29	0.08	1.5	8.5	0.67
G43NO	71.8	4.75	1.66	0.13	2.4	8.9	0.68
W34FH	77.33	5.51	1.6	0.12	0.9	9.7	0.72
W37NO	38.52	2.29	1.87	0.2	2.0	13.2	0.64
W40NO	82.87	6.26	1.88	0.15	1.8	15.8	0.65
W43FL	80.1	5.51	1.77	0.25	2.0	14.1	0.66

Table 2.3: Fundamental nanoscale properties m_s, h_s and Ca/Si of C-S-H in our cement paste samples. The uncertainty in Ca/Si is calculated as the standard deviation $\sigma_{C/S}$ of Ca/Si among data points belonging to C-S-H cluster (See Materials & Methods). Micromechanics based extrapolation algorithm was deemed successful in finding unique values m_s and h_s for properties of the C-S-H nanoparticle only when $0.6 \leq \eta_{med} \leq 0.85$, $\epsilon_{min} \leq 2\%$ and $c_v \leq 10\%$ (see Materials & Methods). Cement paste samples that satisfied these criteria are in bold font. Our experimental results from these samples alone are compared to results from molecular simulations.

2.3.1 Ca/Si ratio of the C-S-H phase

Our experiments were able to produce cement pastes with varying Ca/Si ratios of the C-S-H phase. The maximum Ca/Si was 1.87 in W37NO and the minimum Ca/Si ratio was 1.29 in G37FH and G40FL (Table 2.3). We wanted to understand the cement paste synthesis conditions that repeatably produce C-S-H phase of a specific Ca/Si ratio. We observe the uncertainty in the measured Ca/Si ratio of the C-S-H phase ($\sigma_{C/S}$) to be variable (Table 2.3). In A37FL, $\sigma_{C/S} = 0.4$ with a coefficient of variation of 25%. In other samples with $\sigma_{C/S} \in [0.2 - 0.3]$, coefficient of variation of Ca/Siis less than 20%. For comparison, in a recent study of white portland cement pastes blended with fly ash using TEM-EDS, Girao et al. measure a Ca/Si ratio of the C-S-H phase as 1.49 with an uncertainty of 0.12. Note that even with the higher resolution that TEM affords, the uncertainties are comparable to some of our measurements ($\sigma_{C/S} \in [0.1 - 0.2]$ in Table 2.3). However, as described above uncertainty of Ca/Si in some other samples are significantly higher. At this point, we are unable to identify the precise factors causing such variations in $\sigma_{C/S}$.

Table 2.3 shows an instance of controlling factors in the synthesis of cement paste to produce C-S-H with low Ca/Si. Two samples produced the C-S-H phase with the lowest Ca/Si of 1.29: G37FH and G40FL. Synthesis of both these samples involved the use of grey cement and fly ash. Is that a sufficient condition to produce C-S-H of low Ca/Si? Considering the Ca/Si ratios of C-S-H measured in G43NO, G43NO, A40FH and A37FL it does not seem like either gray cement or fly ash is singularly able to produce such low Ca/Si ratios. Fly ash is known to produce low Ca/Si ratios through reaction of silicates with CH to form C-S-H (pozzalonic reaction) [6]. However, fly ash is also notorious for its low reactivity [58]. From Table 2.2, note that G37FH and G40FL were cured at 60 and 40°C, respectively. Curing at elevated temperatures is known to enhance fly ash's reactivity [58–61]. In white portland cement of w/s = 0.5 blended with 30% fly ash cured at 55°C for 28 days, Girao et al. [59] measured Ca/(Si + Al) of C-S-H as 1.26, remarkably close to our measurement of Ca/Si of the C-S-H phase in G37FH, 1.29. Note that Fe is absent in white cement which makes the ratio Ca/(Si + Al) similar to the ratio that we use to represent Ca/Si. Our measurements suggest that curing at 40°C can also produce such Ca/Si ratios as seen in G40FL. Other cement paste samples with FH or FL in our Taguchi L16 array were cured at 5 or 20°C. We do not see low Ca/Si of the C-S-H phase in these pastes. This clearly suggests an interaction between temperature and fly ash in influencing Ca/Si of C-S-H. Other results also suggest such interactions between different factors influencing Ca/Si of C-S-H. While Ca/Si of C-S-H in A'40NO and A'40NH are comparable within limits of uncertainty, there is a statistically significant difference between Ca/Si of C-S-H in B'40NO and B'40NH. In this case, the clinker composition and additive chemistry together have an influence on Ca/Si. We noted earlier that such interactions among factors to influence the outcome are not the strong suit of Taguchi experimental design. Let us now turn to results from our Taguchi experimental design to support or contradict the above statement.

2.3.2 Taguchi experimental design

Four samples involving pure β- C_2S did not set to become solid. To complete the L16 array and derive optimal cement paste synthesis conditions to produce desirable nanoscale

properties of C-S-H, we use hypothetical results for these samples. For the four samples involving β- C_2S, we used $m_s^h = 40$ GPa, $h_s^h = 2$ GPa and $Ca/Si^h = 1.7$, the superscript h indicating that these values are hypothetical. The values we used for m_s^h and h_s^h are close to the lowest values we observe for the respective quantities in Table 2.3. Belite hydration is known be similar to alite [6] except for its slower time frame. Hence, we assumed the Ca/Si^h of C-S-H in these samples to be 1.7. Note that by assuming identical results in all of the four β- C_2S samples, we are artificially inducing clinker chemistry to be the dominant factor in controlling the nanoscale properties of the C-S-H phase. Therefore, we do not analyze the ranges of $\{S/N\}_{n_i}$ of various factors to predict the most influential factor.

Objective	Optimal levels of factors			
	T (°C)	w/c	clinker	Additive
Maximize m_s	20	0.4	Grey	None
Maximize h_s	20	0.43	Grey	None
Ca/Si = 1.5	20	0.4	Grey	FH

Table 2.4: Optimal levels of different factors for various objectives. For each of these objectives, S/N for pH = 4 was approximately equal to S/N for pH = 7, implying pH of hydrating water has no effect on the nanoscale properties of the C-S-H phase.

Table 2.4 summarizes our analysis of the signal over noise ratios S/N for various factors at different levels. We determined the optimal levels for each of these factors to achieve three objectives: (1) maximize m_s, (2) maximize h_s, and (3) Ca/Si = 1.5. Variation of pH factor did not have any influence on the outcome of our experiments and so we do not include it in Table 2.4. The optimal levels of factors other than w/c are identical to achieve maximum m_s and h_s. The optimal levels of all factors except additives are identical to maximize m_s and produce C-S-H with Ca/Si = 1.5. To test the validity of the Taguchi method, we synthesized a new sample incorporating the optimal levels of factors needed to maximize m_s: G40NO, referred to in the text that follows as the α-sample. For the Taguchi method to be successful, at the very least, α-sample should produce the C-S-H phase with high m_s.

The nanoscale properties of the C-S-H phase in α-sample are summarized in Table 2.5. We draw a comparison with other samples that produced the stiffest and hardest C-S-H phase among samples in L16 array. With the α-sample producing the C-S-H phase that is

Sample	m_s	h_s	Ca/Si	$\sigma_{Ca/Si}$
α (G40NO)	72.20	4.50	1.7	0.1
A34NO	**93.96**	7.26	1.8	0.1
A37FL	88.42	**9.47**	1.71	0.4

Table 2.5: Comparison of nanoscale properties of C-S-H in *upalpha*-sample with those specific samples from L16. A34NO produced the C-S-H phase with highest m_s. A37FL produced the C-S-H phase with highest h_s. Bold font indicates highest m_s and h_s measured among samples in L16 array.

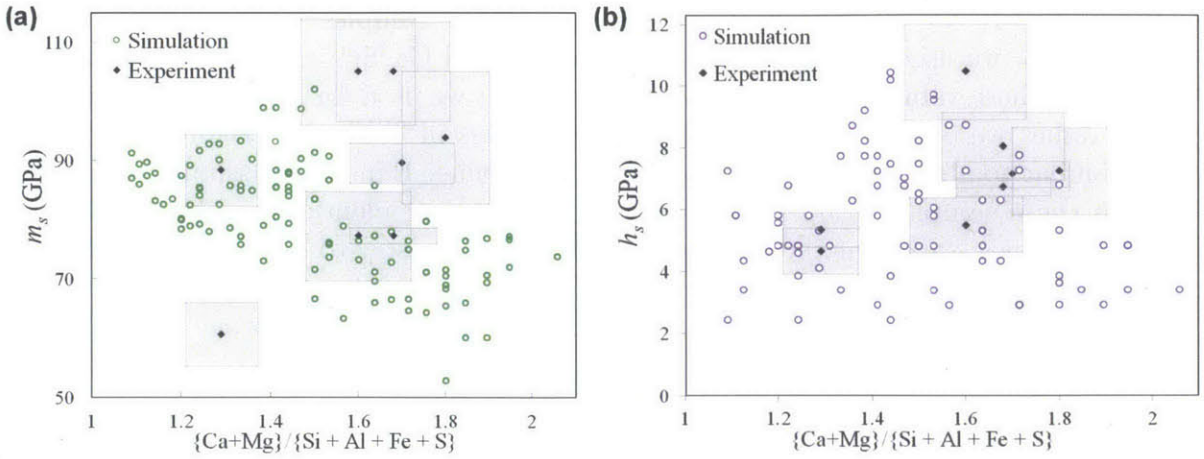

Figure 2.4: Over a range of Ca/Si from 1.2 to 2.1, (A) Indentation elastic moduli m_s and (B) Indentation hardness h_s of fully dense C-S-H agrees well with predictions from shear deformation simulations of C-S-H polymorphs. Grey shaded region represents the spread (uncertainty) in the calculated properties. The calculation of uncertainties of m_s and h_s are similar. In (A) the half-width of spread along m_s axis is calculated for each sample as $c_v \times < R_{m_s^0} >$. The half width along the Ca/Si axis is equal to $\sigma_{C/S}$. See Materials and Methods for more details. For results from molecular simulations, stiffness and hardness of the C-S-H nanoparticle calculated by R. Shahsavari for structures generated by R. Pellenq.

significantly less stiffer than that in A34NO, we can conclude the Taguchi experimental design failed to deliver expected results. This failure could be a result of our use of hypothetical values for nanoscale properties of the C-S-H phase in samples involving β-C_2S. Inspecting our analysis of S/N ratios *posteriori*, we found the results in Table 2.4 to be insensitive to $m_s^h \in [40 - 70]$ GPa and $h_s^h \in [2 - 4]$ GPa. This suggests that use of identical values for m_s^h and h_s^h in all of the four samples involving β-C_2S could be a reason for the failure of Taguchi S/N analysis. In that case, we can deduce that each of the factors strongly influences the outcome independently or they interact strongly to influence the outcome. We noted evidence of the latter in the previous section: interaction between additives and temperature to influence the Ca/Si of C-S-H. In the event of either one of the above deductions being correct, the full factorial approach fares better than Taguchi experimental design [50].

2.3.3 Comparison with molecular simulations

We noted that G37FH and G40FL produced C-S-H phase with identical Ca/Si ratios. Another notable result involving G37FH and G40FL is that in spite of the same Ca/Si of C-S-H in these pastes, we calculate different values (statistically significant) for the stiffness m_s of the C-S-H nanoparticle. Of the 24 samples, micromechanics-based modelling satisfied the criteria for the existence of the C-S-H nanoparticle with unique stiffness m_s^0 and hardness h_s^0 in in 8 samples (including G37FH and G40FL). We turn to results from molecular simulations to understand how the C-S-H nanoparticle can have different stiffness values for a

given Ca/Si. Figure 2.4 directly compares our computational predictions and experimental measurements of m_s and h_s over a range of Ca/Si ratios, and relates several key points. First, our experimental measurements of indentation moduli and hardness agree well with our predictions from molecular simulations over the Ca/Si range 1.3 - 1.8. Second, we find in our experiments that C-S-H of a fixed composition can exhibit a range of stiffness and hardness. This is consistent with predictions of simulations by Shahsavari et al., in which we observe that C-S-H structures of a given Ca/Si value do not exhibit the same stiffness and hardness. These structures can be referred to as C-S-H polymorphs, which we define as structures of identical composition (identical Ca/Si) but different physical or mechanical properties. The concept of polymorphs addresses the debate about whether Ca/Si increases or decreases stiffness of the C-S-H phase [62,63]. That is, the final Ca/Si does not uniquely determine the magnitude of mechanical properties of the C-S-H nanoparticle. Third, there exists an optimum Ca/Si which produces the stiffest and hardest C-S-H gel. Our simulations predict this optimum Ca/Si to be 1.5. This agrees well with our experimental predictions. In Sample A'40NO with the C-S-H phase of Ca/Si of 1.62 $\pm$ 0.1, our experiments predict the highest stiffness m_s and hardness h_s for the C-S-H nanoparticle.

How do polymorphic structures of C-S-H exhibit different properties for the same composition? Our team's simulations suggest that variation of structural parameters like mean chain length, dimer content and density are responsible for widely differing mechanical properties of polymorphs. Density of C-S-H nanoparticle has a linear correlation with its indentation modulus m_s (see Figure 2.5A). From the molecular model proposed by Pellenq et al [31], we know that the structure of C-S-H consists of silicate chains of various lengths. NMR studies on cement pastes have reported distinct chain lengths of 2, 5, 8 ... (3n-1) Si

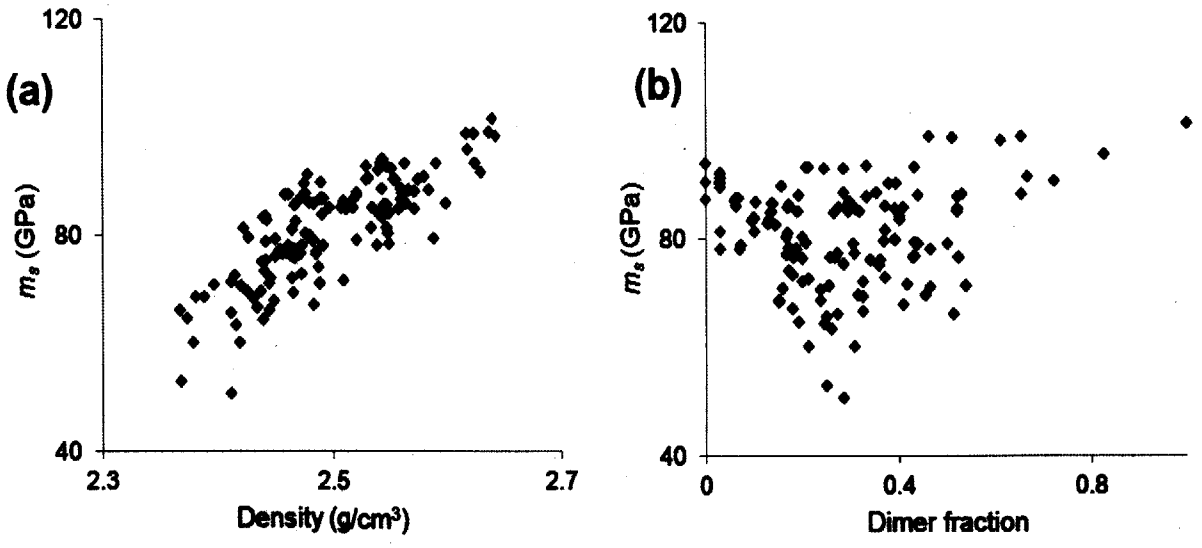

Figure 2.5: Molecular simulation predict dependence of Indentation Modulus m_s of the C-S-H nanoparticle on (A) density (B) fraction of dimeric silicate groups. The Ca/Si ratios of polymorphs shown here vary from 1.2 to 2.1. C-S-H density and dimer fraction were calculaed by M. Qomi for mechanical properties of the C-S-H phase calculated by R. Shahsavari.

Sample	Q_1 *(ppm)*	Q_2 *(ppm)*	l_{Si}	V_1 *- Proportion of Dimers (%)*
A'40NO	-78.3	-83.8	2.33	86
B'40NO	-78.8	-84.2	3.98	50

Table 2.6: Results of ^{1}H-^{29}Si CP MAS NMR experiments on A'40NO and B'40NO. Mean silicate chain length $l_{Si} = 2 \times (1 + V_2/V_1)$ where V_1 and V_2 are the proportions of Q_1 and Q_2, respectively.

atoms [22]. Interestingly, in our simulations we find a dependence of m_s on the fraction of dimeric silicate chains (Figure 2.5A). The higher the fraction of dimeric silicate chains, the higher the average m_s of polymorphs. However, there is no straightforward correlation like in the case of density. Note that polymorphs with $m_s \sim 100$ GPa exist over a range of dimer fractions from 0.5 to 1 (Figure 2.5B). Dimer fraction and silicate chain length can be experimentally determined using nuclear magnetic resonance (NMR) experiments.

We carried out CP MAS NMR experiments on A'40NO and B'40NO, for which we predict the C-S-H nanoparticle to have stiffness $m_s \sim 100$ GPa in both cases. We note dimers consist of two Q_1 groups. From equation (2.2), we also note that if the proportion of dimers is high, i.e., $V_1 \gg V_2$, the mean chain length is ~ 2. Our NMR results are summarized in Table 2.4. A'40NO has a high proportion of dimers and a chain length close to 2. On the other hand, B'40NO has a chain length of 4 and significantly lesser proportion of dimers. Thus, our experiments do not support the prediction from molecular simulations that the stiffest C-S-H polymorphs have a large proportion of silicate dimers.

As a cement paste ages, the average chain length of silicate chains increases. Typically, in the first year of cement paste hydration, the mean silicate chain length of C-S-H phase is less than 3 [23] (see Chapter 1). It is therefore surprising that silicate chain length in B'40NO is 4, after merely a month of hydration. In the past, NMR based studies have shown that the early stages of hydration (within 1 day) are dominated by Q_1 groups [23]. After ~ 1 week, the Q_2 groups can be observed in NMR [23, 57]. Thus, initially, the mean silicate chain length is 2. Subsequently, as silicate chains in C-S-H become longer and more ordered, the proportion of dimers or Q_1 groups decreases. This ties well to our NMR results for A'40NO. Belite, the major component of B' has a slower time frame of hydration than alite which is the major component of A'. If belite in B' has not reacted than, the NMR results of A'40NO and B'40NO should be similar in principle because alite is the only component reacting with water in both cases. If belite has started to react, after 28 days of hydration, its degree of hydration would be lesser than alite, and hence it should contribute relatively higher proportion of dimers than alite. In that case, the dimer content in B'40NO should be higher than A'40NO. Unfortunately, we cannot ascertain the relative amounts of C_2S and C_3S from EPMA-WDS as we observe a broad clinker cluster corresponding to a mixture of C_2S and C_3S. However, note that A' and B' have different composition from OPC and WPC (see Materials and Methods). The NMR results of B'40NO are surprising and at present, the only explanation we have is that relative alite/belite content could have significant effects on NMR results and thus, on the C-S-H silicate structure.

In the beginning of the chapter, we noted that optimizing the stiffness and hardness of

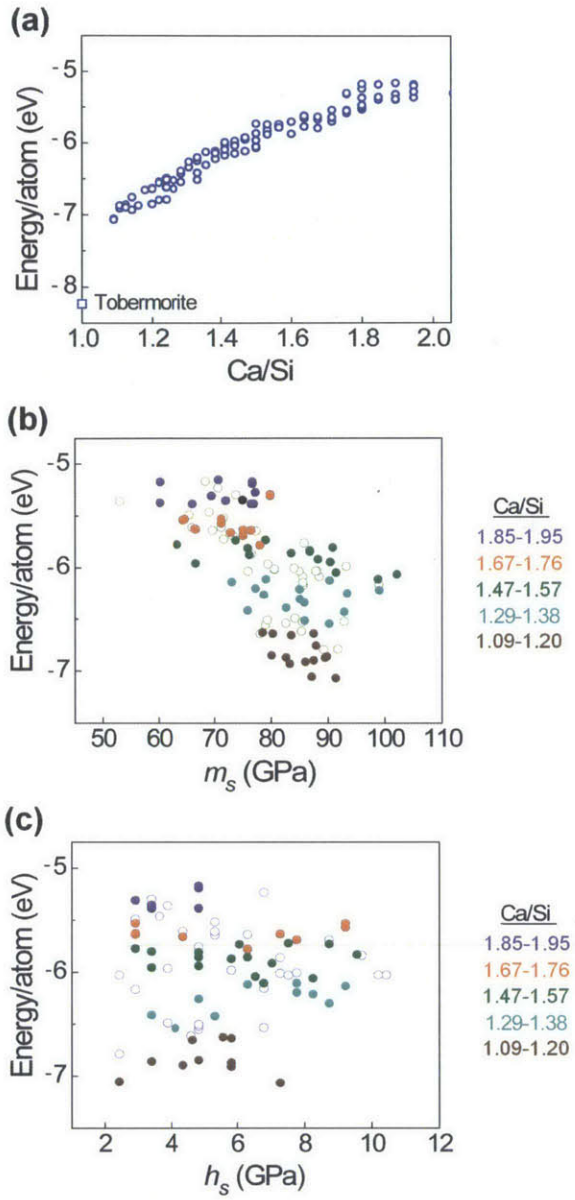

Figure 2.6: Energy of the C-S-H polymorphs from molecular simulations by R. Shahsavari on structures generated by R. Pellenq. (A) Energy per atom of C-S-H decreases with decreasing Ca/Si, tending to that of tobermorite for Ca/Si = 1.0. (B) Energy per atom generally decreases with increasing indentation modulus m_s. However, the stiffest polymorphs are of intermediate energies. (C) There exists no correlation between energy per atom and the hardness of the C-S-H polymorph. For a given Ca/Si range, these polymorphs confer a wide range of m_s and h_s for a narrow difference in energy. Colored filled circles represent polymorphs related to a specific Ca/Si range; open circles represent polymorphs outside of these defined Ca/Si ranges.

C-S-H is only part of the solution. The remainder being proposing protocols to repeatably produce C-S-H with those optimum properties. We explore the relative stabilities of various polymorphs using formation energy/atom obtained from molecular simulations. Note that normalization of formation energies on per-atom basis allows comparison among phases, without conflating the composition-dependent densities among these polymorphs. Figure 2.6A shows that the formation energy/atom of C-S-H correlates strongly with Ca/Si, due chiefly to the concurrent change in number of water molecules. Interestingly, the C-S-H phase stability generally increases with decreasing Ca/Si; as expected, the crystalline tobermorite phase at Ca/Si = 1 is most stable. Figures 2.6B-C relates the formation energy/atom to the elastic moduli and hardness of the C-S-H phase. Note that the C-S-H phases with lower m_s are of higher energy, whereas there is no correlation between stability and hardness h_s. Further, Figs. 2.6B-C shows that for a polymorph family of fixed composition (e.g., Ca/Si $\sim$ 1.5), there is no correlation between phase energy and these mechanical properties: these structures are energetically competitive (within $\sim$ 0.3 eV/atom). Thus, promotion of stiffer and harder polymorphs cannot be attained only by chemistry and relative phase stability, but may be accessible via altered reaction kinetics. Given the complexity of C-S-H precipitation in actual cement pastes that contain impurities unaccounted for in our current simulations, the level of agreement between experiments and simulations summarized in Figure 2.4 validates several of our computational predictions.

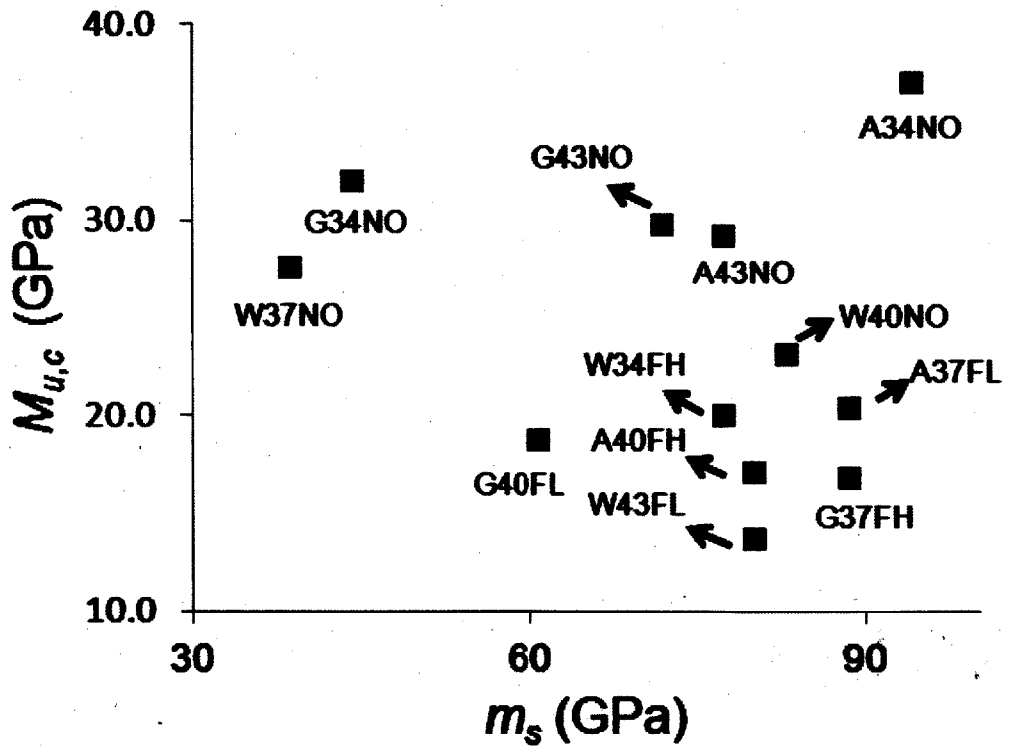

Figure 2.7: Influence of stiffness m_s of the C-S-H nanoparticle on the microscale composite stiffness $M_{\mu,c}$ of cement paste for 12 samples of L16 array.

2.3.4 Influence of C-S-H nano-scale properties on micro-scale composite properties of cement paste

Does high stiffness m_s and hardness h_s of the C-S-H nanoparticle ensure correspondingly better mechanical properties at a higher length scale? We explore this using our results from microindentation experiments on cement paste samples in L16 array. These experiments measure the composite stiffness of cement paste at the micron scale. Figure 2.7 shows the dependence of microscale composite stiffness of cement paste $M_{\mu,c}$ on stiffness m_s of the C-S-H nanoparticle. The microscale composite stiffness, $M_{\mu,c}$, is a function of the properties of several phases in cement paste (including C-S-H) and porosity. Of the 12 samples represented in Figure 2.7, micromechanics-based modelling to predict the stiffness m_s and hardness h_s of the C-S-H nanoparticle was successful (see Section 2.2) in 5 samples. We quantified the correlation between m_s and $M_{\mu,c}$ in these 5 samples using Pearson product-moment correlation coefficient r. The values of m_s and $M_{\mu,c}$ in these 5 samples are shown in Table 2.7.

Sample	m_s (GPa)	$M_{\mu,c}$ (GPa)
A43NO	77.3	29.2
A34NO	94.0	34.2
G37FH	88.4	16.8
G40FL	60.7	18.8
W34FH	77.3	20.0

Table 2.7: Stiffness m_s of the C-S-H nanoparticle and microscale composite stiffness $M_{\mu,c}$ of the cement paste in 5 samples of the L16 array in which micromechanical modelling to predict mechanical properties of the C-S-H nanoparticle was successful. This dataset was used to determine the correlation between m_s and $M_{\mu,c}$ as quantified by Pearson's product-moment coefficient r.

For the dataset shown in Table 2.7, r can be calculated as

$$r = \frac{1}{4}\sum_{i=1}^{5}\left(\frac{m_s - < m_s >}{\sigma_{m_s}}\right)\left(\frac{M_{\mu,c} - < M_{\mu,c} >}{\sigma_{M_{\mu,c}}}\right) \tag{2.6}$$

where $< X >$ and σ_X represent, respectively, the mean and standard deviation of X, $X \in \{m_s, M_{\mu,c}\}$. Using equation 2.6, we calculate r to be 0.5. This could be characterized as medium positive correlation. [11]

A notable result from Figure 2.7 is that in all cement pastes with fly ash (A40FH, W43FL, G37FH, G40FL, W43FH, and G40FL), we measure $M_{\mu,c}$ to be between 10 - 20 GPa, significantly lesser than that measured in samples without fly ash (W37NO, G34NO, G43NO, A43NO and A34NO). This has been repeatably observed in macroscale compression tests on cement pastes and concrete [64, 65]. Use of fly ash in cementitious materials has been shown to decrease compression strength of concrete for upto $\sim$ 3 months. We note that in 4/6 samples without fly ash (W37N0, G34NO, G43NO, and A43NO), $M_{\mu,c}$ is around 30 GPa, irrespective of the stiffness m_s of the C-S-H nanoparticle (Figure 2.7). However,

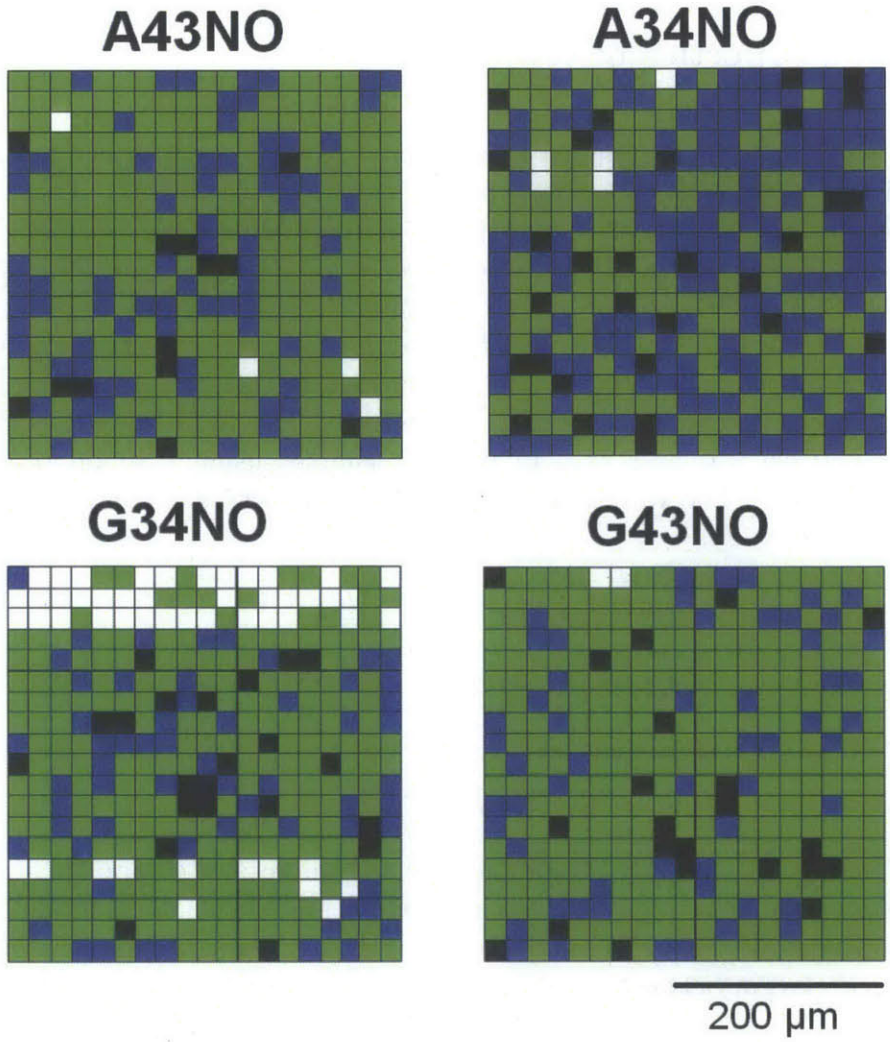

Figure 2.8: Voxel maps of indentation modulus measured by nanoindentation of 400×400 μm^2 area on cement paste specimens. Each voxel represents a mean volume of 60 μm^3 (20 ×20 μm^2 surface area with an average indentation depth of 150 nm). Color code: White - $M \in [0-15]$ GPa, capillary pore ; Green - $M \in [15-35]$ GPa, C-S-H; Blue - $M \in [35-50]$ GPa, C-S-H + Portlandite; Black - $M > 60$ GPa, Portlandite + Clinker, where M is the indentation modulus measured by nanoindentation. Ranges of M for different phases from Ref. [34].

A34NO is an exception. In A34NO, with the highest value of stiffness m_s of the C-S-H nanoparticle among samples represented in Figure 2.7, we measure the highest microscopic composite stiffness to be 37 GPa. To verify if high $M_{\mu,c}$ of A34NO stems from C-S-H phase, we turn to voxel maps generated from nanoindentation data.

The nanoindentation maps of A43NO, G34NO and G43NO are comparable (Figure 2.8). This explains the similar values for $M_{\mu,c}$ measured in these samples ($\sim$ 30 GPa). Porosity in G34NO does not influence $M_{\mu,c}$ significantly. In fact, $M_{\mu,c}$ of G34NO is slightly higher

Sample	M of C-S-H (GPa)	η (%)
A43NO	24.9 ± 5.6	72
A34NO	34.2 ± 5.1	74
G34NO	26.7 ± 5.3	73
G43NO	27.1 ± 6.1	71

Table 2.8: From mixture modelling of nanoindentation data, we can extract average microscale stiffness of C-S-H phase as the mean ± standard deviation of M among data points belonging to the C-S-H cluster.

than that of G34NO and A43NO, although the latter two samples contain lesser porosity. More importantly, there is little porosity (white voxels in Figure 2.8) in A43NO and A34NO. This is important because micromechanics-based extrapolation to determine the properties m_s and h_s of the C-S-H nanoparticle was successful in both A43NO and A34NO (Table 2.3). In Figure 2.8, note the relatively higher proportion of blue voxels in A34NO compared to the other 3 samples in general and A43NO in particular. In the absence of porosity, this difference must be responsible for the variation in $M_{\mu,c}$ among these samples. Blue voxels in Figure 2.8 could represent either C-S-H or CH or a mixture of both. From our mixture modelling algorithms, we can extract the average stiffness M of C-S-H phase as measured by nanoindentation and its packing density (Table 2.8). We note that the average stiffness of C-S-H phase in A34NO is significantly higher than in in other samples in general and A43NO in particular. We also note from Table 2.8 that the packing density η is similar in all 4 samples. Thus, we measured the highest microscale composite indentation modulus $M_{\mu,c}$ in the sample with the stiffest C-S-H nanoparticle.

2.4 Summary

We prepared 24 cement pastes of varying Ca/Si of the C-S-H phase by exploring several factors such as cement clinker chemistry, alite content, w/c, additives and curing temperature. We measured a maximum Ca/Si of 1.88 and a minimum Ca/Si of 1.29 for the C-S-H phase. Our results were consistent with the previous work involving measurement of Ca/Si of the C-S-H phase in cementitious systems.

Our Taguchi design of experiments could not identify the optimal levels of synthesis factors to repeatably produce stiff and hard C-S-H phase. This could partly be a result of using hypothetical results for samples prepared with β-C_2S. However, we also found that interactions between synthesis factors could influence the outcome, and this is best accounted for using smaller full factorial designs. Notably, in samples G40FL and G37FH, we deduced that the interaction of curing temperature and additives produced a C-S-H phase with low Ca/Si ratio. Future work should consider other potential interactions between factors before designing experiments.

We find that mechanical properties of the C-S-H nanoparticle can indeed be tuned by altering its Ca/Si. In our experiments, we find that Ca/Si of C-S-H does not uniquely determine the stiffness m_s and hardness h_s of the C-S-H nanoparticle. Results from molecular

simulations on the C-S-H phase by our collaborators simulations suggest the existence of polymorphs: C-S-H nanoparticles of the same composition can exhibit different values of stiffness and hardness. Remarkably, our experiments affirm the prediction from molecular simulations that C-S-H polymorph with Ca/Si $\sim$ 1.5 exhibited the highest stiffness and hardness.

Molecular simulations on the C-S-H phase propose that the difference in mechanical properties of polymorphs arises out of structural differences, importantly phase density and proportion of silicate dimers. We test the prediction on silicate chain structure with CP NMR MAS experiments on our cement paste samples in which we experimentally found the highest stiffness m_s. Interestingly, one of the samples was rich in silicate dimers as predicted by molecular simulations while the other had significantly lower proportion of dimers. In other words, we do not provide conclusive evidence that high stiffness of C-S-H is correlated with a high proportion of silicate dimers.

We explored the relative stabilities of polymorphs by considering the energy associated with each structure as calculated from atomistic simulations. We find that polymorphs with lower Ca/Si are more stable than those with higher Ca/Si. For polymorphs of similar Ca/Si, we found that stiffer polymorphs of the C-S-H phase have similar formation energies as those with lower stiffness. This points to the importance of a thorough understanding of hydration kinetics to consistently produce the C-S-H phase with optimum stiffness and hardness.

Finally, we explored the relationship between stiffness m_s of the C-S-H nanoparticle and microscale composite stiffness $M_{\mu,c}$ of cement paste. Our data suggests a medium positive correlation between m_s and $M_{\mu,c}$. In samples with fly ash, we measured approximately 50% lesser $M_{\mu,c}$ than in samples without fly ash. We measured the highest $M_{\mu,c}$ in the sample with the stiffest C-S-H nanoparticle, i.e., sample with highest m_s. These results should be interpreted carefully as none of the samples we tested represents the complexity of an industrially produced concrete. In the next chapter, we explore whether results on the C-S-H phase can be applied to existing concrete formulations.

Chapter 3

Towards designing concrete for protective infrastructure

3.1 Introduction

Ultra high performance concrete (UHPC) is one of the hallmarks of 20^{th} century concrete innovations. In comparison to ordinary concrete, its properties such as higher compressive strength, lower creep resistance, and shrinkage have led to its adoption in diverse applications [66–68]. An important application for which UHPC's properties are currently being explored is its ability to withstand extreme environments such as explosions [69]. Research and development of UHPC specifically geared towards blast/explosion resistance has obvious applications in buildings and structures of national/international importance which need to be safeguarded against potential damages from mechanical impact and high temperatures.

In light of such long term objectives, our current work focuses on three topics: (1) properties of calcium silicate hydrate (C-S-H) phase in UHPC and how they compare to those found in ordinary cement paste (OPC), (2) influence of reinforcement fibres on the micro-nanoscale properties of UHPC, and (3) effects of prolonged exposure to high temperatures on C-S-H and UHPC matrix. We carry out our investigations on a commercially available UHPC, Ductal®. To study the effect of elevated temperature on C-S-H and microstructure, our collaborators at Oak Ridge National Lab, F. Ren et al., heat treated some samples to temperatures of 500 and 1000°C. Subsequently, we investigated the mechanical properties and chemical composition of these samples using nanoindentation and EPMA-WDS experiments, respectively.

3.2 Materials & Methods

UHPC is superior to Ordinary Portland Cement-based concrete in terms of two performance characteristics that have long plagued the latter's structural applications: mechanical fracture resistance and susceptibility to environmental attacks. This is why conventional concrete needs to be reinforced with steel bars. Multi-scale porosity in conventional concrete is primarily responsible for these problems. UHPC overcomes these weaknesses through (a)

efficient packing of constituent particles, and (b) low water/cement ratio. Concrete is a porous granular material [31], comprising cement clinker and hydrates, sand (quartz) and stone aggregates [24]. In UHPC, stone aggregates are not used; quartz is the only aggregate. Further, efficiency of space occupancy is improved by broadening the particle size distribution so that small particles fill the space between large particles. When excessive unreacted water in concrete evaporates during setting, it leaves behind porous space. On the other hand, water is essential to form cement hydrates that provide cohesion. In UHPC, an optimum water/cement ratio of 0.15 [66] is used; this is approximately half of that used in traditional concrete. The superior mechanical performance of UHPC, compression strength 20 times greater than ordinary concrete and flexural strength comparable to aluminum [66], is attributed to porosity reduction. UHPC can be reinforced with steel fibers instead of steel bars to improve ductility, in terms of strain-to-failure [68]. The high-tensile steel fibers used in Ductal® are typically 14 mm long with a diameter of 0.2 mm [70]. The other notable difference in UHPC over ordinary concrete is the use of silica fume [66]. Silica fume is known to react with $Ca(OH)_2$ to form the C-S-H phase of low Ca/Si by the so-called pozzalonic reaction [6,21]. We note that the diameter of silica fume particles used in UHPC is typically of the order of 0.1 μm [67,71]. Therefore, this phase can only be perceived in conjunction with other phases in our nanoindentation or EPMA-WDS experiments, whose interaction volumes are of the order of 1 μm^3.

Commercially available UHPC Ductal® was used to prepare specimens for experiments. Samples were cast at Oak Ridge National Laboratory as cylinders of diameter 2″ and height 4.5″. We use two different types of samples: (a) sample nos. 106, 109, 114, 102C and 105B with steel fibre reinforcements in the matrix, henceforth referred to as the 100 series and (b) samples nos. 411, 414, 420, 406A and 419C with no matrix reinforcements, henceforth referred to as the 400-series. Among the five samples belonging to each series, the first three listed above were tested in as-prepared condition (henceforth referred to as pristine) and the last two were subjected to high temperatures. Specimens of approximately 0.4×0.4×0.1″ were then cut from these samples at MIT using diamond saw with ethanol as a coolant. The polishing procedure used to prepare specimens for nanoindentation and x-ray spectroscopy experiments has been described in Ref. [39].

Two samples belonging to each series were then subjected to high temperatures by irradiating with a plasma lamp (see Figure 3.1). These heat treatments were carried out by F. Ren et al. at Oak Ridge National Laboratory. Thermocouples inserted at different heights along the cylindrical sample were used to monitor the temperature of the sample. By varying the plasma lamp's power and the duration of exposure to plasma lamp, we were able to achieve different heat treatments in samples. Samples 105B and 419C were both heated to maximum temperatures close to 1000°C and sustained heavy macroscopic damage. Notably, sample 419C (without steel fibers) disintegrated into smaller irregular pieces while sample 105B (with steel fibers) was able to partially retain its structural integrity. Samples 406A and 102C were heated to maximum temperatures of 400°C. For all heat treated samples except 419C, specimens for experiments were cut from the top surface of the samples which achieved the maximum temperatures.

We used statistical nanoindentation to assess the microscale mechanical properties of constituent phases in UHPC. The protocol for these experiments and subsequent analyses has been described in Section 2.2. We used the identical grid configuration and loading

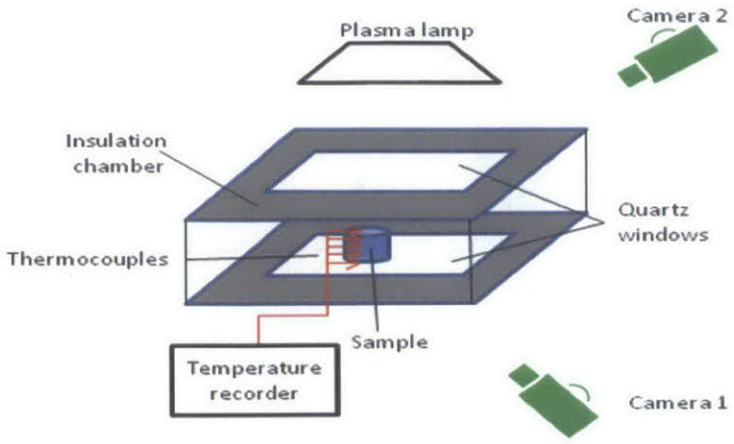

Figure 3.1: Schematic of experimental setup used for heat treatment of UHPC samples. From F. Ren et al., Oak Ridge National Laboratory.

conditions to those described in the previous chapter. Additionally, from the data set of extracted values of indentation modulus M and indentation hardness H of each specimen, we construct voxel maps showing the spatial variation of these properties across the sampled area of each specimen. In other words, this is the microstructure of the specimen perceived by the nanoindenter. To generate these maps, we do not eliminate irregular load-response curves corresponding to pores and surface preparation defects as that data filtering operation would render the spatial component of these maps meaningless. We refer to this complete data set as unfiltered data set. For the chemical analysis of constituent phases in UHPC, we used EPMA-WDS in an identical fashion to that described in Section 2.2.

3.3 Results & Discussion

3.3.1 Comparision of C-S-H in UHPC & OPC

We compared the composition and fundamental mechanical properties of C-S-H in UHPC with those found in OPC (sample G40NO, see Chapter 2). These results are summarized in Figure 3.2. First, C-S-H in UHPC has a Ca/Si ratio $\sim$ 1, distinctly different from that found in OPC ($\sim$1.7). UHPC is rich in silica fume and it is likely that the low Ca/Si ratio is a result of pozzalonic reaction with silica fume [22]. Note that the measured difference in Ca/Si between 400-series (without fibers) and 100-series(with steel fibers) is within the limits of experimental uncertainty. Hence, we can deduce that steel fibers do not influence the Ca/Si of C-S-H. Second, we experimentally calculate the stiffness m_s of the C-S-H nanoparticle in 100-series and 400-series to be close to 90 GPa in comparison to 72 GPa in OPC. Taking into account uncertainties in both the above values, we infer that the C-S-H nanoparticle is 8-45% stiffer in UHPC than in OPC. We calculate the hardness of the C-S-H nanoparticle to be 8.5 and 4.75 GPa, respectively in UHPC and OPC. This represents a 27-167% increase in hardness h_s of the C-S-H nanoparticle in UHPC over that in OPC.

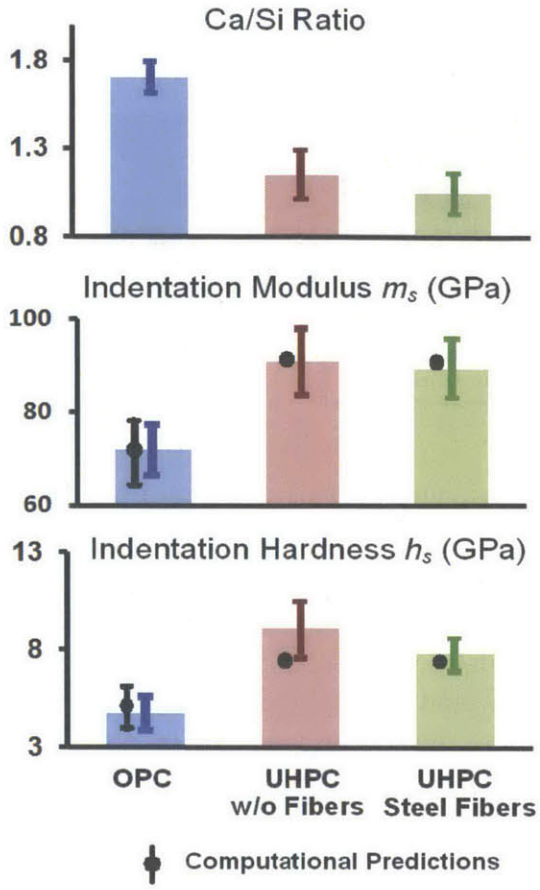

Figure 3.2: Comparison of composition and nanoscale mechanical properties of C-S-H in UHPC with those found in OPC. Error bars of experimental data (colored bars) correspond to uncertainties in predictions from micromechanics model. The half length of the error bar of indentation modulus m_s of the C-S-H nanoparticle (and similarly for indentation hardness h_s) is given by $< R^0_{m_s} > \times c_v$. These terms are defined in Section 2.2. Computational predictions from R. Shahsavari et al. [72]. For Ca/Si = 1.7, the length of the error bar in computational predictions (black) represents the range of properties of different polymorphs (Figure 2.4). At Ca/Si = 1, only one polymorph exists (Tobermorite, Figure 2.6A), and consequently that prediction does not have an error bar.

These changes in the mechanical properties of the C-S-H phase support our earlier findings in Section 2.3.3. that the mechanical properties of C-S-H can be tuned its composition as quantified by Ca/Si. Thirdly, the results of our experiments agree with those from molecular simulations by R. Shahsavari et al. [72]. For C-S-H nanoparticle of Ca/Si = 1 and Ca/Si = 1.7, the theoretically predicted stiffness m_s and hardness h_s values are within the respective range of values calculated from experiments. Thus, we have demonstrated the merits of this combination of theoretical and experimental understanding of C-S-H through its application on a commercially available concrete.

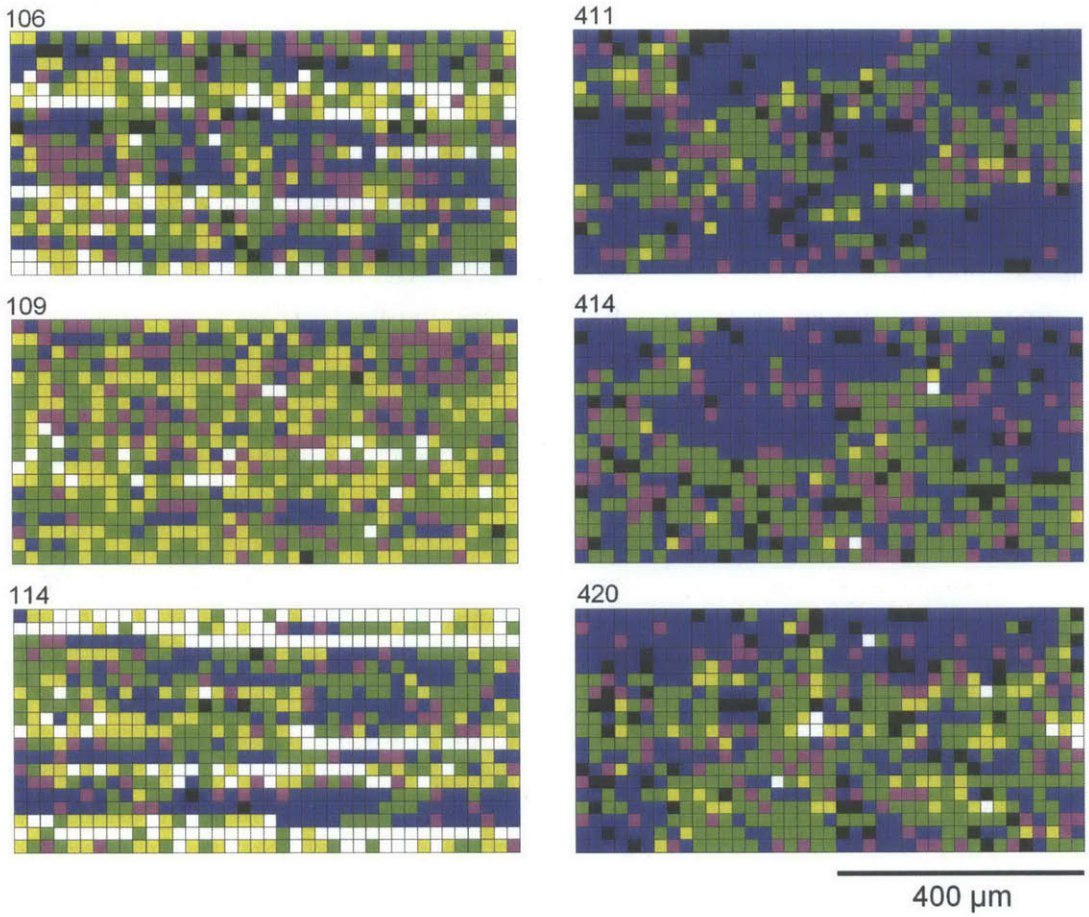

Figure 3.3: Voxel maps of indentation modulus measured by nanoindentation of 800×400 μm^2 area on pristine UHPC specimens. Each voxel represents a mean volume of 60 μm^3 (20 ×20 μm^2 surface area with an average indentation depth of 150 nm). Colors of voxels correspond to following range of indentation modulus magnitude : White - 0 - 15 GPa, capillary pore (∼10μm) ; Yellow - 15 - 30 GPa, low density (LD) C-S-H, sub-micron capillary pore (∼0.1μm); Green - 30 - 50 GPa, high density (HD) C-S-H; Magenta - 50 - 60 GPa, C-S-H+α-quartz; Blue - 60 - 90 GPa, α-quartz+ clinker; Black - > 90 GPa; clinker+steel wires. The choice of range of magnitudes for different phases is described in Figure 3.4.

3.3.2 Effect of steel fibers on UHPC matrix

We find that in the microstructures perceived by the nanoindenter (see Figure 3.3), there are some noticeable differences between the 100-series and the 400-series of specimens. We observe:(1) the presence of porosity (white voxels in Figure 3.3) in 100-series (immediately apparent bottom-most 100-series voxel map in Figure 3.3) and its relative absence in 400-series (2) relatively higher presence of low density (LD) or low stiffness C-S-H (yellow voxels in Figure 3.3) in 100-series more than the 400-series and (3) the presence of large areas of blue voxels, representing α-quartz (stable polymorph of quartz up to 573°C) + clinker phase

mixture, in 400-series and their absence in 100-series. Below we explore each one of the above deductions in more detail.

We cannot infer that incorporation of steel fibers in UHPC matrix leads to the formation of large pores of diameter $\sim$ 100 μm as they are absent in the voxel map of Sample 109 (Figure 3.3). It is important to note that voxel maps in Figure 3.3 involve all the measured nanoindentation load-response curves, including the irregular load-response curves corresponding to pores and surface-preparation defects, i.e., they use unfiltered nanoindentation data (see Section 3.2).

Upon inspecting the load-response curves corresponding to LD C-S-H observed prominently in the 100-series in (yellow areas in Figure 3.3), we find that, in the majority of cases, these correspond to capillary pores (pores with diameter in the range 10 nm - 10 μm [73]) with maximum depth measured by nanoindentation of 0.3 μm. In instances where yellow voxels in Figure 3.3 are immediately adjacent to white voxels, the yellow voxels are sub-micron capillary pores which are part of larger pores ($\sim$10 μm) and act as an interface between the solid phase and the large pore. We also observe independent sub-micron capillary porosity, especially in Sample 109, which has relatively fewer large pores of diameter $\sim$ 10 μm (white voxels in Figure 3.3) than other specimens in the 100-series. These results are better visualized using probability distributions of indentation modulus both in filtered and unfiltered data sets.

Figures 3.4A and 3.4B compare the probability distribution of the unfiltered indentation modulus dataset of the 100-series of specimens with those of the 400-series of specimens. As observed in Figure 3.3, there are noticeable differences in volume fractions of porosity ($<$ 15GPa), stiffness of the C-S-H phase (15-50 GPa) and stiffness of α-quartz + clinker phase mixture and these volume fractions respectively correspond to the three deductions in that order from Figure 3.3. Having discussed the presence of large pores earlier, we continue with the discussion of low density or low stiffness C-S-H phase and its relatively higher volume fraction in the 100-series. We are tempted from Figures 3.4A and 3.4B to conclude that incorporation of steel fibers in UHPC matrix leads to distinct reduction in the stiffness of the C-S-H phase. However, as mentioned in the previous paragraph, we observe that a number of data points in the LD C-S-H range of indentation modulus ($15 < M < 30$) actually correspond to sub-micron capillary pores. Upon elimination of data points associated with irregular load-response curves corresponding to pores and surface preparation points, we observe that the probability density peak associated with the C-S-H phase in 100-series moves to higher indentation modulus values and now matches well with that seen in the 400-series (Figures 3.4C and 3.4D) in two out of three instances (106 and 114). Thus, we infer that incorporation of steel fibers in UHPC matrix does not necessarily lead to the formation of C-S-H with low stiffness.

From Figures 3.4B and 3.4D, we observe that, among the specimens of the 400-series, the positions of probability density peaks associated with C-S-H phase and quartz + clinker are remarkably identical, i.e., the peaks are located at the same indentation modulus value for all specimens. This is unlike the 100-series in which the probability density peaks associated with the C-S-H phase occurred at different values of indentation modulus for different specimens. This suggests that the mechanical properties of the C-S-H phase do not vary among the three 400-series samples. On the other hand, the mechanical properties of the C-S-H phase exhibit significant variation among the 100-series of samples. This variation in

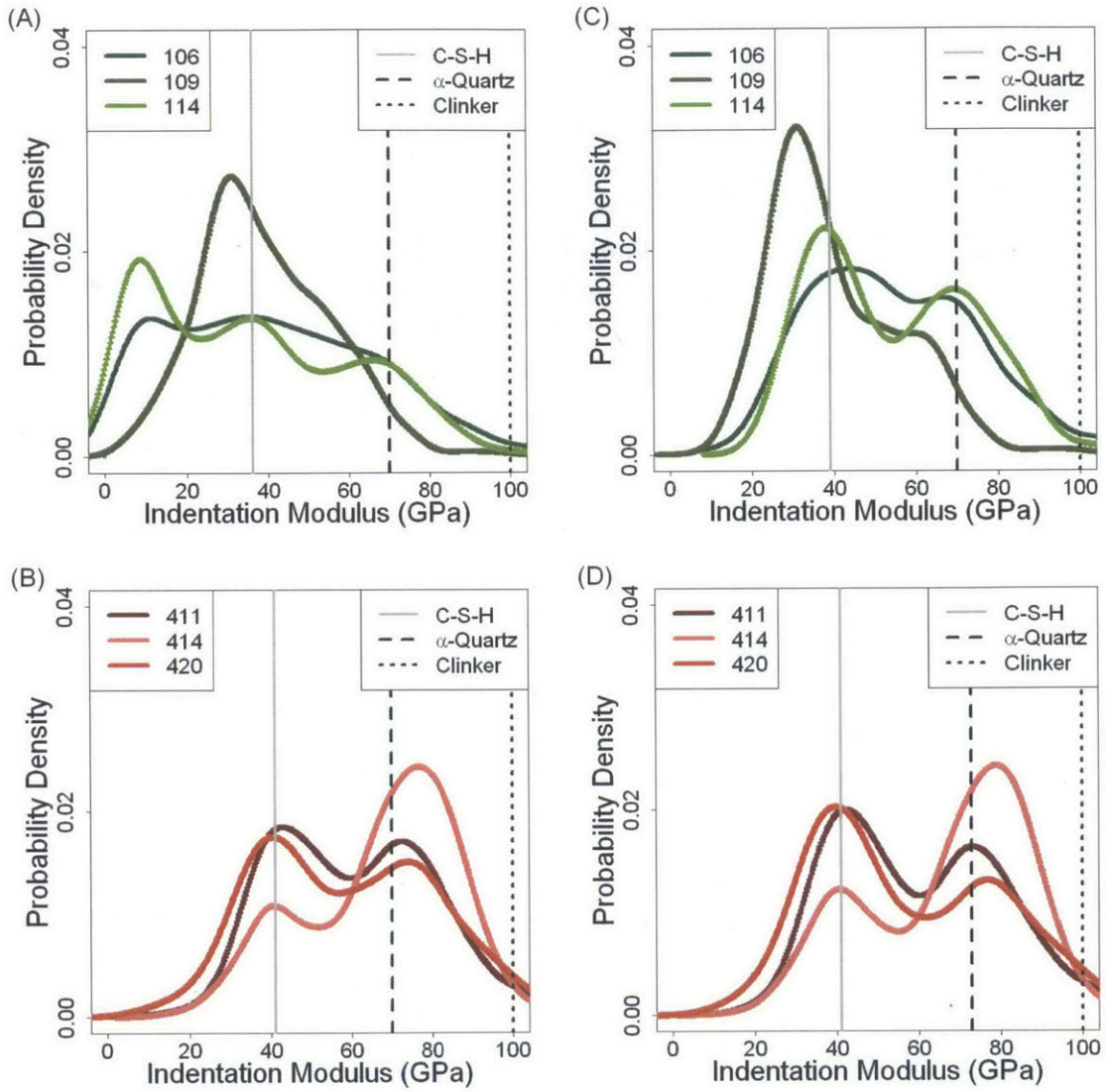

Figure 3.4: Probability distribution of unfiltered indentation modulus data set of (A) the 100-series and (B) the 400-series, and filtered indentation modulus data set of (C) the 100-series and (D) the 400-series. α-quartz and clinker phases (black dotted vertical lines) have been identified through standard properties reported elsewhere. The probability density peaks in $60 < M < 100$ GPa region must correspond to quartz sand/flour which we label as $\alpha - Quartz$. This peak occurs around 75 GPa with a half width at full maximum of approximately 15 GPa. Further, note that there is a crest in the probability distributions in 50 - 60 GPa region which must represent a mixture of the phases represented by probability density peaks on either side of the crest. Vertical lines labelled C-S-H are mere visual aids to help identify probability distribution peaks corresponding to the C-S-H phase. This peak occurs around 40 GPa with a full width at half maximum of approximately 10 GPa.

microscale properties of the C-S-H phase is attributable possibly to steel fibers since that is the only component that distinguishes the 100-series from the 400-series. The question that then arises is whether the steel fibers locally influence the packing density η of the C-S-H phase or the fundamental nanoscale mechanical properties m_s and h_s of the C-S-H nanoparticle? From Figure 3.2, we can infer that the fundamental nanoscale properties, namely Ca/Si ratio, m_s and h_s are unaffected by the incorporation of steel fibers. Hence, steel fibers must locally reduce the packing density of the C-S-H phase.

Our third deduction from Figures 3.3 and 3.4 is concerned with (a) presence of large grains of blue voxels corresponding to α-quartz + clinker in 400-series and their absence in 100-series in Figure 3.4, and (b) probability density peaks of α-quartz + clinker in Figure 3.4C and 3.4D occurring at 80 GPa in 400-series and 70 GPa in the 100-series, the latter matching closely with the experimentally determined indentation modulus of α-quartz. Previous nanoindentation studies on UHPC have attributed measurements with $M \in [60 - 90]$ GPa to α-quartz [67, and references therein]. Further, note that these grains of blue voxels are of length $\sim$ 100 μm. The only UHPC constituent with particle diameters of that order is sand, i.e., α-quartz [66]. This can be explained by considering the efficient packing of particles of different diameters in UHPC (without fibers). The characteristic particle size of different constituents of UHPC such as α-quartz, clinker, silica fume and so on are carefully engineered so as to maximize the packing density and particle-particle contact [66]. When steel fibers with a completely different aspect ratio than the particles are incorporated in the matrix, the ideal spatial arrangement of particles breaks down. This explains why large grains of blue voxels are not found in the 100-series in Figure 3.3 and probability density peaks corresponding to α-quartz + clinker occur close to the indentation modulus of α-quartz in Figure 3.4B, suggesting that they are probably pure α-quartz particles. Note that unlike the local changes in properties of C-S-H, these observations are applicable to all the 100-series specimens and therefore, must occur globally over the entire sample.

3.3.3 Effect of exposure to elevated temperatures

To test the suitability of these materials for resistance to mechanical failure after exposure to high temperatures, such as those experienced in blasts, a subset of samples were heated to temperatures of 400°C and 1000°C. In the 100-series specimen from the sample exposed to 1000°C, the specimen became extremely porous (see Figure 3.5). As described in the Materials and Methods Section, the 400-series sample exposed to 1000°C disintegrated into irregular pieces and therefore we cannot ascertain the maximum temperature our tested specimen experienced. However, we label it as 1000°C. Unlike 105B, its voxel maps do not show signs of significant damage. Thus, we deduce it did not experience high temperatures close to 1000°C. It is interesting to note that the parts of the sample were relatively undamaged even after exposure to 1000°C.

Interestingly, we note that capillary porosity found in pristine 100 series specimens is absent from the 100-series specimen heated to 400°C. We also notice that it has large blue grains corresponding to α-quartz + clinker as seen in pristine 400-series specimens. Turning to the 400-series specimen heated to 400°C, we observe that it has a relatively large number of black voxels corresponding to unreacted clinker. To further understand these observations, we use probability distributions of indentation modulus and hardness as in Section

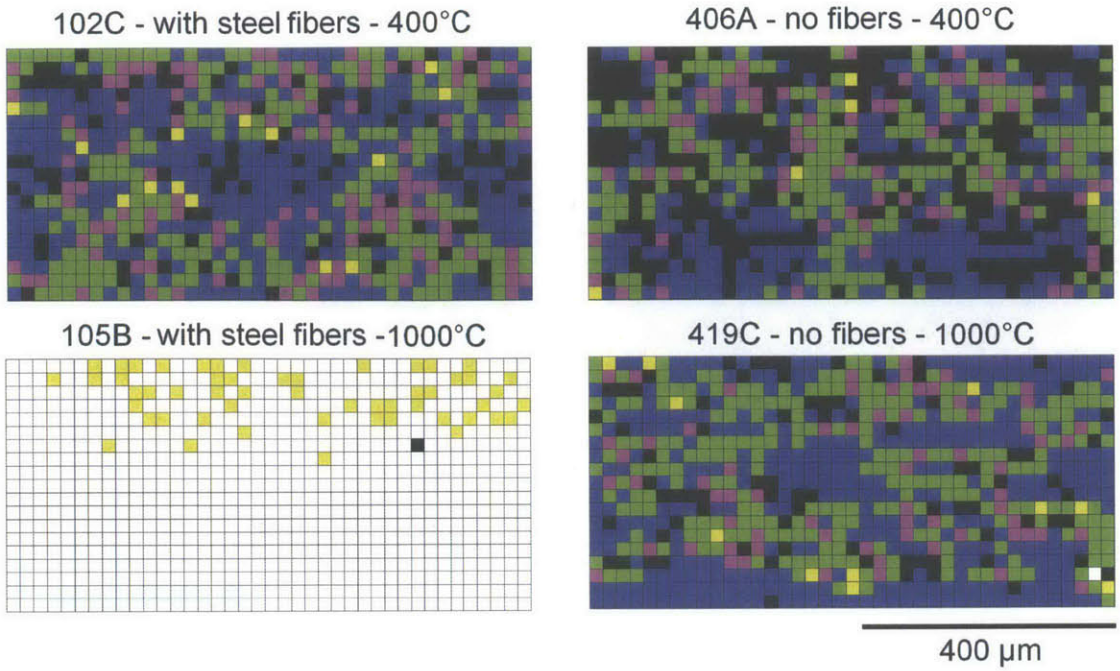

Figure 3.5: Voxel maps of indentation modulus measured by nanoindentation of 800×400 μm^2 area on heat treated UHPC specimens. Each voxel represents a 20 × 20 μm^2 area on a specimen. Color code: White - 0 - 15 GPa, capillary pore ($\sim$ 10 μm) ; Yellow - 15 - 30 GPa, low density (LD) C-S-H, sub-micron capillary pore ($\sim$ 0.1 μm); Green - 30 - 50 GPa, high density (HD) C-S-H; Magenta - 50 - 60 GPa, C-S-H+α-quartz;Blue - 60 -90 GPa, α-quartz+ clinker; Black - > 90 GPa; clinker+steel wires. Note that Sample 105B sustained heavy microscopic damage during heat treatment and here we see that it has been rendered porous.

3.3.2. Because of the relative absence of porosity in all heat treated samples except the 100-series sample heat treated to 1000°C, we use filtered nanoindentation data set to produce probability distributions of indentation modulus and hardness.

From Figure 3.7, we observe that the Ca/Si ratio of C-S-H remains unchanged from heat treatment to 400°C. Thus, we can ascertain that the C-S-H phase within the UHPC is heat resistant up to 400°C. We also observed that that the 100-series sample subjected to 1000°C majorly consists of silica phases. Figure 3.6A and B suggests that this sample is dominated by pores. Dehydration of C-S-H can lead to creation of pores. However, this phenomenon alone cannot explain all the porosity in 105B subjected to 1000°C because Figure 3.7A suggests that Si-rich phases are dominant in this sample. We know these Si-rich phases to be quartz sand/flour. The quartz phase does not undergo any chemical change during the thermal treatment as they do not react with silicates, silicate hydrates or carbonates of Calcium which constitute the rest of the UHPC matrix. Since this sample was not subjected to any mechanical stress, we can deduce that heat treatment to 1000°C has resulted in a porous form of quartz. Given this phase was not highly porous in pristine samples and its melting point is $\sim$ 1700°C [74], we can surmise that thermal stresses setup during the heat

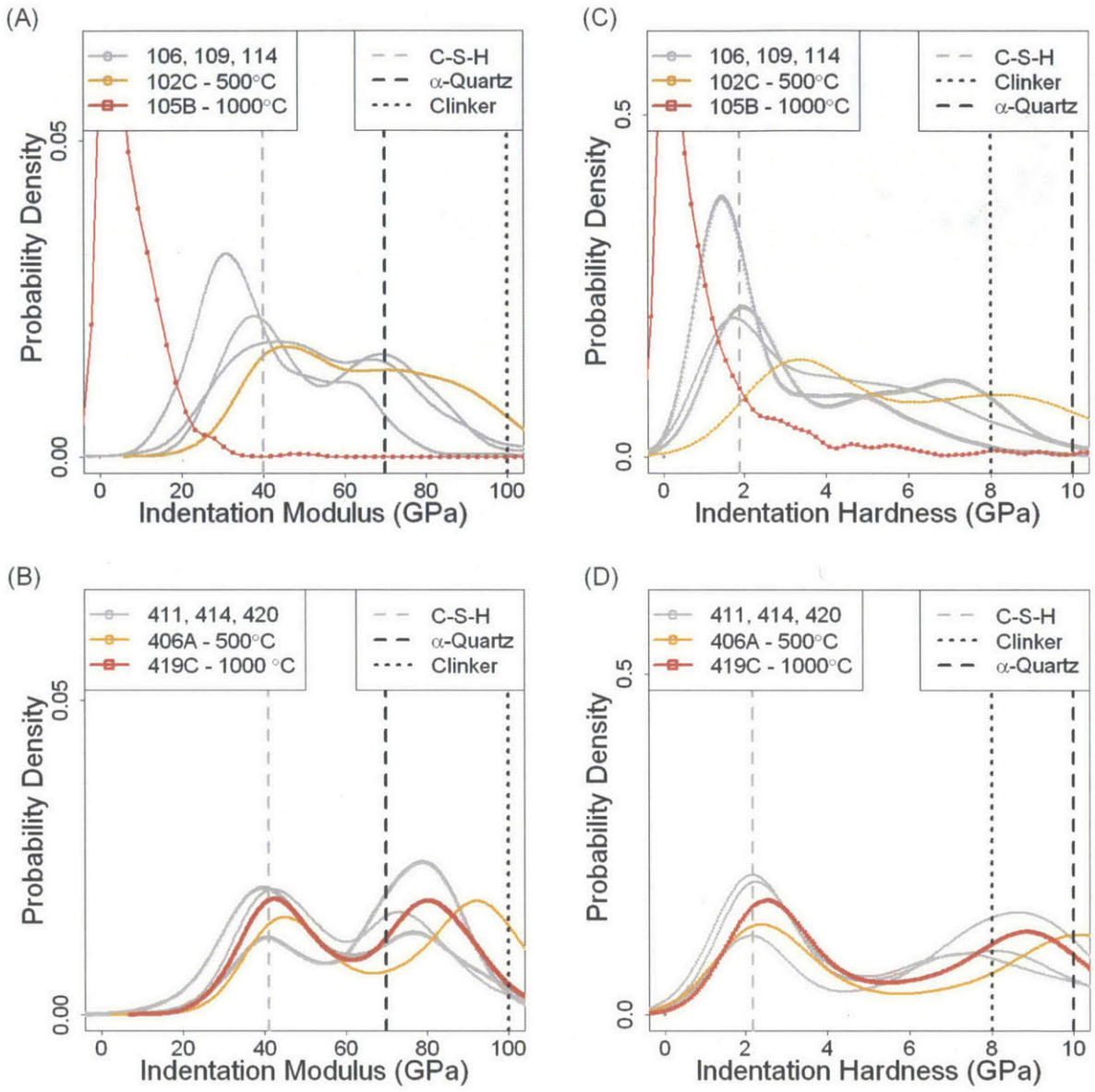

Figure 3.6: Effect of heat treatment on indentation modulus in (A) the 100-series and (B) the 400-series and indentation hardness in (C) the 100 series and (D) the 400-series. α-quartz and clinker phases (black dotted vertical lines) have been identified through standard properties reported elsewhere and represent the peaks in $M > 60$ GPa and $H > 4$ GPa regions. Vertical lines labelled C-S-H are mere visual aids to help identify probability distribution peaks associated with the C-S-H phase. Note that filtered nanoindentation data sets were used for this figure.

treatment have fractured the quartz phase.

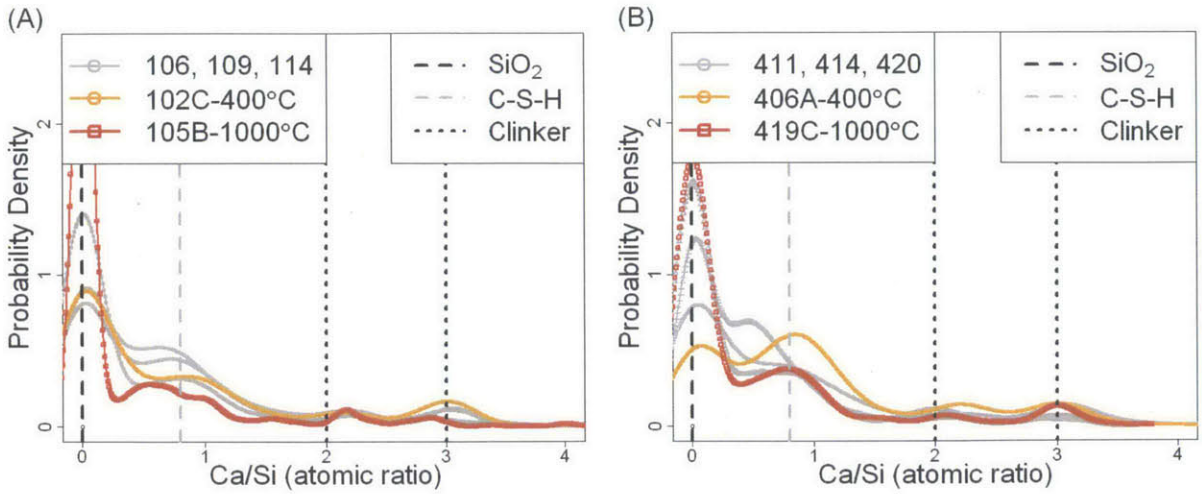

Figure 3.7: Probability distribution of Ca/Si ratio measured by X-ray spectroscopy in (A) the 100-series and (B) the 400-series. SiO_2 and clinker phases (black dotted vertical lines) have been identified by their standard compositions. Vertical lines labelled C-S-H are mere visual aids to help identify probability distribution peaks associated with the C-S-H phase.

3.4 Summary

We investigated the nanoscale properties of C-S-H in UHPC and found it to be distinctly different from C-S-H found in OPC. We noted the trend towards increasing thermodynamic stability of C-S-H as Ca/Si approaches 1 in Figure 2.6, with the most stable C-S-H phase being Tobermorite with Ca/Si = 1. We measured the Ca/Si of C-S-H in UHPC to approximately unity. Our nanoindentation experiments show that this C-S-H phase is significantly stiffer and harder than the C-S-H polymorphs with Ca/Si $\sim$ 1.7 that are typically of OPC. The mechanical properties we predict for C-S-H in UHPC agree well with the results from molecular simulations on Tobermorite.

From our microscale investigation of UHPC, we find incorporation of steel fibers: (1) creates sub-micron scale capillary porosity, (2) locally affects the packing density of C-S-H, and (3) leads to deterioration of excellent particle-particle contact which is a characteristic feature of UHPC. Although findings (1) and (3) seem initially pejorative, this porosity and reduced particle packing may be advantageous especially in the case of designing materials that can sustain high pressures and high temperatures. It is well known that upon impact by high velocity projectiles, unreinforced UHPC based structures fail largely due to build up of pore pressures from a combination of evaporation of water from hydrated phases and dimensional changes accompanying phase transformations of constituent materials [75]. The efficient packing of particles, which is a hallmark of UHPC [66], is more a bane than a boon in this instance because it allows rapid increase of pore pressures. Incorporation of steel fibers not only provides tensile strength, but also, unintended "breathing spaces" in the form of capillary porosity that can alleviate the pore pressure related concerns. Future research on these materials for blast resistance should consider these aspects of fiber reinforcements.

From investigation of heat treated UHPC specimens, we conclude that UHPC is heat resistant up to at least 400°C. Interestingly, we note capillary porosity observed in pristine 100-series specimens with steel fibers is absent after being heated to 400°C. It is likely that, there is a reorganization of particles to achieve more efficient packing, and thus the apparent lack of capillary porosity in 100-series specimen heat treated to 400°C. In the 100-series specimen heated to 1000°C, development of thermal stresses has led to the fracture of the quartz phase.

In the concluding section of Chapter 2 (Section 2.4), we remarked about the importance of understanding cement hydration kinetics, given that C-S-H polymorphs of high and low stiffness m_s had similar thermodynamic formation energies. From the results of this chapter, we deduced the importance of microstructure and morphology in influencing macroscopic properties of concrete (in this case, sustenance of high temperatures and pressures). In the next chapter, we will proceed to understand the morphology and kinetics of C-S-H growth during early stages of cement hydration.

Chapter 4

Early stages of cement hydration: Kinetics & nanostructure of C-S-H nucleation and growth

In Section 1.3.3, we described some of the unanswered questions in cement hydration and the potential applications of solutions to these questions. Two of these questions concerned the growth of the C-S-H phase. How do we reconcile the silicate chain model of C-S-H as seen in studies based on NMR spectroscopy with the nanoparticle model that explains its mechanical properties? How does C-S-H grow during the early stages of cement hydration? In Section 1.3.2, we alluded to few direct observations of C-S-H nucleation and growth. Below, we briefly review these studies as context for the work in this chapter.

Gauffinet et al. [13] reported aggregation of nanoparticles ($\sim$ 1000 nm^3) of C-S-H observed using Atomic Force Microscopy (AFM) on an alite pellet wetted with lime solution. A later study by the same authors [14] reports the growth rate of C-S-H to be 0.04 nm/s (0.15 μm/h) and 0.02 nm/s (0.07 μm/h) along parallel and perpendicular directions, respectively to the alite surface. Through electrical conductivity experiments on saturated solutions of lime and silica with and without alite, these authors showed that the time of homogeneous nucleation t_{hom} to be about 20 times larger than that required for heterogeneous nucleation t_{het}, making a case against homogeneous nucleation of C-S-H. In Section 1.3.2, we noted that the boundary nucleation and growth (BNG) model (that assumes heterogeneous nucleation) fitted the calorimetric hydration rate data better than the Avrami model (that assumes homogeneous and heterogeneous nucleation).

Other direct observations of C-S-H growth have involved a technique known as soft X-ray microscopy [76–78]. These studies use qualitative observations on suspensions of C-S-H precursors (lime and silica) or cement clinker (e.g., alite, blast furnace slag) to propose or modify mechanisms of hydration. Gartner et al. observed that the reaction between silica particles suspended in solutions of $CaCl_2$ to garner [76]"indirect evidence" for the silicate sheets based growth mechanism (see Section 1.3.2) of C-S-H. Juenger et al. propose a mechanism for the accelerating effect of $CaCl_2$ on cement hydration [77]. Both the above mentioned studies report a set of micrographs depicting the growth of hydration product

with time, from which one can make estimates of C-S-H growth rate to be greater than 0.13 nm/s or 0.5 μm/h. Because of the high surface/volume ratios inherent to such systems, alite particles and the C-S-H phase growing on it are susceptible to carbonation from CO_2 dissolved in aqueous media [6]. However, none of these studies reports a chemical analysis of the hydration products formed in these systems.

To study suspensions of alite particles in aqueous media, we use a different experimental setup than the one used in soft X-ray microscopy studies mentioned above. Recently, Grossier and coworkers reported a novel experimental design of controlled nucleation of crystalline materials like NaCl and macromolecules like proteins from solution [79,80]. They argue that highly supersaturated metastable solutions could be created through volumetric confinement [81]. For instance in [80], the authors create confined picoliter volumes of NaCl solution on of diameter $\sim$ 0.5 μm on a glass cover slip. These picoliter droplets are then covered with an organic liquid to encourage slow diffusion of water from NaCl solution into the organic liquid, thus forming supersaturated metastable NaCl solutions. Upon manually perturbing such metastable solutions (in this case with the microcapillary), nucleation is initiated, thus providing spatial and temporal control to what is typically a random event. Coupled with optical microscopy, the authors are able to observe *in situ* nucleation and growth in these confined systems. We adopted this approach to study C-S-H nucleation and growth processes. This method also enables us to create an array of independent confined volumes in which we can simultaneously observe nucleation and growth processes. In comparison, the previously reported results on C-S-H growth have all been based on single observations. The subject of this chapter is benchmarking of such novel hydration experiments using timelapse imaging to consider hydration product growth rates and using Raman spectroscopy to confirm the chemical identity of those hydration products.

The results reported in this chapter involved the efforts of several personnel. The setup and protocol for confined cement hydration experiments in picoliter droplets was designed by Dr. R. Grossier during postdoctoral research in the Van Vliet Group at MIT. Growth rates of hydration products inside these droplets were calculated by both Dr. R. Grossier and the author. Raman experiments on these systems were carried out by Dr. N. Ferralis at the Grossman Lab in the Department of Materials Science and Engineering, MIT. Spectra from Raman experiments were interpreted by the author together with Dr. N. Ferralis.

4.1 Materials & Methods

Figure 4.1 shows our experimental setup and its components. A key component of our experiments is the creation of picoliter droplets of hydration water achieved using a microinjector [12]. These microinjectors are connected to microcapillaries [13] that deliver picoliter droplets of fluid upon application of pressure. We mentioned the possibilility of creating an array of independent confined reaction environments. This is achieved using a micromanipulator that enables translatory motion of the microcapillary. We control the translatory motion using a joystick. The hydration reaction between clinker particles and water, both deposited on the glass slide, is observed through an inverted optical microscope[14]. For systematic analysis of the hydration products, we capture images using a 5.5 megapixel sCMOS camera[15] which are analyzed on a local computer.

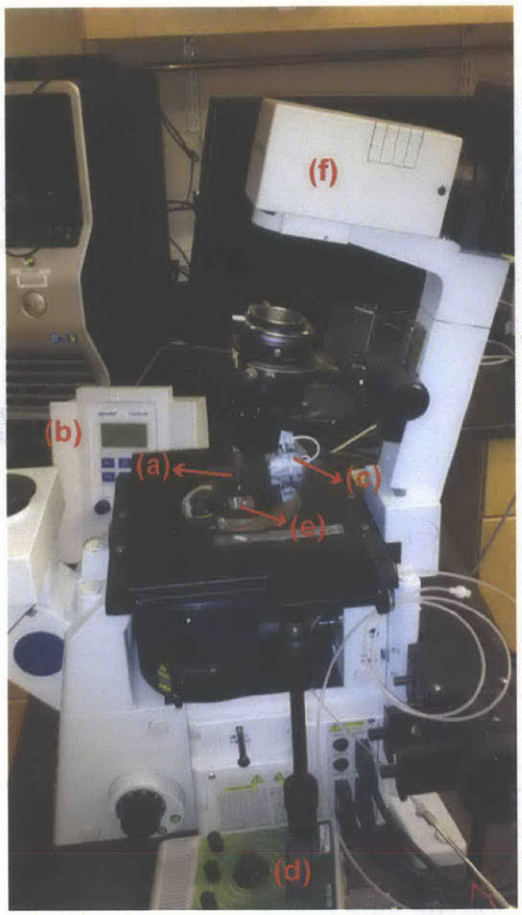

Figure 4.1: Experimental setup. Picolitre droplets of hydrating water are delivered using microcapillaries (a) regulated by microinjectors (b). Micromanipulator (c) controlled by joystick (d) enables 3D motion of the microcapillary. The hydration reaction as it unfolds on the glass slide (e) can be observed through the optical microscope (f). Camera attachment of the optical microscope enables storing and subsequent analysis of images on a local computer.

To create confined reaction volumes with few nucleation events, we use the following protocol. A suspension of monoclinic C_3S is obtained by dissolving 10 g in 50 ml of isopropanol in a plastic centrifuge tube. After some time, C_3S settles at the bottom of the tube leaving clear transparent isopropanol supernatant. Right before an experiment, the contents in the tube are mixed by manual shaking. We shake the tube lightly enough that the supernatant becomes opaque, but not vigorously enough to disturb the C_3S residue at the bottom of the tube. As the particles start to settle again, transparent, translucent and opaque sections develop in the supernatant. Approximately $\sim$ 50 µl sample is drawn from the translucent section (red in Figure 4.2) of the supernatant to deposit on the glass coverslip. When the isopropanol evaporates, it leaves behind an irregular deposit of microscopic clinker particles on the glass slide. When a sample of the suspension (that will be deposited on the glass slide) is drawn either from the fully transparent or opaque sections of the supernatant, we find that the distribution of clinker particles to be either too sparse or too dense. In the latter case,

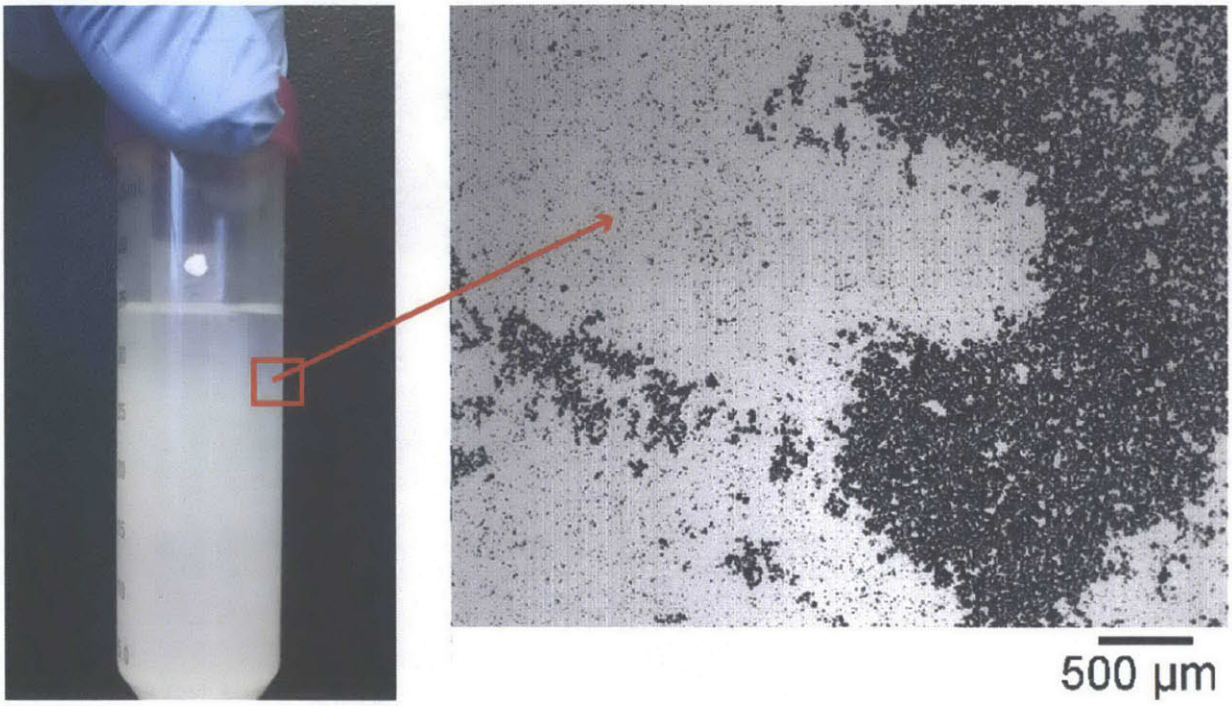

Figure 4.2: Drawing a sample of suspension of alite particles in isopropanol to deposit on the glass slide. Sample taken from translucent section (red) of the supernatant produces a uniform distribution of clinker particles on the glass slide upon evaporation of isopropanol. If the density of clinker particles is too high in the sample (for instance when a sample is drawn from opaque sections of the supernatant), the clinker particles can agglomerate to form clusters.

clinker particles can agglomerate to form clusters (Figure 4.2), defeating the purpose of these experiments to observe hydration on accessible surfaces of clinker particles. A 100 µl of inert paraffin oil is drawn into a pipette to cover this deposit of alite particles on the glass slide. We gently bring the microcapillary in contact with the surface of the glass slide beneath the droplet of oil. We then created sequences of picoliter droplets of aqueous media[16] with diameter $\sim$ 50µm (see Figure 4.3A). We explored four alternatives for hydrating aqueous media: water, NaOH solution (pH 12), saturated solution of CH, and saturated solution of $CaCl_2$.

We captured the evolution of the reaction interface inside the droplet using time lapse photography (Figure 4.4A). Typically, the droplets evaporate after 15 h. We captured a snapshot of the array of droplets (such as that shown in Figure 4.3A) once every 2 minutes for 10 h. Beyond making qualitative observations, knowing the spatial resolutions enabled us to make quantitative analysis of the hydration products that grow inside the droplets. To analyze images for making quantitative deductions, we used Cell Profiler ^{TM} [82], an open source image analysis software with built in functions to track motion of objects in a sequence of images. It has been used successfully to track the motion of biological cells. In this case, we wanted to compute the rate of growth of reaction interfaces inside the droplet (Figure 4.4A). The efficient use of the tracking function required the object to be tracked

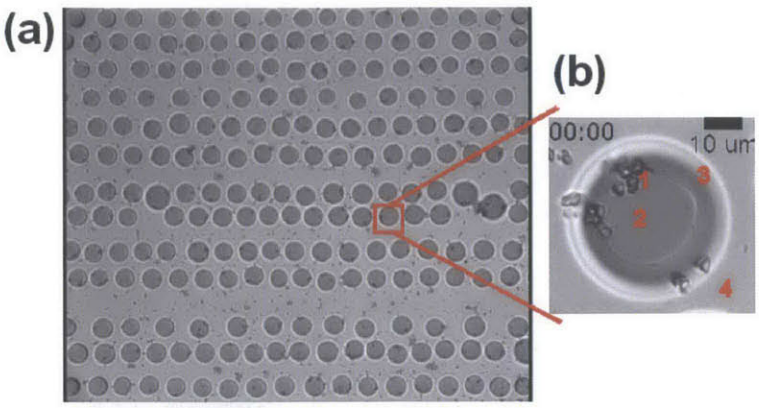

Figure 4.3: (A) Array of picoliter droplets of NaOH pH 12 reacting with microscopic C_3S particles deposited on a glass slide observed under optical microscope. (B) Close-up view of one of the droplets at start of the experiment (time 00:00h) with C_3S particles (1) at the periphery of the droplet of hydrating water (2). Clinker particles are also seen on the the oil-water interface (3) and outside the droplet (4) in contact with oil. These particles do not undergo any reaction.

(such as the edge of the interface) to be starkly distinct from the background. To achieve this contrast, we subtracted the image at timestep $n-1$ from the image at timestep n. For instance, we subtract the image at time = 1h from the image at time = 2h, image at time = 2h from the image at time = 3h and so on. The subtraction of images as a concept is easier to understand if one imagines each image to be an array of pixels, each pixel being a real number ranging from 0 to 1. Visually, the extreme values 0 and 1 represent pixels that are completely dark and totally bright, respectively. The subtraction process then boils down to computing the difference matrix and renormalizing it to make the value of brightest pixel equal 1. The results of this process are shown in Figure 4.4B. This process produced a sequence of images in which we can clearly contrast a white moving edge of the interface from the dark background. This sequence of images were fed to the tracking function which was then able to extract the coordinates of the centroid of the moving edge, and further, its distance travelled and speed as a function of time.

4.1.1 Raman Spectroscopy

We then characterized these systems using Raman spectroscopy. Raman spectroscopy is a vibrational spectroscopic technique. Photons from a laser impinging on a material are scattered inelastically, the extent of which is characteristic of the molecular bonds present in the material, and is measured by the Raman shift [83]. The interaction volume is of the order of 1 μm^3 [83]. Typical applications include local structure determination and qualitative and quantitative analysis of chemical composition. The principal advantages of using Raman spectroscopy are its micro-scale resolution and ability to characterize amorphous materials [84]. We note the relevance of both these advantages to our confined cement hydration systems.

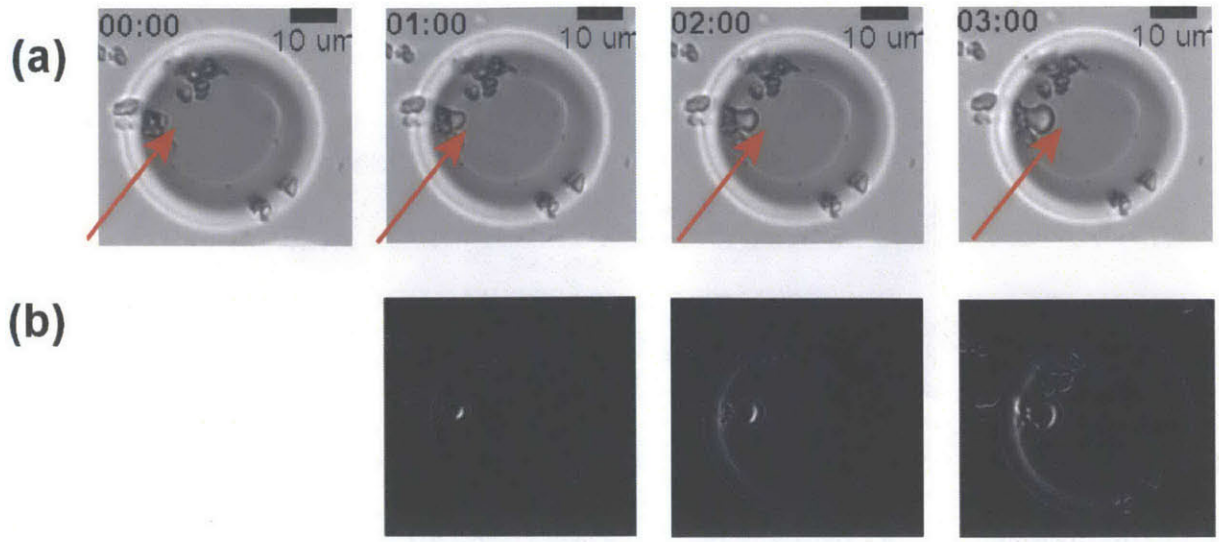

Figure 4.4: (a) Dynamics of reaction interface (red arrow points to leading edge of the interface) inside the droplet captured through snapshots at 0, 1, 2, and 3 hours. At T = 00:00h, the interface becomes detectable at the scale of our observation ($\sim$ µm). (b) To enhance the contrast between the moving interface and the background, we substracted image at time n from that at time $n-1$, $n \geq 1$. The tracking function in CellProfiler can then use the sequence of images in (b) to extract information such as rate of growth of interface.

We discuss the necessary background for Raman spectroscopy of cementitious materials in the context of relevant study by Ibáñez et al. in which they characterize monoclinic C_3S paste of w/c = 1 cured for 30 days and subsequently carbonated for 60 days using Raman spectroscopy [85]. For silicates, the Raman spectrum consists of the so-called internal modes of SiO_4^{4-} [84]. Internal modes are atomic vibrations in a complex ionic group that keep the center of mass stationary[17]. There are two kinds of internal modes, namely bending and stretching, with corresponding vibrations. These internal modes are modified by silicate polymerization and local chemical environments, thus enabling differentiation of phases [84]. The polymerization of silicate groups is represented using Q_n notation where n $\in \{1, 2, 3, 4\}$ denotes the number of Si-O-Si bridges (Section 1.3.2, Figure 1.2). The dominant internal modes for C_3S correspond to stretching vibrations of Q_0 silicates with Raman shifts in the range 800 - 850 cm^{-1} (see Figure 4.5A).

In the Raman spectrum of hydrated paste (Figure 4.5B), the peaks corresponding to clinker phases clearly become less dominant. The new features that emerge must correspond to the hydration products in the paste: C-S-H and CH. $Ca(OH)_2$ has been previously characterized by Raman [86]. Based on previous studies on pure $Ca(OH)_2$, we can attribute sharp responses at 250 and 355 cm^{-1} in Figure 4.5B to Portlandite. There are two broad crests, one centered around 670 cm^{-1}, and the other spanning 800 - 1050 cm^{-1}. Q_2 silicates in C-S-H contribute to the broad feature at 670 cm^{-1}. In their work on synthetic C-S-H, Kirkpatrick et al. [87] detected two characteristic features at 850 cm^{-1} and 1070 cm^{-1}. They assigned these features respectively to stretching modes of Q_1 and Q_2 silicate groups. The stretching modes

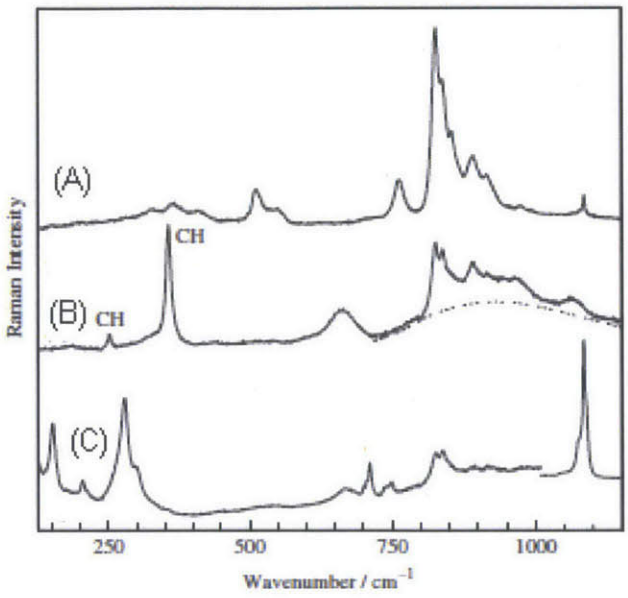

Figure 4.5: Raman spectra of (A) anhydrous monoclinic C_3S, (B) hydrated monoclinic C_3S paste, and (C) hydrated and carbonated monoclinic C_3S paste. From Ref. [85].

of Q_3 and Q_4 silicate groups have higher wavenumbers. Thus, based on characterization of synthetic C-S-H, Ibáñez et al. attribute the broad feature spanning 800 - 1050 cm^{-1} to Q_1 and Q_2 silicate groups in C-S-H [85]. They attribute the broadness to lack of crystallinity of C-S-H. Several studies have attributed this broadness of C-S-H signature to lack of definitive crystal structure [83,84,88]. They do not refer to any specific characteristic of the structure, but rather its low structure factor.

Carbonation in cement pastes can occur by reaction of CO_2 with CH, C-S-H and anhydrous C_3S [85]. The isolated CO_3^{2-} group has a dominant stretching mode at 1085 cm^{-1} and a slightly weaker external mode at 280 cm^{-1} [83,84]. Decalcification of C-S-H in the presence of CO_2 will reduce its C/S ratio, which in turn has been shown to induce polymerization in silicate chain structure of C-S-H as measured by the increase in proportion of Q_3 and Q_4 silicate groups [87]. In the carbonated paste (Figure 4.5C), we note that the signal attributed to $CaCO_3$ is strong. Clinker and CH signatures have been subsumed (compare to Figure 4.5B). The broad features associated with C-S-H have also been relatively muted (compare Figure 4.5B and C). Further, Ibáñez et al observe that there are local variations (at different physical locations of the sample at length scale of $\sim$ 1 μm) in the Raman spectrum of the carbonated waste. Notably, at some locations they notice broad features in 1050 - 1100 cm^{-1}, which they argue corresponds to Q_3 and Q_4 silicate groups that result from carbonation [85].

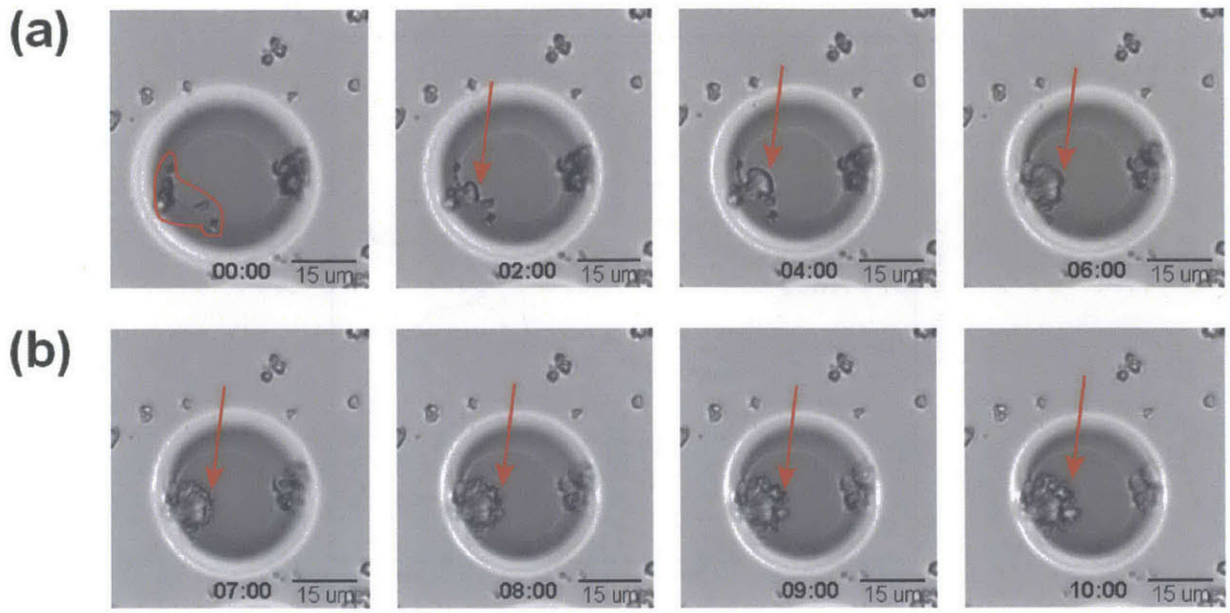

Figure 4.6: Evolution of the growth front of the hydration product inside the droplet. Clinker particles inside the red loop at t = 0 h contribute to the growth of the product. The red arrow (from t = 2 h onwards) points to the approximate centroid of the growth front. (a) Initially (in this case, from 1 - 6 h), the growth front can be approximated as an arc. (b) Eventually (in this case, after 7 h), the arc-like growth front breaks up to develop rough "finger-like" projections.

4.2 Results & Discussion

First, we report qualitative and quantitative results from our analysis of images of growth of hydration products inside the droplet. We compare these results to the studies described in the beginning of this chapter. Second, we present results from our Raman experiments on products growing inside the droplet. We interpret these results in light of previous studies on early stages of cement hydration presented at the beginning of this chapter and in Section 1.3.

The sequence of images Figure 4.6A captures the growth of the hydration product interface inside our droplets. Note that the two-dimensional (2D) projection of the product is growing in a radially symmetric fashion, i.e., the growth front (pointed to by the red arrows in Figure 4.6A) can be approximated as an arc of a circle. It is likely that the growing product is adopting the symmetry of the space into which it is growing, which happens to be a droplet with rotational symmetry in 2D. Hence, our approach of tracking the motion of the centroid of the growth front to quantify the dynamics of the interface. In all of the droplets with such growth of a product, we observed a transition in the growth front at later times. The arc like interface breaks up to form "finger-like" projections, losing its radial symmetry (Figure 4.6B). This transition is accompanied by a distinct change in the texture of the product as perceived by the microscope (contrast the product near the growth front in Figure 4.6A and B). In the beginning of the chapter, we referred to an AFM based study

of C-S-H growth on lime wetted C_3S pellets [14]. Interestingly, the authors of this study also report " the C-S-H assemblage is very dense and flat from the beginning of the C-S-H precipitation up to the point where the alite surface is virtually covered ... [after which] the morphology of the C-S-H [phase] becomes quite different, it is less dense and more porous." Note the geometry of their experiment was a flat pellet facing an infinite half space and the growing product (described as being flat) seems to inherit the corresponding symmetry. In our experiments as well, we observe this transition after all the particles contributing to the growth of the hydration product are covered by the hydration product. This can be seen in Figure 4.6A, by t = 6 h, all the alite particles that have contributed to the growth of the product (marked by the red loop in t = 0 h, Figure 4.6A) have been covered by the product. The authors do not report the time when this transition occurs. In our experiments, the time for this transition varies from droplet to droplet, which indicates which indicates the variation of this unstable growth front on either the clinker particle geometry or crystallographic orientation of the exposed facet. The authors in Ref. [14] interpret this change in texture/morphology as a transition from interface controlled kinetics to diffusion driven kinetics.

Our quantitative results on the growth rate of interface up until this transition also hint towards lack of diffusion control. If the rate of reaction were controlled by diffusion, then the

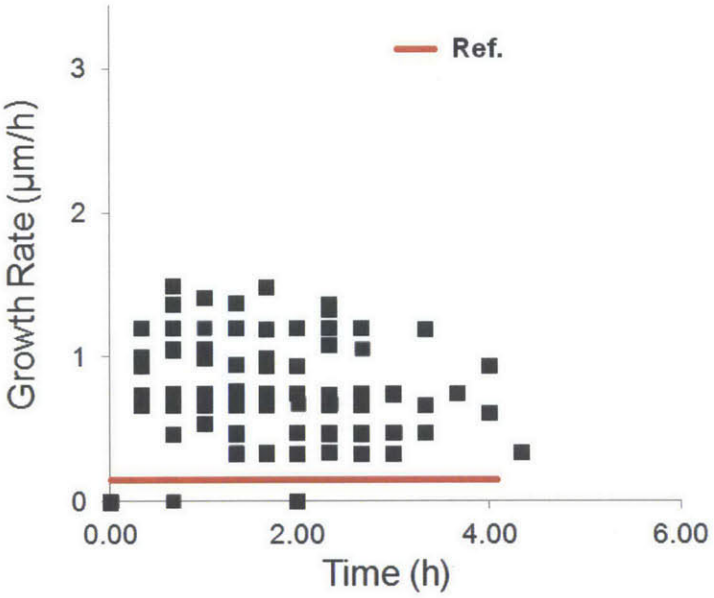

Figure 4.7: Growth rates of hydration product computed by tracking growth fronts of 30 interfaces using image analysis algorithms. These growth rates were calculated for C_3S particles reacting with droplets of NaOH pH 12. This growth rate is of the same order of magnitude as that calculated by Ref. [14] up until the morphology of the hydration product changes. To illustrate hydration product with "flat" morphology (and hence constant growth rate), authors in Ref. [14] show an AFm image taken at t = 4 h. Thus, we can infer that the hydration product they observe has a constant growth rate for at least 4 h.

growth rate would have a parabolic dependence with time, steeply decaying at later times. Figure 4.7 shows the results of our image analysis. We report growth rates of the interface up until the growth front remains an arc. We find average growth rates of 0.5 μm/h. There is a gradual decrease of growth rates with time. Interestingly, the different spatial distribution of clinker particles in each droplet does not seem to have noticeable effects on the growth rate of hydration product interface. However, we must be cautious in interpreting these results. There is no rigorously defined error in these image analysis measurements. If the resolution of the images used in this analysis is any indication (2 pixels/μm), the error could be comparable to the measured growth rates. Even if that were the case, we can assert that the clinker particle distribution within/around the droplet influences the growth rate of the hydration product interface within an order of magnitude. We note that our growth rates are the same order of magnitude as that reported in Ref. [14] for a flat growth front. We also note that the growth rates are relatively constant over the measured time periods. If the reaction were controlled by diffusion, the average growth rate at t = 2 h would be 4 times lesser than that at t = 1 h, that at t = 3 h would be 9 times lesser, and so on. Since we do not observe such a drastic decay of growth rates, we can deduce that the kinetics of the reaction generating the product is controlled by reaction at the interface as noted before from Ref. [14]. The authors of this study do not confirm the chemical identity of the hydration product. However, they report that this hydration product grows by the aggregation of nanoparticles [14] (resolved using AFM to have dimensions of around 1000 nm^3), which is unlikely of any crystalline phase.

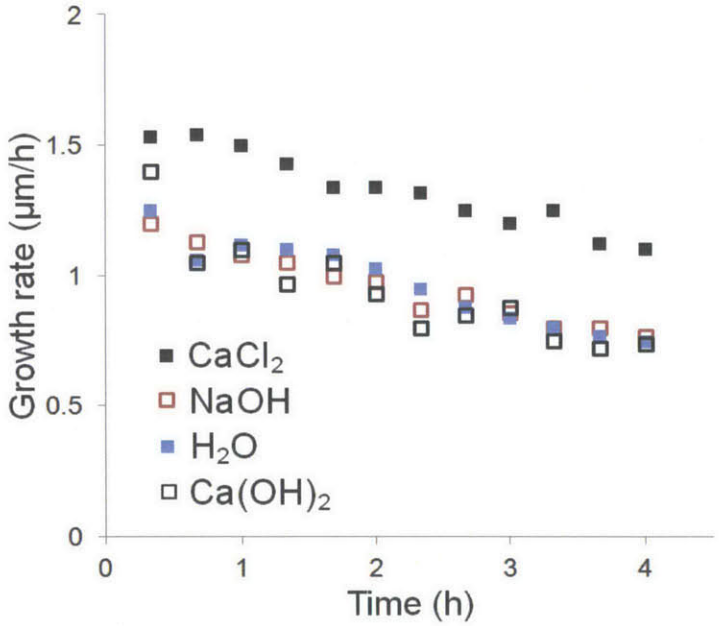

Figure 4.8: Average growth rates of hydration product computed by tracking growth fronts for different compositions of hydrating water: saturated solution of $CaCl_2$, NaOH pH 12, water, and saturated solution of $Ca(OH)_2$. Growth rates of hydration product in reactions of C_3S with water and saturated solution of $Ca(OH)_2$ as measured by R. Grossier.

Further, we explored the influence of the aqueous media on the average growth rates of hydrating products. These results are summarized in Figure 4.8. Among the four alternatives we tried for aqueous media, the growth rates of hydration product were identical in water, NaOH pH 12, and saturated solution of $Ca(OH)_2$. A saturated solution of $CaCl_2$ produced a higher growth rate ($\sim$ 1.5 times) than the rest. $CaCl_2$ is a known accelerator [4, 77], however the mechanism by which it enables a faster rate of hydration has not been proven conclusively [77]. Based on qualitative observations from x-ray microscopy studies of C_3S suspensions in $CaCl_2$ solution, Juenger et al. [77] propose that C-S-H formed in the early stages of hydration around the C_3S particle is more porous (than the one that forms in the control sample without $CaCl_2$) enabling faster diffusion of water, and calcium and silicate ions and thus, higher growth rates of C-S-H. On the other hand, Thomas et al. [16], based on modelling of experimental data from calorimetric experiments, propose that $CaCl_2$ would influence the nucleation of C-S-H, but would not affect the growth rate of C-S-H. If the hydration product growing inside our droplets is C-S-H, then it would support the mechanism proposed by Juenger et al. [77].

To confirm the chemical composition of the hydration product growing inside these droplets, we use Raman spectroscopy. We identified the product to be $CaCO_3$ (Figure 4.9). Figure 4.9 also shows the spectrum of paraffin oil (grey). The spectra of hydration products show certain elements of the paraffin oil spectrum, with broad features between 700 - 900 cm^{-1}. However, the dominant signature can be identified as $CaCO_3$. We carried out several such experiments and in all of these experiments, we identified the growing hydration product as $CaCO_3$. Interestingly, in the results from image analysis, tentatively assumed that the hydration product was C-S-H, and refer to that unvalidated supposition as "putative C-S-H." We noted its similar growth rates to those measured in Ref. [14]. From the same reference, we also noted the transition of the growth front and the morphological change in the product. We found that $CaCl_2$ accelerated the growth rate of this product. The authors in Ref. [77] proposed increased growth rates of C-S-H as a mechanism for the accelerative effect of $CaCl_2$ on cement hydration. However,However, we find that our assertion, based on several pieces of empirical evidence, is rejected by our Raman spectra. This emphasizes the importance of carrying out chemical characterization tests to identify hydration products, especially in hydration experiments involving dilute suspensions of cement clinker particles which are highly susceptible to dissolved CO_2 in aqueous media [6]. In the beginning of this chapter, we lamented about the lack of such rigorous characterization in several of the previous studies on early stages of cement hydration.

Because our experiments are not designed to be completely CO_2 free, we investigated if longer degassing times could delay the formation of carbonates. Although, we cover the aqueous droplets with oil, owing to its finite solubility in oil, water diffuses out from these droplets into oil and this process is typically complete after $\sim$ 15 h. This was the time frame within which we could conduct hydration experiments. After a few trials, we found that water degassed for more than a day (compared to 3 h previously) prevented the formation of carbonates for at least 12 h. Using this degassing protocol, we attempted to observe the evolution of Raman spectra of products growing inside these droplets. We report representative spectra collected at 2, 3, 9, 12 and 18h after hydration of C_3S particles in NaOH solution of pH 12.

Figure 4.10 shows the evolution of the Raman spectrum of the phases inside the droplet

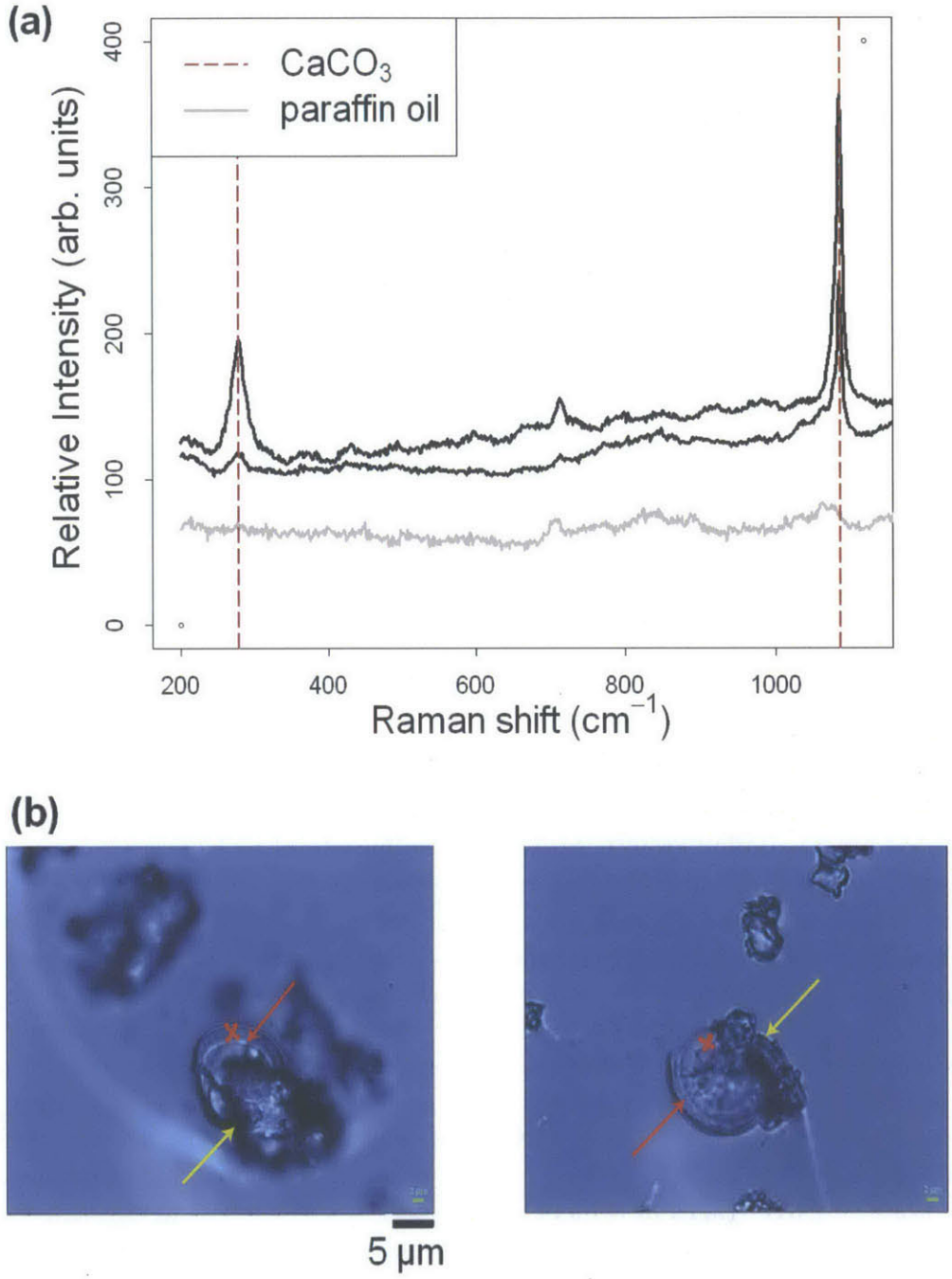

Figure 4.9: Raman spectra of C_3S particles in NaOH pH 12 after 2.5 h of hydration. We wanted to characterize the products whose growth rates we had computed with image analysis. The micrographs show the radially symmetric products as having grown from irregularly shaped alite particles. These products are visually similar (in shape) to those seen in Figures 4.4A and 4.6A. Red crosses in the micrographs indicate the location where the spectra were captured. Raman spectroscopy has an interaction volume of $\sim 1\mu m^3$.

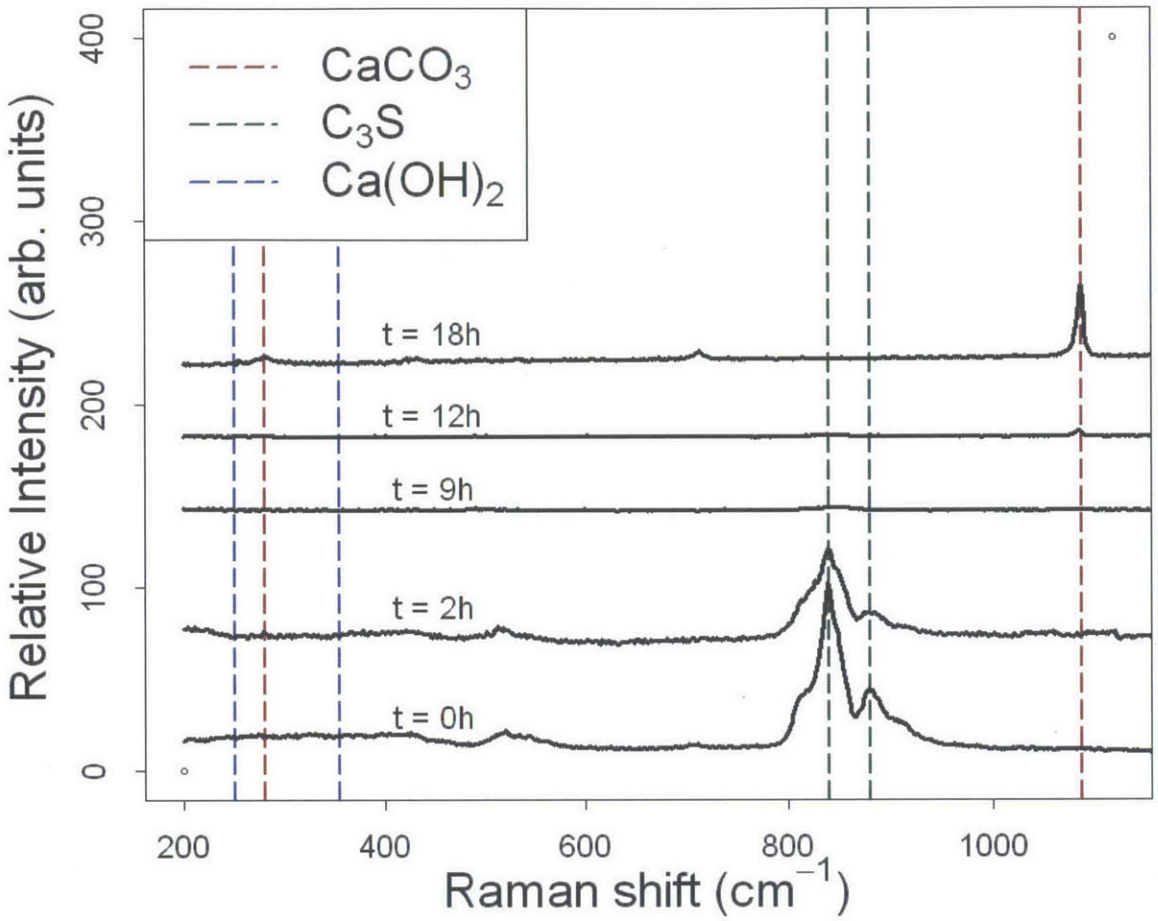

Figure 4.10: Evolution of Raman spectra collected on the surface of C_3S particle covered in NaOH pH 12.

with hydration time. We note two familiar features from the discussion on Raman spectroscopy in the Materials & Methods section: internal modes of Q_0 silicates in anhydrous C_3S between 800 - 900 cm^{-1}, and stretching vibration of CO_3^{2-} in $CaCO_3$ at $\sim$ 1100 cm^{-1}. We notice that carbonates start to form at 12 h. In the 18 h spectra, we can deduce that calcium carbonate is the dominant phase. We noted that droplets evaporate at $\sim$ 15 h. It is likely that as water diffuses out of the droplets into oil, the concentration of bicarbonate ions in hydrating water increases until the ionic product of concentrations of calcium and bicarbonate ions exceeds the solubility product of the corresponding carbonate. In the spectra corresponding to 2, 9 and 12 h of hydration, we notice that: (1) clinker signature decays with hydration time, and (2) the major hydration product (which we shall refer to as X) does not seem to have a distinct Raman signature. If X = $CaCO_3$, as seen in 18h spectra, we would have seen a sharp signal at $\sim$ 1100 cm^{-1}. If X = CH, we would have seen a distinct signature around 350 cm^{-1}. By elimination, X = C-S-H. If so, what about its Raman signature?

In Section 1.3.2, we described NMR based studies that demonstrate that in the early stages of hydration (until $\sim$ 100 h), the silicate structure of the C-S-H phase is dominated by Q_1 silicates. One may initially assume that time scales of hydration processes are much shorter for our microscopic C_3S particles suspended in NaOH pH 12 when compared to conventional pastes like the one used in the NMR study. However, Damidot et al. have shown using calorimetry based experiments that there is little difference in time scales of various stages of hydration (see Section 1.3) between pastes of water/cement ratio (w/c) $\sim$ 1 and suspensions of water/cement ratio $\sim$ 1000 [89]. From Figure 4.3B, we note that the edge length of each clinker particle is approximately 3 μm. The diameter of the droplet is 30 μm. Assuming each clinker particle to be a cube of side 3 μm and density of 2.5 g/cm^3 [6], the w/c ratio of a droplet with one clinker particle would be 100 - 200, 100 being the case when the droplet is approximately a hemisphere, and 200 when the droplet is a full sphere. If we assume a maximum of 10 such clinker particles in each droplet, the w/c ratio in our experiments is of the order of magnitude 10^1 - 10^2. Given our w/c ratios are less than 1000, the hydration times in our experiments are reasonably assumed (via Ref. [89]) to be same as those in conventional pastes. Hence, we can infer from NMR studies on conventional pastes that C-S-H in our experiments would consist mainly of Q_1 silicates. Why don't we observe the signature of Q_1 silicates in t = 9, 12h spectra in Figure 4.10 where we deduced the major phase has to be C-S-H? Is Raman spectroscopy less sensitive to Q_1 silicates? Studies on synthetic C-S-H [87], which report a distinct signature of Q_1 silicates, would disagree with that argument. If C-S-H is the dominant phase in the volume that we probe in Raman spectroscopy, then the only other rationale for lack of any signal could be its low absolute mass (i.e., low density or high porosity) or more micron-scale disorder than C-S-H in mature pastes. A relevant recent study suggests that it could be low density. We refer to a recent high resolution TEM study of early hydration by Galluci et al. [90]. The authors in this study have identified methods to prepare TEM samples of OPC pastes after a mere 2 h of hydration. Typically, only mature pastes (1 month or older) with significant mechanical strength are subjected to the intense sample preparation process required for TEM [90]. In this study, they report qualitative observations on the evolution of the C-S-H structure from such an early stage of cement hydration. Relevant to our experiments, they report a "fragile C-S-H" phase forming as early as 4 h [90]. Further, they report that this "fibrous C-S-H [which] appears to have a lower packing density than the rest of the hydration products. [90]" Based on their studies on pastes hydrated for up to 2 days of hydration, they conclude that this low density C-S-H phase forms the denser conventional inner product or Ip (see Section 1.4) C-S-H after 24 h.

4.3 Summary

The following is a summary of the results of our attempts to visualize and quantify the *in situ* hydration kinetics of nucleation and growth of the C-S-H phase:

1. Did we measure growth rates of C-S-H during early stages of hydration? No. We attempted to measure growth rates of C-S-H for various compositions of aqueous media. We analyzed the images of alite hydration for various alternatives of aqueous media. We noted empirical agreement on several deductions with previous "direct" observations of

the C-S-H phase. However, unlike many of the previous studies, we characterized the supposed C-S-H phase in our experiments and found out that it was $CaCO_3$. As we noted, our results emphasize the need to rigorously characterize supposed hydration products, especially in experiments involving suspensions of alite particles which may be all the more susceptible to carbonation.

2. Did we avoid carbonation? Partly. We were able to delay carbonation of products inside our droplets by degassing the aqueous media for longer times. However, this was a result of trial and error. For future work, it is better to pursue a stronger strategy that aims at eliminating carbonation. This could involve moving synthesis of droplet samples into a glove box filled with inert atmosphere. However, the whole assembly of microscope and microinjectors cannot easily be accommodated inside a glove box.

    - One alternative could be to load the microcapillaries with aqueous media inside a glove box. Would the $\sim$ 100 nm diameter of the microcapillary be enough to prevent CO_2 in air from dissolving in aqueous media when the microcapillary is brought back into normal atmosphere?
    - Another alternative could be to use μl droplets delivered by regular pipettes instead of picoliter droplets from microcapillaries regulated with microinjectors. We would lose the distinct advantage of using picoliter droplets, which enabled us to focus on the small number of alite particles inside each droplet instead of a sea of alite particles deposited on the glass plate. Thus, the use of picoliter droplets simplified the subsequent acquisition and analysis of timelapsed images. One way to overcome this difficulty would be to synthesize C_3S pellets of size $\sim$ 0.5 mm. Microliter droplets of water deposited on glass have a diameter of around 1 mm.
    - A third possible alternative is to degas water, and then preserve the droplets sample in a humid atmosphere. Then the experiments would not require oil and concentration of dissolved bicarbonate ions in aqueous media would never become high enough to induce the precipitation of carbonates.

3. Were the characterization tools able to detect C-S-H? No. The structure of the C-S-H phase has typically been studied using electron microscopes with resolution in 100 nm range. We hoped to characterize the composition and nanostructure of C-S-H with Raman spectroscopy. However, we found that Raman Spectroscopy may not be well suited to study the structure of C-S-H within hydration times less than 1 day. In Ref. [90], the authors report that a low density of C-S-H exists for up to 1 day after which it transforms into denser forms of C-S-H seen in mature pastes, for which Raman Spectroscopy has been shown to be valuable [83, 84, 88].

    Another consideration concerns the volume of C-S-H that will form in the first 10 - 20 h of hydration of alite. From a variety of studies that have evaluated the degree of hydration of alite as a function of time using techniques such as NMR [23], calorimetry [4] and electrical conductivity [14], we can conclude that the degree of hydration of alite within 24 h would be less than 10%. Degree of hydration is the ratio of mass of C-S-H

to the original mass of clinker at the start of hydration. Irrespective of whether the C-S-H phase is Inner Product (grows into clinker particle, i.e., replaces it) or or Outer Product (grows into aqueous media), would the optical microscope would be able to detect such a small fraction of the alite particle, which it self is of the dimension of around 3 μm? At a magnification of 100X (the maximum in most optical microscopes), the ideal resolution of the optical microscope is 0.2 μm [91]. For degree of hydration of 10%, we can expect the C-S-H phase to grow to comparable dimensions on our clinker particles (of size $\sim$ 3 μm) after 24 h of hydration. A better alternative here would using an environmental scanning electron microscope (ESEM) that can characterize wet samples.

Chapter 5

Conclusions

5.1 Summary of Results

In Chapter 2, we experimentally validated a key result from molecular simulations on the C-S-H phase: existence of polymorphic C-S-H structures i.e., C-S-H structures having identical composition, but different mechanical properties. We described the synthesis of numerous cement pastes with C-S-H phase of diverse Ca/Si ratios ranging from 1.29 to 1.88. We found several pairs of cement pastes in which the Ca/Si of the C-S-H phase was the same, however the mechanical properties of the C-S-H nanoparticle were different, proving the existence of polymorphic structures. Molecular simulations of the C-S-H phase also predict the stiffest and hardest C-S-H polymorph has a Ca/Si ratio close to 1.5. Of the 30 samples we synthesized, we found the stiffest and hardest C-S-H phase in B'40NO with Ca/Si ratio of 1.68 $\pm$ 0.1, which is consistent with the prediction. We also explored the influence of mechanical properties of the C-S-H nanoparticle on higher scale mechanical properties. Our microindentation experiments showed that presence of additives such as fly ash is more influential than the mechanical properties of the C-S-H nanoparticle on the microscale mechanical properties of cement paste. On the other hand, we also showed that in pastes without additives, the mechanical properties of the C-S-H nanoparticle has a significant influence on the microscale mechanical properties of the cement paste.

In Chapter 3, we applied our methods to a commercially used concrete, ultra high performance concrete (UHPC), to inform the design of concrete for protective infrastructure. We found the C-S-H nanoparticle in UHPC to be significantly stiffer and harder than the C-S-H nanoparticle in ordinary portland cement (OPC). Notably, this result agreed with molecular simulations on the C-S-H phase that predict such a difference based on the different Ca/Si ratios of C-S-H phase in UHPC and OPC. We also found that steel fibers played an interesting role in the UHPC matrix. They locally decreased the packing density of the C-S-H phase, in other words, a less stiff and less hard C-S-H phase comprising many C-S-H nanoparticles or "grains". Further, they also create capillary porosity in the UHPC matrix which is known for its reduced porosity due to efficient packing of constituent phase. Although the effects of steel fibers on the UHPC matrix as described above seem pejorative, we argue that they could especially be beneficial in the context of designing concrete that can resist high impact projectiles. Given that mechanical failure under these conditions occurs due to build up of

pore pressures, we argue that capillary porosity can alleviate such concerns. We also find that the C-S-H phase in UHPC is heat resistant up to at least 400°C.

In Chapter 4, we studied the growth of C-S-H phase during the early stages of cement hydration. We used a novel experimental setup that provided access to surfaces of clinker particles exposed to hydration water, thus enabling direct observations. Through such observations, we measured the growth rates of supposed C-S-H phase which were in agreement with previous measurements of the growth rate of C-S-H phase. However, our Raman spectroscopy experiments showed the phase in question to be calcium carbonate. These experiments showed the importance of rigorous chemical characterization in experiments involving direct observations of the C-S-H phase because of the imminent problem of carbonation due to dissolved CO_2 in aqueous media. We were able to able to delay carbonation of our samples enabling us to characterize C-S-H that grows in the first $\sim$ 10 h of alite hydration. This early stage C-S-H does not have a Raman signature, which using evidence from a recent study, we were able to attribute to its high porosity.

5.2 Contributions

1. We validated the existence of polymorphic structures of the C-S-H nanoparticle predicted by molecular simulations through chemomechanical testing of cement pastes. In our experiments, we observe that the C-S-H nanoparticle of a given composition, as quantified by Ca/Si ratio, can possess a range of stiffness and hardness values. In other words, composition of the C-S-H nanoparticle does not uniquely determine the mechanical properties, stiffness and hardness, of the C-S-H nanoparticle.

2. Incorporation of steel fibers in UHPC leads to the development of sub-micron capillary porosity. By comparing the microscale indentation modulus voxel maps of UHPC with and without steel fiber reinforcements, we deduced that steel fibers disrupt the efficient packing of constituent particles in UHPC to create sub-micron capillary porosity.

3. UHPC is unaffected by heat treatment up to 500°C. Our nanoindentation experiments on UHPC samples, both pristine and heated to 500°C (and subsequently cooled) show that the probability distribution of microscale indentation modulus of the UHPC remains unaffected after heat treatment.

5.3 Directions for Future Work

5.3.1 How to reliably synthesize C-S-H phase with specific nanoscale properties?

We attempted the use of Taguchi design of experiments to elucidate the influence of various synthesis factors of cement paste on the nanoscale properties of the C-S-H phase, specifically its Ca/Si ratio, stiffness and hardness of the C-S-H nanoparticle. However, we noted the strong interactions between synthesis factors of cement paste as one of the possible reasons

for the failure of our study. It would then be more appropriate to use smaller full-factorial designs.

The similar thermodynamic stability of C-S-H polymorphs, as evaluated from our collaborators' molecular scale simulations, suggests that attaining the stiffest and hardest C-S-H nanoparticles depends strongly on the kinetics of cement hydration. Temperature is always a factor that influences the kinetics of any reaction. This factor should certainly be invoked in all experimental designs. On the other hand, one must remain skeptical about the use of additives. For instance, they may produce lower Ca/Si ratios of the C-S-H phase resulting in stiffer and harder C-S-H nanoparticle than in the control sample without additives. However, we also noted that use of fly ash tends to decrease the microscale mechanical properties of cement paste and therefore, possibly to macroscale mechanical properties. Therefore, effects on properties at multiple scales must be factored into experimental design. We also noted that the pH of the aqueous media has no effect on the nanoscale properties of the C-S-H phase.

5.3.2 Influence of mechanical properties of the C-S-H nanoparticle on mechanical properties of concrete

We took first steps in this direction using our microindentation experiments. Concrete is a complex system with a multiscale hierarchical structure. Thus, even if we conducted macroscale compression tests on cement pastes to elucidate the influence of the stiffness and hardness of the C-S-H nanoparticle on mechanical properties at higher scale, one can still question the applicability of our results to realistic concrete systems. The skepticism concerns the presence of multiscale porosity in concrete.

This issue can partly be resolved by controlling the porosity in concrete; ultra high performance concrete (UHPC), for instance, is engineered to have low porosity. We showed the applicability of our methods to this commercially available concrete formulation in Chapter 3. UHPC can be used to perform benchmarking experiments that evaluate the potential of the C-S-H phase to influence the properties of concrete. We demonstrated in Chapter 3 so that the C-S-H nanoparticle of Ca/Si = 1 is around 10% stiffer and 100% harder than that of Ca/Si = 1.7. To test whether such an increase in stiffness and hardness increases the compression strength of concrete, consider the following thought experiment. We synthesize an experimental concrete formulation by substituting silica rich cement and silica fume in UHPC with ordinary portland cement (OPC). However, we ensure that the porosity of this experimental concrete is low by achieving particle-particle contact identical to that in UHPC. Then, we compare this experimental concrete with our control sample UHPC for the nanoscale properties of the C-S-H phase and macroscale compression strength. It is likely that Ca/Si of the C-S-H phase in the experimental concrete would be 1.7, and in we know how its nanoscale stiffness and hardness compare with those of the C-S-H phase of Ca/Si = 1 found in UHPC. The correlation between macroscale compression strengths of concrete samples and nanoscale stiffness and hardness of the C-S-H phase quantifies the influence of C-S-H nanoscale properties on macroscale properties of concrete. Importantly, such a quantitative estimate would be an upper bound given the low levels of porosity in our concrete samples. We can expect higher levels of porosity , typical of ordinary concrete, to lessen

the correlation between the nanoscale properties of the C-S-H phase and the macroscale properties of concrete.

5.3.3 Use of porosity in materials for protective infrastructure

We found that steel fibers create capillary porosity in UHPC due to their geometry from its other constituents. When high impact projectiles are fired at concrete slabs, build up of pore pressure is one the principal reasons for mechanical failure. We argued that porosity might be beneficial in countering such pore pressure build ups, thus improving resistance to failure. Of course, we acknowledge that high levels of porosity tend to also reduce the fracture toughness of concrete, so this is a design trade-off. But within these constraints, the concept of using capillary microporosity to improve the properties of concrete raises several interesting questions. First, if porosity resulting from addition of fibers to UHPC is a purely geometric effect, we could potentially use other fibers that could bring down the cost of manufacturing of UHPC. For instance, can cheaper natural textile fibers produce the same microcapillary porosity as steel fibers? Additionally, note that natural textile fibers are sustainable alternatives to steel fibers, which have a relatively larger carbon footprint from metallurgical processing. Second, taking a page from design of aerated concrete that provides improved thermal resistance, we can explore if mere provision of porosity without the use of fibers could provide the same benefits. Third, moving from material design to infrastructure design, could we use UHPC with different levels of porosity or fiber content in different parts of the infrastructure? For instance, could the inner most part of infrastructure that is closest to people and other valuable resources be made of UHPC that is the most resistant to failure from impact of high velocity projectiles, while outer parts could be made of relatively less resistant UHPC?

5.3.4 Influence of hydration water chemistry on hydration of alternative cement clinkers

We discussed our novel experimental setup for studying cement hydration in Chapter 4. One of the principal strengths of this experimental setup is measuring the influence of composition of hydration water on cement hydration. One of the significant applications of such a study would be on alternative clinkers, like ground blast furnace slag and fly ash, which are notorious for their slow hydration kinetics. These materials will become predominant in concrete in the future owing to sustainability concerns of OPC. Further, little or no knowledge exists of the hydration processes in these materials. Therefore, by exploring means to accelerate the hydration reaction of these materials through aqueous media of various compositions, we would have a definitive impact on the concrete industry.

Appendix A

Materials used in cement paste synthesis

A.1 Monoclinic C_3S

Source: Grace Construction Products Ltd., Cambridge MA

Purity tested by X-ray diffraction.

A.2 β-C_2S

Source: Grace Construction Products Ltd., Cambridge MA

Purity tested by X-ray diffraction.

A.3 White Portland Cement

Source: Lehigh® - Heidelberg Cement Group, Brooklyn NY

Compostion in wt%:

Component	Proportion (%)
SiO_2	24.33
CaO	68.58
Al_2O_3	2.00
Fe_2O_3	0.34
MgO	0.65
SO_3	2.17

A.4 Lafarge Portland Cement (Grey Cement)

Source: Grace Construction Products Ltd., Cambridge MA

Proportions of components as described in AASHTO M240 standard [92].

A.5 Brayton Point Class F Fly Ash

Source: Headwaters Resources, Taylorsville GA

Compostion in wt%:

Component	Proportion (%)
SiO_2	57.56
CaO	1.41
Al_2O_3	26.89
Fe_2O_3	5.28
SO_3	0.19
Alkali oxides	1.01

Notes

[1]cran.r-project.org/web/packages/mclust/mclust.pdf

[2]William Barker and John Fournelle, University of Wisconsin-Madison, http://www.geology.wisc.edu/ johnf/660.html

[3]http://web.mit.edu/e-probe/www/

[4]Floor(x) = $\lfloor x \rfloor$ is the largest integer not greater than x

[5]Analog vortex mixer (VWR Scientific Products, West Chester, PA)

[6]Isomet® Low Speed Saw (Buehler Ltd., Evanston, IL)

[7]Nanotest® (Micro Materials Ltd, Wrexham, United Kingdom)

[8]CSM Instruments, Needham MA

[9]MagicPlot, http://magicplot.com/index.php

[10]Lorentzian and Gaussian peaks produce identical results [57].

[11]Wikipedia: http://en.wikipedia.org/wiki/Pearson_product-moment_correlation_coefficient

[12]Femtojet, Eppendorf-Nethler-Hinz, GmbH Hamburg, Germany

[13]Femtotip, Eppendorf-Nethler-Hinz, GmbH Hamburg, Germany

[14]Olympus America Inc, Chelmsford MA

[15]Andor Technology PLC, Belfast, Ireland

[16]We degassed aqueous media in vacuum of 29" Hg for $\sim$ 3 hrs and loaded the microcapillary in a fume hood.

[17]By contrast, in external modes complex ionic groups vibrate as a rigid unit.

Bibliography

[1] F.J. Ulm. What's the matter with concrete? *Atti del XX Convegno Nazionale del Gruppo Italiano Frattura*, page 3, 2008.

[2] J.L. Cohen and G.M. Moeller. *Liquid stone: new architecture in concrete.* Princeton Architectural Press, 2006.

[3] Portland Cement Association. *Design and control of concrete mixtures.* Portland cement association, 1979.

[4] J.W. Bullard, H.M. Jennings, R.A. Livingston, A. Nonat, G.W. Scherer, J.S. Schweitzer, K.L. Scrivener, and J.J. Thomas. Mechanisms of cement hydration. *Cement and Concrete Research*, 41(12):1208–1223, 2011.

[5] G. Constantinides, F.J. Ulm, and K. Van Vliet. On the use of nanoindentation for cementitious materials. *Materials and Structures*, 36(3):191–196, 2003.

[6] H.F.W. Taylor. *Cement chemistry.* Thomas Telford, 1997.

[7] D. Damidot, F. Bellmann, B. MÃser, and T. Sovoidnich. Calculation of the dissolution rate of tricalcium silicate in several electrolyte compositions. *Cement, Wapno, Beton*, (2):57–67, 2007.

[8] EM Gartner, JF Young, DA Damidot, and I. Jawed. Hydration of portland cement. *Structure and performance of cements*, 13:978, 2002.

[9] H.M. Jennings. Aqueous solubility relationships for two types of calcium silicate hydrate. *Journal of the American Ceramic Society*, 69(8):614–618, 1986.

[10] J.W. Bullard. A determination of hydration mechanisms for tricalcium silicate using a kinetic cellular automaton model. *Journal of the American Ceramic Society*, 91(7):2088–2097, 2008.

[11] A. Nonat. Modelling hydration and setting of cement. *Ceramics*, 92:247–257, 2005.

[12] J. N. Maycock, J. P. Skalny, and R. S. Kalyoncu. Solid-state defects and clinker mineral hydration. *Am.Ceram.Soc.Bull.*, 53:326, 1974.

[13] S. Gauffinet, E. Finot, E. Lesniewska, and A. Nonat. Direct observation of the growth of calcium silicate hydrate on alite and silica surfaces by atomic force microscopy. *Comptes Rendus de l'Academie des Sciences Series IIA Earth and Planetary Science*, 327(4):231–236, 1998.

[14] S. Garrault, E. Finot, E. Lesniewska, and A. Nonat. Study of csh growth on c_3s surface during its early hydration. *Materials and structures*, 38(4):435–442, 2005.

[15] M. Zajac. *Etude des relations entre vitesse d'hydratation, texturation des hydrates et résistance mécanique finale des pâtes et micro-mortiers de ciment Portland.* PhD thesis, 2007.

[16] J.J. Thomas, J.J. Biernacki, J.W. Bullard, S. Bishnoi, J.S. Dolado, G.W. Scherer, and A. Luttge. Modeling and simulation of cement hydration kinetics and microstructure development. *Cement and Concrete Research*, 41(12):1257–1278, 2011.

[17] M. Avrami. Kinetics of phase change. i general theory. *The Journal of Chemical Physics*, 7:1103, 1939.

[18] S. Garrault-Gauffinet and A. Nonat. Experimental investigation of calcium silicate hydrate (csh) nucleation. *Journal of crystal growth*, 200(3):565–574, 1999.

[19] J.J. Thomas. A new approach to modeling the nucleation and growth kinetics of tricalcium silicate hydration. *Journal of the American Ceramic Society*, 90(10):3282–3288, 2007.

[20] J.J. Thomas, H.M. Jennings, and J.J. Chen. Influence of nucleation seeding on the hydration mechanisms of tricalcium silicate and cement. *The Journal of Physical Chemistry C*, 113(11):4327–4334, 2009.

[21] IG Richardson. The nature of the hydration products in hardened cement pastes. *Cement and Concrete Composites*, 22(2):97–113, 2000.

[22] I. G. Richardson. Tobermorite/jennite- and tobermorite/calcium hydroxide-based models for the structure of c-s-h: Applicability to hardened pastes of tricalcium silicate, β-dicalcium silicate, portland cement, and blends of portland cement with blast-furnace slag, metakaolin, or silica fume. *Cement and Concrete Research*, 34(9):1733–1777, 2004.

[23] IG Richardson, AR Brough, GW Groves, and CM Dobson. The characterization of hardened alkali-activated blast-furnace slag pastes and the nature of the calcium silicate hydrate (CSH) phase. *Cement and concrete research*, 24(5):813–829, 1994.

[24] S.H. Kosmatka, W.C. Panarese, G.E. Allen, and S. Cumming. *Design and control of concrete mixtures*, volume 5420. Portland Cement Association Skokie, Ill., 2002.

[25] PJM Monteiro and PK Mehta. *Concrete-Microstructure, Properties and Materials.* New York: McGraw-Hill, 2006.

[26] G. Constantinides and F.J. Ulm. The effect of two types of csh on the elasticity of cement-based materials: Results from nanoindentation and micromechanical modeling. *Cement and Concrete Research*, 34(1):67–80, 2004.

[27] T.C. Powers and T.L. Brownyard. Studies of the physical properties of hardened portland cement paste. In *ACI Journal Proceedings*, volume 43. ACI, 1947.

[28] R.F. Feldman and P.J. Sereda. A model for hydrated portland cement paste as deduced from sorption-length change and mechanical properties. *Materials and structures*, 1(6):509–520, 1968.

[29] P.D. Tennis and H.M. Jennings. A model for two types of calcium silicate hydrate in the microstructure of portland cement pastes. *Cement and Concrete Research*, 30(6):855–863, 2000.

[30] H.M. Jennings. Refinements to colloid model of csh in cement: Cm-ii. *Cement and Concrete Research*, 38(3):275–289, 2008.

[31] R.J.M. Pellenq, A. Kushima, R. Shahsavari, K.J. Van Vliet, M.J. Buehler, S. Yip, and F.J. Ulm. A realistic molecular model of cement hydrates. *Proceedings of the National Academy of Sciences*, 106(38):16102–16107, 2009.

[32] IG Richardson and GW Groves. Microstructure and microanalysis of hardened ordinary portland cement pastes. *Journal of materials science*, 28(1):265–277, 1993.

[33] G. Constantinides, KS Ravi Chandran, F.J. Ulm, and KJ Van Vliet. Grid indentation analysis of composite microstructure and mechanics: Principles and validation. *Materials Science and Engineering: A*, 430(1):189–202, 2006.

[34] G. Constantinides and F.J. Ulm. The nanogranular nature of c–s–h. *Journal of the Mechanics and Physics of Solids*, 55(1):64–90, 2007.

[35] F.J. Ulm, M. Vandamme, C. Bobko, J. Alberto Ortega, K. Tai, and C. Ortiz. Statistical indentation techniques for hydrated nanocomposites: Concrete, bone, and shale. *Journal of the American Ceramic Society*, 90(9):2677–2692, 2007.

[36] A.J. Allen, J.J. Thomas, and H.M. Jennings. Composition and density of nanoscale calcium–silicate–hydrate in cement. *Nature materials*, 6(4):311–316, 2007.

[37] Y.I. Golovin. Nanoindentation and mechanical properties of solids in submicrovolumes, thin near-surface layers, and films: A review. *Physics of the solid State*, 50(12):2205–2236, 2008.

[38] W.C. Oliver and G.M. Pharr. Nanoindentation in materials research: Past, present, and future. *MRS bulletin*, 35(11):897–907, 2010.

[39] M. Miller, C. Bobko, M. Vandamme, and F.J. Ulm. Surface roughness criteria for cement paste nanoindentation. *Cement and Concrete Research*, 38(4):467–476, 2008.

[40] P. Lura, P. Trtik, and B. Münch. Validity of recent approaches for statistical nanoindentation of cement pastes. *Cement and Concrete Composites*, 33(4):457–465, 2011.

[41] P. Trtik, B. Münch, and P. Lura. A critical examination of statistical nanoindentation on model materials and hardened cement pastes based on virtual experiments. *Cement and Concrete Composites*, 31(10):705–714, 2009.

[42] C. Fraley and A.E. Raftery. Mclust: Software for model-based cluster analysis. *Journal of Classification*, 16(2):297–306, 1999.

[43] R.D.C. Team et al. R: A language and environment for statistical computing. *R Foundation Statistical Computing*, 2008.

[44] S. Cariou et al. *The effect of the packing density on the indentation hardness of cohesive-frictional porous materials.* PhD thesis, Massachusetts Institute of Technology, 2006.

[45] G. Constantinides and F.J. Ulm. The nanogranular nature of c-s-h. *Journal of the Mechanics and Physics of Solids*, 55(1):64–90, 2007.

[46] DL Rayment and AJ Majumdar. The composition of the CSH phases in portland cement pastes. *Cement and Concrete Research*, 12(6):753–764, 1982.

[47] J.J. Chen, L. Sorelli, M. Vandamme, F.J. Ulm, and G. Chanvillard. A Coupled Nanoindentation/SEM-EDS Study on Low Water/Cement Ratio Portland Cement Paste: Evidence for "C-S-H/$Ca(OH)_2$" Nanocomposites. *Journal of the American Ceramic Society*, 93(5):1484–1493, 2010.

[48] X. Pardal, I. Pochard, and A. Nonat. Experimental study of Si–Al substitution in calcium-silicate-hydrate (CSH) prepared under equilibrium conditions. *Cement and Concrete Research*, 39(8):637–643, 2009.

[49] Cement Sustainability Initiative. 2012 progress report. Technical report, World Business Council for Sustainable Development, 2012.

[50] Oom M. Terrien B. Zalewski J. Fraley, S. Design of experiments via taguchi methods: orthogonal arrays. In *Michigan chemical process dynamics and controls open textbook.* 2007.

[51] G. Taguchi, E.A. Elsayed, and T.C. Hsiang. *Quality engineering in production systems.* McGraw-Hill College, 1989.

[52] H.F.W. Taylor. Modification of the bogue calculation. *Advances in Cement Research*, 2(6):73–77, 1989.

[53] K. Riding, D.A. Silva, and K. Scrivener. Early age strength enhancement of blended cement systems by $CaCl_2$ and diethanol-isopropanolamine. *Cement and Concrete Research*, 40(6):935–946, 2010.

[54] W.C. Oliver and G.M. Pharr. Improved technique for determining hardness and elastic modulus using load and displacement sensing indentation experiments. *Journal of materials research*, 7(6):1564–1583, 1992.

[55] J. Hjorth, J. Skibsted, and H.J. Jakobsen. ^{29}si mas nmr studies of portland cement components and effects of microsilica on the hydration reaction. *Cement and Concrete Research*, 18(5):789 – 798, 1988.

[56] J. Keeler. *Understanding NMR spectroscopy*. Wiley, 2011.

[57] J. Chen. *The Nanostructure of Calcium Silicate Hydrate*. PhD thesis, Northwestern University, 2003.

[58] E. Sakai, S. Miyahara, S. Ohsawa, S.H. Lee, and M. Daimon. Hydration of fly ash cement. *Cement and Concrete Research*, 35(6):1135–1140, 2005.

[59] AV Girao, IG Richardson, R. Taylor, and RMD Brydson. Composition, morphology and nanostructure of C–S–H in 70% white Portland cement–30% fly ash blends hydrated at 55ř C. *Cement and Concrete Research*, 40(9):1350–1359, 2010.

[60] S. Hanehara, F. Tomosawa, M. Kobayakawa, and K.R. Hwang. Effects of water/powder ratio, mixing ratio of fly ash, and curing temperature on pozzolanic reaction of fly ash in cement paste. *Cement and Concrete Research*, 31(1):31–39, 2001.

[61] P. Wang and X. Liu. Effect of temperature on the hydration process and strength development in blends of portland cement and activated coal gangue or fly ash. *Journal of Zhejiang University-Science A*, 12(2):162–170, 2011.

[62] J.J. Beaudoin, RF Feldman, J. Baron, and M. Conjeaud. *Dependence of Degree of Silica Polymerization and Intrinsic Mechanical Properties of CSH-on C/S Ratio*. National Research Council Canada, Institute for Research in Construction, 1986.

[63] C. Plassard, E. Lesniewska, I. Pochard, and A. Nonat. Investigation of the surface structure and elastic properties of calcium silicate hydrates at the nanoscale. *Ultramicroscopy*, 100(3):331–338, 2004.

[64] P.K. Mehta and O.E. GjÃÿrv. Properties of portland cement concrete containing fly ash and condensed silica-fume. *Cement and Concrete Research*, 12(5):587 – 595, 1982.

[65] Vagelis G. Papadakis. Effect of fly ash on portland cement systems: Part i. low-calcium fly ash. *Cement and Concrete Research*, 29(11):1727 – 1736, 1999.

[66] C.P. Vernet. Ultra-durable concretes: Structure at the micro-and nanoscale. *MRS Bulletin*, 29(05):324–327, 2004.

[67] L. Sorelli, G. Constantinides, F.J. Ulm, and F. Toutlemonde. The nano-mechanical signature of ultra high performance concrete by statistical nanoindentation techniques. *Cement and Concrete Research*, 38(12):1447–1456, 2008.

[68] MM Reda, NG Shrive, and JE Gillott. Microstructural investigation of innovative uhpc. *Cement and Concrete Research*, 29(3):323–329, 1999.

[69] B. Cavill and M. Rebentrost. Ductal-a High-performance Material for Resistance to Blasts and Impacts. *Australian Journal of Structural Engineering*, 7(1):37, 2006.

[70] Js1100rs: Field-cast joint fill solutions for accelerated bridge construction. Technical report, Lafarge Canada, Inc.

[71] L. Gatty, S. Bonnamy, A. Feylessoufi, C. Clinard, P. Richard, and H. Van Damme. A transmission electron microscopy study of interfaces and matrix homogeneity in ultra-high-performance cement-based materials. *Journal of materials science*, 36(16):4013–4026, 2001.

[72] R. Shahsavari, M.J. Buehler, R.J.M. Pellenq, and F.J. Ulm. First-Principles Study of Elastic Constants and Interlayer Interactions of Complex Hydrated Oxides: Case Study of Tobermorite and Jennite. *Journal of the American Ceramic Society*, 92(10):2323–2330, 2009.

[73] P. Chindaprasirt, C. Jaturapitakkul, and T. Sinsiri. Effect of fly ash fineness on compressive strength and pore size of blended cement paste. *Cement and Concrete Composites*, 27(4):425–428, 2005.

[74] W.A. Deer and R.A. Howie. *An introduction to the rock-forming minerals.* Longman, 1966.

[75] B. Cavill and M. Rebentrost. Ductal-a High-performance Material for Resistance to Blasts and Impacts. *Australian Journal of Structural Engineering*, 7(1):37, 2006.

[76] EM Gartner, KE Kurtis, and PJM Monteiro. Proposed mechanism of csh growth tested by soft x-ray microscopy. *Cement and concrete research*, 30(5):817–822, 2000.

[77] MCG Juenger, PJM Monteiro, EM Gartner, and GP Denbeaux. A soft x-ray microscope investigation into the effects of calcium chloride on tricalcium silicate hydration. *Cement and concrete research*, 35(1):19–25, 2005.

[78] M.C.G. Juenger, P.J.M. Monteiro, and EM Gartner. In situ imaging of ground granulated blast furnace slag hydration. *Journal of materials science*, 41(21):7074–7081, 2006.

[79] R. Grossier, A. Magnaldo, and S. Veesler. Ultra-fast crystallization due to confinement. *Journal of Crystal Growth*, 312(4):487–489, 2010.

[80] R. Grossier, Z. Hammadi, R. Morin, and S. Veesler. Predictive nucleation of crystals in small volumes and its consequences. *Physical Review Letters*, 107(2):25504, 2011.

[81] R. Grossier and S. Veesler. Reaching one single and stable critical cluster through finite-sized systems. *Crystal Growth and Design*, 9(4):1917–1922, 2009.

[82] M.R. Lamprecht, D.M. Sabatini, A.E. Carpenter, et al. Cellprofiler: free, versatile software for automated biological image analysis. *Biotechniques*, 42(1):71, 2007.

[83] SS Potgieter-Vermaak, JH Potgieter, and R. Van Grieken. The application of raman spectrometry to investigate and characterize cement, part i: A review. *Cement and concrete research*, 36(4):656–662, 2006.

[84] S. Martínez Ramírez, L. Fernández Carrasco, et al. Raman spectroscopy: application to cementitious systems. 2011.

[85] J. Ibáñez, L. Artús, R. Cuscó, Á. López, E. Menéndez, and M.C. Andrade. Hydration and carbonation of monoclinic c2s and c3s studied by raman spectroscopy. *Journal of Raman Spectroscopy*, 38(1):61–67, 2007.

[86] ZV Padanyi. The Raman spectrum of $Ca(OH)_2$. *Solid State Communications*, 8(7):541–543, 1970.

[87] R.J. Kirkpatrick, JL Yarger, P.F. McMillan, Y. Ping, and X. Cong. Raman spectroscopy of CSH, tobermorite, and jennite. *Advanced Cement Based Materials*, 5(3):93–99, 1997.

[88] IG Richardson, J. Skibsted, L. Black, and R.J. Kirkpatrick. Characterisation of cement hydrate phases by tem, nmr and raman spectroscopy. *Advances in cement research*, 22(4):233–248, 2010.

[89] D. Damidot and A. Nonat. C_3S Hydration in diluted and stirred suspension: I. Evidence of two CSH precipitation steps'. *Adv. Cement Res*, 1994.

[90] E. Gallucci, P. Mathur, and K. Scrivener. Microstructural development of early age hydration shells around cement grains. *Cement and Concrete Research*, 40(1):4–13, 2010.

[91] MW Davidson and P. Dirac. Nikon MicroscopyU: Concepts and Formulas in Microscopy Resolution, 2007.

[92] R.J. Collins and S.K. Ciesielski. *Recycling and use of waste materials and by-products in highway construction.* Number 199. 1994.